Formation mechanism of spatial and temporal fractals in bipedal walking

Kota OKAMOTO

KYOTO UNIVERSITY

DOCTORAL THESIS

Formation mechanism of spatial and temporal fractals in bipedal walking

Author:
Kota OKAMOTO

Supervisor:
Prof. Kei SENDA

A thesis submitted in fulfillment of the requirements for the degree of Doctor of Philosophy

in the

Dynamics in Aeronautics and Astronautics
Department of Aeronautics and Astronautics, Graduate School of Engineering

Acknowledgements

First and foremost, I would like to express my sincere gratitude to Dr. Kei Senda, Professor of Department of Aeronautics and Astronautics, Graduate School of Engineering, Kyoto University, for his continuous guidance and support. Without his valuable advice and comments, this thesis would never be completed.

I would like to express appreciation to Dr. Kenji Fujimoto, Professor of Department of Aeronautics and Astronautics, Graduate School of Engineering, Kyoto University, Dr. Ichiro Maruta, Associate Professor of Department of Aeronautics and Astronautics, Graduate School of Engineering, Kyoto University, and Dr. Toshiyuki Ohtsuka, Professor of Department of Informatics, Graduate School of Informatics, Kyoto University, for their valuable comments and suggestions.

I would like to extend the deepest appreciation to Dr. Shinya Aoi, Professor of Department of Mechanical Science and Bioengineering, Graduate School of Engineering Science, Osaka University, for his continuous guidance and grateful support thorough out my research. He has tirelessly used exertion for teaching and supporting me. Without his valuable advice and support, this thesis would not have materialized.

I would like to express my cordial gratitude to Dr. Tsuchiya Kazuo, Professor of Department of Aeronautics and Astronautics, Graduate School of Engineering, Kyoto University, for his invaluable comments and suggestions. I was indeed stimulated by discussion with him and strongly influenced by his perspective to researches.

I would like to express appreciation to Dr. Hiroshi Kokubu, Professor of Department of Mathematics, Graduate School of Science, Kyoto University, and Dr. Ippei Obayashi, Professor of Cyber-Physical Engineering Information Research Core (Cypher), Okayama University, for the collaboration in experimental works and their useful comments and discussions.

I would like to express appreciation to Dr. Nozomi Akashi, Assistant Professor of Graduate School of Informatics, Kyoto University, for the collaboration in experimental work. I was taught a lot of things through the experiment with him.

I would like to express appreciation to Dr. Yuichi Ambe, Assistant Professor of Department of Mechanical Science and Bioengineering, Graduate School of Engineering Science, Osaka University, Dr. Nozomi Tomita, Researcher of Department of Mechanical Science and Bioengineering, Graduate School of Engineering Science, Osaka University, and Dr. Mau Adachi, Researcher of Department of Mechanical Science and Bioengineering, Graduate School of Engineering Science, Osaka University, for encouragement and advice. Taking a coffee break refreshed me and when I had minor technical problems, they helped me to solve them.

I would like to thank the members of the laboratory of Dynamics in Aeronautics and Astronautics and the laboratory of Systems and Control. Thanks to seminar, discussion, experiment, conversation, and activity with them, I have fully enjoyed my student life. Especially, I would like to express appreciation to Mr. Ryo Iba.

Lastly, I am deeply grateful to my parents, Takashi and Kumiko Okamoto, for their generous attitude, constant support, and warm encouragement during my student life.

Contents

Chapter 1

Introduction

1.1 Background

Fractal is a general term for complex spatial and temporal features that do not take simple shapes regardless of how much they are magnified. This fractal nature can be observed in various things in nature. Spatial fractality is observed in branching trees, complexly shaped coastlines, and anatomical structures such as dendritic structures in human arteries and veins. Temporal fractality is observed in signals emitted from living organisms, such as human heart rate. Both spatial and temporal fractals are observed during bipedal walking. Usually, studies have focused on stability, speed, and energy efficiency as the characteristics of walking, but fractality has not been sufficiently studied. However, fractality has been suggested to play an important role in the characterization of gait because it is related to gait stability and the degree of functional disability in human gait. In this study, we investigated the roles of body and neural control systems in the fractal nature of bipedal gait using a model.

1.2 Related works

1.2.1 Fractal

Spatial fractal

The term "fractal" was coined by B. Mandelbrot, a mathematician at IBM, in the 1960s. It is generally accepted that fractals exhibit the following three properties: complex structures at multiple length scales, repetition of structures at different length scales (self-similarity), and "fractal dimension" which is not an integer. To satisfy these requirements, a fractal object is composed of units, whose structure resembles that of an entire object, and subunits, whose structure resembles that of each unit.

We consider the Cantor set an example of a fractal geometric structure. The Cantor set is defined as follows. Starting from the closed interval $S_0 = [0, 1]$, the middle third is removed. The two resulting intervals are $S_1 = [0, 1/3] \cup [2/3, 1]$, and the central third of each interval is removed to obtain S_2, which consists of four intervals. This is repeated and S_∞ is obtained as the limit is the Cantor set. This Cantor

set is fractal because of its complexity over a wide range of spatial scales and self-similarity, as described above.

When an object has a fractal structure, its dimension (fractal dimension) is not integer. Generally, dimension is the minimum number of coordinates required to specify a point in the object. For example, a smooth curve has one dimension, and a smooth surface has two dimensions. However, the Cantor set is not one-dimensional because its entire length is $\lim_{n\to\infty}(\frac{2}{3})^n = 0$. The Cantor set is also not zero-dimensional, because it is a set of countless points. Therefore, the dimensions of the Cantor set are less than 1 and larger than 0. The non-integer dimension representing a fractal object obtained from this concept is called the fractal dimension.

There are several ways to obtain fractal dimensions. For example, one definition of a fractal is that it has complex structures at multiple length scales. Based on this property, the number of boxes required to cover a fractal figure with equally spaced boxes is investigated. A fractal dimension is quantified by examining how the number of boxes to cover changed as the size of the box decreased. Any two-dimensional rectangle in $\mathbb{R}^2$ can be covered by $C(1/\epsilon)^2$ squares of side ϵ, where C is a constant that depends on object size. Similarly, a d-dimensional (d is an integer) region requires $C(1/\epsilon)^d$ boxes with size ϵ. That is, the number of boxes of size ϵ is scaled by $(1/\epsilon)^d$. Extending this idea to more complex objects such as fractals, we consider using this "scaling rule" to define the dimension d (d may not be an integer) of an object whose dimension is not known in advance. What is defined by this idea is called the box-counting dimension, which is one of the several definitions of the fractal dimension. In the case of the Cantor set described above, $d = \log 2/\log 3$ because the number of necessary boxes doubles every time ϵ is multiplied by $1/3$.

Other definitions of the fractal dimension include the similarity dimension based on the self-similarity of fractals, the correlation dimension, which is obtained from the density of points on a chaotic attractor, and the Hausdorff dimension, which measures the number of elements using a box of variable sizes instead of constant sizes [28]. All seek a dimension that is "the smallest element necessary to define the object," but it is difficult to characterize whatever fractal dimension means by a single dimension.

Temporal fractal

The concept of a fractal can be applied not only to geometric forms with complex shapes over a wide range of scales, where repeated structures appear at different spatial scales, but also to complex time series processes over a wide range of scales, where repeated structures appear at different time scales [79, 101, 104, 132]. Fractal time series processes generate irregular fluctuations across multiple timescales. This is analogous to a spatial feature that is composed of units that resemble the structure of an entire object. We focus on fluctuations at different temporal resolution scales to

understand the self-similarity of time series processes with fractality. When examining fractal time series at different temporal resolutions, the irregularities at different scales are indistinguishable and have statistical self-similarity [78, 123].

As with the fractal dimension in geometry, there are several ways to quantify the fractal time series. For example, if a time series Y is fractal, a small window of the time series has the same standard deviation as a larger window because they are statistically self-similar. In this case, $Y(Lt) \equiv L^H Y(t)$, where H is the Hurst exponent (L refers to the ratio of window sizes of the time series of interest, and $Y(t)$ is the standard deviation in that window). The Hurst exponent is a measure of the self-similarity of a time series.

Other methods include power spectrum analysis, which determines self-similarity based on the relationship between amplitude and frequency [29]. In particular, when considering the fractal nature of biological signals, because both stationary and non-stationary time series exist, Detrended Fluctuation Analysis (DFA), which does not assume stationarity, and the scaling index α obtained from DFA are often used to quantify self-similarity [39]. In this case, when $\alpha = 0.5$, the time series is white noise, whereas it is statistically persistent when $0.5 < \alpha < 1$ and statistically anti-pertinent when $0 < \alpha < 0.5$. Statistical pertinence is present when the fluctuations of the time series are statistically more likely to fluctuate in the same direction, whereas statistical anti-pertinence is present when the fluctuations are more likely to fluctuate in the opposite direction.

1.2.2 Spatial fractal in passive dynamic walking

Passive dynamic walking

Passive dynamic walking is a robot or a model that walks down a shallow slope without any actuators, sensors, or controls but only through the interaction between the walking machine and the environment. Because passive dynamic walking does not consume energy, controllers designed based on passive dynamic walking would be energy efficient and the dynamics is similar to that of human walking [85]. It is widely used to explore the mechanical principles of gait (gait dynamics) [9, 12, 15, 17, 18, 23, 58, 60, 70–73, 130, 131].

In an experiment on a real machine, McGeer realized a passive walker with knees [86, 87]. McGeer's passive dynamic walker has four identical legs, with two pairs of inner and outer legs that move synchronously. This condition constrains the walking motion in a two-dimensional sagittal plane. This walker also has knee stoppers that prevent the knees from bending backward and circular feet.

Limit cycle

McGeer [85–87] showed from numerical simulations that passive walking has two limit cycles: one stable and the other unstable. Walking continues for as long as the

state is in the limit cycle. Furthermore, when the limit cycle is stable, the state is pulled back into the limit cycle even if it leaves the limit cycle. When the trajectory is on a limit cycle, the periodic gait can be regarded as an equilibrium point in the Poincaré section. From this equilibrium point, the generation of the limit cycle and its stability can be analyzed.

McGeer analyzed not only a passive walker with knees but also rimless wheel locomotion, a compass-type model, and a model with an upper body. The basic framework for the analysis of passive dynamic walking was largely developed by McGeer in the early 1990s.

Bifurcation

After McGeer's studies, Goswami et al. [40] performed a detailed numerical simulation analysis of passive dynamic walking using a compass-type model. They found that the period-doubling bifurcation repeats as the slope angle increases. Specifically, as the slope angle increases, the period of the walking cycle changes from period-1 to period-2, from period-2 to period-4, and so on. The new gait doubled the period and eventually led to chaos. This period-doubling bifurcation occurs when the limit cycle changes from stable to unstable and the state transitions to another limit cycle.

At about the same time as Goswami et al., Garcia et al. [36] proposed the simplest walking model, which simplifies the compass-type model. They numerically confirmed that this model also exhibits the stable limit cycle and period-doubling bifurcation. They also showed the existence of multiple limit cycles and their stability by the perturbation method. The simplest walking model is used in various studies because it is useful for understanding the essence of the phenomenon [6,72,112,131].

Spatial fractal in basin of attraction

Schwab & Wisse [112] computed the basin of attraction using the simplest walking model and demonstrated that it exhibits a small and thin shape with fractal characteristics. Akashi et al. [2] numerically showed that the basin of attraction has fractality in a more general passive dynamic walking model. They also suggested that this fractality emerges at a different slope angle from the slope angle associated with chaotic attractors resulting from period-doubling bifurcations.

Because it is difficult to identify the basin of attraction in complex models and robotic systems, previous research has predominantly focused on simple models for researching the basin of attraction. However, it has been suggested that this fractality is generated by the saddle characteristics inherent in the inverted pendulum, which are common characteristics in bipedal walking [94]. Therefore, it would be a universal characteristic of bipedal locomotion. Because the fractality of the basin of

attraction directly influences a key measure of robustness known as final-state sensitivity [41], understanding the spatial fractality of the basin of attraction is important in elucidating the fundamental principles governing stable bipedal walking.

1.2.3 Central pattern generators

A neural circuit in the mammalian spinal cord generates a basic motor rhythm and produces alternating flexor and extensor motoneuron activities, which are the basis of locomotion. This circuit is called the central pattern generator (CPG), which can operate without sensory feedback [44, 98, 106, 107]. The role of afferent feedback in adjusting motor patterns to the motor task, environment, and biomechanical characteristics of limbs and body is crucial [100, 107]. For example, continuous electrical stimulation of the midbrain locomotor region of a fixed decerebrate cat produces "fictive locomotion," in which the flexor and extensor motoneurons are rhythmically alternately activated, similar to what occurs during normal movement in intact animals [106]. To investigate the effects of afferent inputs on the movement patterns generated by CPGs, experiments were conducted to reproduce fictive locomotion by stimulating sensory afferents in the flexor and extensor [50, 82, 105, 116]. These studies have revealed that, in many cases, afferent stimulation accelerates or delays the phase transition in an ongoing step cycle [83, 109]. Although these findings are based on animal studies, it has been suggested that CPGs are present in the human spinal cord [61, 88].

Although the anatomical structure of CPG circuits remains unclear, mathematical models have been used to study the general effects of afferent stimulation on CPG behavior. Recent neurophysiological findings suggest that CPGs are composed of a hierarchical network, including rhythm generator (RG) and pattern formation (PF) networks, and mathematical models have been devised based on this idea [13, 75, 108, 109]. In the RG, rhythm generation was simply modeled by a van der Pol oscillator [24, 127], Matsuoka oscillator [52, 69, 81, 95, 120, 121], or a phase oscillator [3–5, 26, 31, 99, 122, 133]. In PF, the generation of electromyography in each muscle was modeled [3, 4] from the basic patterns [65, 66] via α-motoneurons based on the muscle synergy hypothesis proposed by Ivanenko et al. [63, 64].

1.2.4 Temporal fractal in human gait

In human gait, fluctuations in the gait cycle exhibit temporal fractality [54]. Although the fluctuations in gait appeared to be random, the analysis using the DFA described above confirmed that the fluctuations in gait were statistically persistent. This statistical persistence indicates that fluctuations in gait are statistically more likely to be in the same direction, which is also called $1/f$ fluctuation. It has been shown that the persistence changes to uncorrelated by age and neural disease [39]. Because the fluctuation characteristics change with neural disease, it is believed that

the fluctuation characteristics of gait are derived from CPGs, and various CPG models have been proposed to reproduce this phenomenon [10, 54, 127]. However, even in simulations using bipedal models without CPGs, it has been confirmed that fluctuations in gait rhythm can have fractal characteristics [1, 38], and the mechanism of generation and change in the fractality of bipedal walking has not yet been clarified. It is known that not only aging and diseases but also external factors such as external input by a metronome and changes in walking speed using a treadmill can change fractality [55]. Therefore, sensory feedback may influence fractality.

1.3 Purpose of this thesis

Based on the above discussion, this study focuses on the importance of the generation and change of spatial and temporal fractality produced by bipedal walking, and aims to reproduce these fractalities with simple models to elucidate their mechanisms.

Regarding spatial fractality, because passive dynamic walking has already been shown to generate fractality in the basin of attraction, we confirmed the fractality using the simplest walking model [36] and clarified its generation mechanism based on the dynamical systems theory. Next, to quantitatively evaluate the fractality of passive dynamic walking, we investigated fractal dimension. The mechanism how the fractal dimension changes was also clarified based on dynamical systems theory.

Regarding temporal fractality, we propose a model that combines a simple CPG model with a simple biomechanical model to confirm the fractality. In particular, we conducted simulations assuming that the sensory feedback of the CPG changes fractality, confirmed that fractality changes depending on the presence or absence of feedback, and discussed the mechanism based on phase response characteristics [34, 122].

1.4 Outline of this thesis

Chapter 1 described the background and purpose of this study based on previous studies.

In Chapter 2, we analyze the spatial fractality of the basin of attraction in passive dynamic walking based on the dynamical systems theory. In this chapter, we use the simplest walking model [36] to analyze the characteristics of the basin of attraction depending on the slope angle. As a result, it is shown that the basin boundary is fractal at a certain slope angle. The fractal generation mechanism is elucidated by focusing on the basin formation process.

In Chapter 3, we investigate the change of fractal characteristics of basin of attraction of passive dynamic walking by slope angle. In this chapter, the fractal dimension and size of the basin of attraction are quantitatively evaluated using the

simplest walking model, as used in Chapter 2. Consequently, we confirmed that both the fractal dimension and size of the basin changed sharply at several slope angles. This sharp change in the basin was elucidated by improving the analytical method that focuses on the formation process in Chapter 2.

In Chapter 4, we propose a model that combines a simple CPG model and a simple biomechanical model based on the assumption that temporal fractality appears because of the interaction between the neural control system and the body dynamical system. In particular, we confirmed that fractality changes depending on the presence or absence of sensory feedback, and showed that the changes correspond to those in the gait of healthy subjects and those of aging or diseased patients. Furthermore, we showed that the fractality change was caused by phase response characteristics.

In Chapter 5, we conclude this thesis and present our future work.

Chapter 2

Mechanism of generation of spatial fractal in basin of attraction in passive dynamic walking

2.1 Introduction

Passive dynamic walking is a model that walks down a shallow slope without any control or input [85], which is useful for investigating the mechanism of generating stable walking from a dynamic viewpoint. This has been widely used to examine how humans walk with low energy consumption [12, 15, 23, 71–73] and to provide design principles for energy-efficient biped robots [9, 17, 18, 58, 60, 70, 130, 131]. However, the basin of attraction is very small and thin and has a fractal-like complicated shape [2, 93, 112], which makes it difficult to produce stable walking. Furthermore, chaos appears in the walking behavior through a period-doubling cascade by increasing the slope angle [40], which makes producing stable walking even more difficult. Meanwhile, the basin of attraction shows a fractal-like shape, even without period doubling. In other words, the fractal-like basin of attraction appears even for a single attractor. Although this indicates that a different mechanism from the period doubling of the attractor induces a fractal-like basin of attraction, the mechanism is unclear.

In our previous study [94], we used the simplest walking model [36] for the analysis of passive dynamic walking and clarified the formation mechanism for the basin of attraction based on dynamical systems theory by focusing on the hybrid dynamics of the model composed of the continuous dynamics generated by the equations of motion during the swing phase with saddle hyperbolicity and the discontinuous dynamics generated by the impact upon foot contact. Specifically, we found that the fractal-like basin of attraction is generated through iterative stretching and bending deformations by sequential inverse images of the Poincaré map for the collection of initial conditions from which the model can walk at least one step, which corresponds to the domain of the Poincaré map. However, whether the fractal-like basin of attraction is actually fractal, i.e., whether infinitely many self-similar patterns are embedded in the basin of attraction, is dependent on the model parameters, such

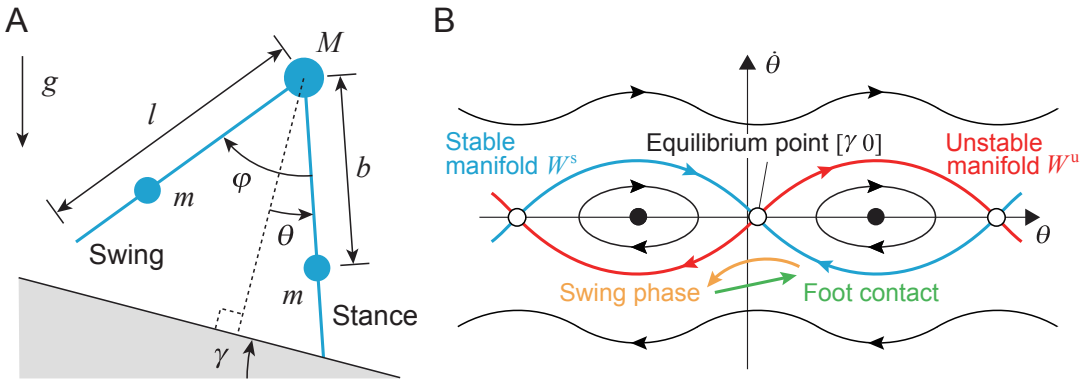

FIGURE 2.1: Passive dynamic walking. A. Compass-type model. B. Phase diagram $[\theta\,\dot{\theta}]$. Equilibrium point $[\theta\,\dot{\theta}] = [\gamma\,0]$ is a saddle point. Stable walking (indicated by the two arrows below the equilibrium point) is obtained by the continuous dynamics during the swing phase and the discontinuous dynamics upon foot contact.

as the slope angle [2, 112]. The mechanism that determines whether the basin of attraction is fractal remains unclear.

In the present study, we improved our previous analysis in order to clarify the mechanism. In particular, we newly focused on the range of the Poincaré map, which corresponds to the collection of states after the model walked one step starting from the domain, and specified the regions that are stretched and bent by the sequential inverse image of the Poincaré map. Through analysis of the specified regions, we clarified the condition and mechanism required for the basin of attraction to be fractal.

2.2 Method

2.2.1 Model

In the present study, we used a compass-type model (Fig. 2.1A) for the analysis of passive dynamic walking. This model has two legs (rigid links), the lengths of which are both l, connected by a frictionless hip joint. Here, θ is the angle of the stance leg with respect to the slope normal, and φ is the relative angle between the stance and swing legs. The mass is located only at the hip and the leg. The hip mass is M, and the leg mass is m. The leg mass is located at a distance b from the hip joint. In addition, g is the acceleration due to gravity. This model walks on a slope of angle γ without any control or input.

2.2.2 Structure of phase space by hybrid dynamics

In the present study, we focused on the simplest walking model, where $m/M \to 0$ and $b/l \to 1$ [36], because the dynamical characteristics remain almost unchanged [94]. This model is governed by hybrid dynamics composed of the continuous dynamics generated by the equations of motion during the swing phase

and the discontinuous dynamics generated by the impact upon foot contact.

The equations of motion are given by

$$\ddot{\theta} - \sin(\theta - \gamma) = 0 \tag{2.1}$$

$$(\cos\varphi - 1)\ddot{\theta} + \ddot{\varphi} - \dot{\theta}^2 \sin\varphi + \sin(\varphi - \theta + \gamma) = 0 \tag{2.2}$$

These equations are nondimensionalized by the time scale $\sqrt{l/g}$ and have an equilibrium point $[\theta\,\dot{\theta}\,\varphi\,\dot{\varphi}] = [\gamma\,0\,0\,0]$, which describes the situation where both legs are upright. The eigenvalues of the linearized equations of motion at the equilibrium point are ± 1 and $\pm i$, and the equilibrium point is a saddle center with one stable direction, one unstable direction, and two neutral directions. Specifically, θ is determined only by (2.1) and is not affected by φ. This equation for θ has a saddle equilibrium point at $[\theta\,\dot{\theta}] = [\gamma\,0]$, as shown in Fig. 2.1B. In the phase diagram of $[\theta\,\dot{\theta}]$ the trajectories going into and out of the equilibrium point are the stable manifold W^{s} and the unstable manifold W^{u}, respectively. In the phase space of four variables $[\theta\,\dot{\theta}\,\varphi\,\dot{\varphi}]$, $W^{\mathrm{s}} \times \mathbb{R}^2$ and $W^{\mathrm{u}} \times \mathbb{R}^2$ are the center-stable manifold and the center-unstable manifold, respectively, and we denote them by W^{cs} and W^{cu}.

Foot contact occurs when the following conditions are satisfied:

$$2\theta - \varphi = 0 \tag{2.3}$$

$$-\pi/2 < \theta < 0 \tag{2.4}$$

$$2\dot{\theta} - \dot{\varphi} < 0 \tag{2.5}$$

The impact upon foot contact yields the following relationship:

$$\begin{bmatrix} \theta^+ \\ \dot{\theta}^+ \\ \varphi^+ \\ \dot{\varphi}^+ \end{bmatrix} = \begin{bmatrix} -\theta^- \\ \dot{\theta}^- \cos 2\theta^- \\ -2\theta^- \\ \cos 2\theta^- (1 - \cos 2\theta^-)\dot{\theta}^- \end{bmatrix} \tag{2.6}$$

where $*^-$ and $*^+$ are the state $*$ just before and after the foot contact, respectively. The important property of this relationship is that the state just after foot contact $[\theta^+\,\dot{\theta}^+\,\varphi^+\,\dot{\varphi}^+]$ depends only on $[\theta^-\,\dot{\theta}^-]$ and is independent of $[\varphi^-\,\dot{\varphi}^-]$. This means that the state just after foot contact forms a two-dimensional surface in the four-dimensional phase space $[\theta^-\,\dot{\theta}^-\,\varphi^-\,\dot{\varphi}^-]$ and satisfies the following two conditions:

$$2\theta^+ = \varphi^+ \tag{2.7}$$

$$\dot{\varphi}^+ = \dot{\theta}^+(1 - \cos 2\theta^+) \tag{2.8}$$

In addition, from (2.4), the state just after foot contact also satisfies

$$0 < \theta^+ < \pi/2 \tag{2.9}$$

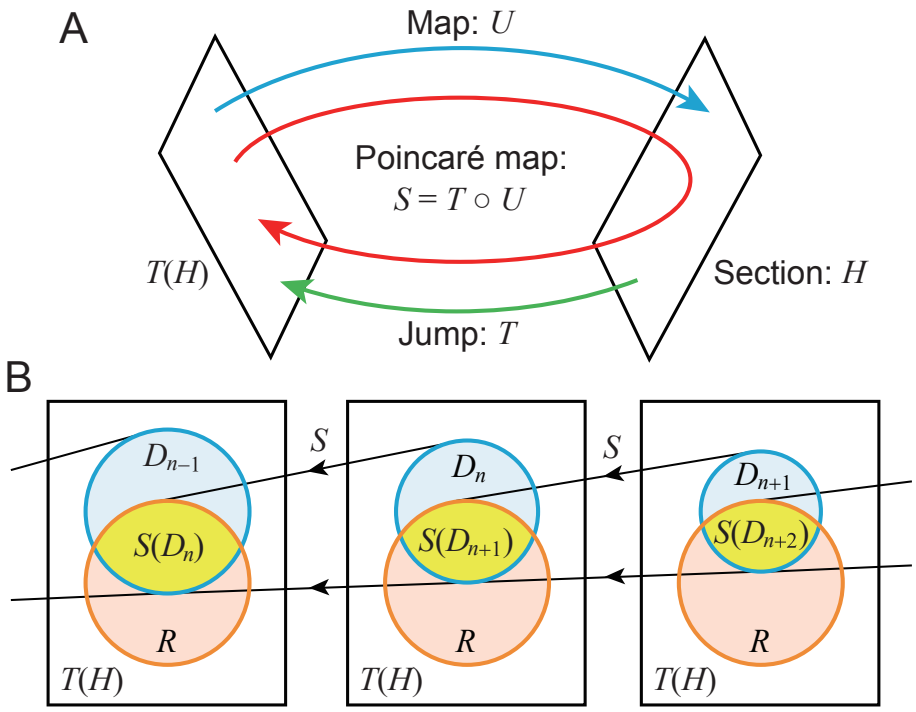

FIGURE 2.2: Schematic diagram of the structure of the phase space. A. Hybrid dynamics composed of the section H, jump T, and map U. B. Relationship among D_n, $S(D_n)$, and R on $T(H)$.

However, note that since the state just after foot contact is independent of $\dot{\varphi}^-$, (2.5) generates no condition.

This hybrid dynamic system determines the structure of the phase space, as shown in Fig. 2.2A. Here, H is the section defined by the foot contact conditions (2.3)–(2.5) and forms a three-dimensional space in the four-dimensional phase space, and T is the jump in the phase space from the state just before foot contact to the state just after foot contact, as defined by (2.6). Therefore, the image of T, $T(H)$, is the region representing all states just after foot contact, and a new step starts from $T(H)$. Moreover, U is the map from the start of a step to the next instance of foot contact. In other words, U is the map from $T(H)$ to H, as defined by the equations of motion (2.1) and (2.2). The Poincaré map S is defined on the Poincaré section $T(H)$ by

$$S = T \circ U : T(H) \to T(H) \tag{2.10}$$

This Poincaré map S represents one step, and an attractor of S represents stable walking. The basin of attraction of S is the main topic of the present paper. Here, S is parameterized by one parameter γ. In particular, S has an attracting fixed point at $0 < \gamma < 0.015$, and there is a period-doubling cascade to chaos for $0.015 < \gamma < 0.019$ [36].

2.2.3 Domain of Poincaré map and basin of attraction

We define D_n $(n = 1, 2, ...)$ as the collection of initial conditions on $T(H)$ from which the model walks at least n steps. This satisfies $D_{n+1} \subseteq D_n$ (Fig. 2.2B), which means that when the initial condition is in D_n but out of D_{n+1}, the model will fall down at the $n+1$-th step. Since the Poincaré map S represents walking one step, $S(D_n)$ indicates the state on $T(H)$ after the model walked one step starting from D_n. Since the model can walk at least $n-1$ steps from $S(D_n)$, the following condition is satisfied:

$$S(D_n) \subseteq D_{n-1} \tag{2.11}$$

Since the domain D of S on $T(H)$ represents the collection of initial conditions on $T(H)$ from which the model walks at least one step, D is identical to D_1.

Using the inverse image of S, we can write $D_n = S^{-1}(D_{n-1})$. However, S^{-1} acts only on a part of D_{n-1}, as shown in Fig. 2.2B, as clarified in the following section. First, the range R of S on $T(H)$ is given by $R = S(D_1)$ because D_1 is the domain of S, which corresponds to the collection of states after the model successfully walked one step starting from all states on $T(H)$. This means that the state after each step must be in R unless the model falls down. The following equation is satisfied:

$$S(D_n) = D_{n-1} \cap R \tag{2.12}$$

We prove this below. First, since $D_n \subseteq D_1$, $S(D_n) \subseteq R$. Based on this consideration and (2.11), $S(D_n) \subseteq D_{n-1} \cap R$. Second, we assume that $d \notin S(D_n)$ for $\exists d \subseteq D_{n-1} \cap R$. Since d is in R, S^{-1} is applicable to d, and, since d is in D_{n-1}, $S^{-1}(d) \subseteq D_n$. This contradicts $d \notin S(D_n)$. Therefore, this assumption is not satisfied. Since any state in $D_{n-1} \cap R$ is in $S(D_n)$, we obtain (2.12). Therefore, instead of $D_n = S^{-1}(D_{n-1})$, we use

$$D_n = S^{-1}(D_{n-1} \cap R) \tag{2.13}$$

In the same manner, instead of $D_n = S^{-n+1}(D_1)$, we use

$$D_n = S^{-1}(S^{-1}(\cdots(S^{-1}(D_1 \cap R) \cap R)\cdots \cap R) \cap R) \tag{2.14}$$

Since the model walks at least n steps from D_n, D_n approximates the basin of attraction as n increases. We confirmed the convergence by comparing D_{100} and D_{200} using $10^4 \times 10^4$ initial states.

2.3 Results

2.3.1 D_n and basin of attraction

Figs. 2.3A and 2.3C show D_1, D_2, D_3, and the basin of attraction for $\gamma = 0.001$ and 0.013, respectively. In order to clarify these geometric characteristics, we used $\theta + \dot{\theta}$

and $\theta - \dot{\theta}$ for the axes for $\gamma = 0.001$ and 0.013 in Figs. 2.3B and 2.3D, respectively, as in our previous study [94]. Here, D_2 and D_3 are V-shaped, and D_3 has a thin slit (note that a V-shaped region indicates that the basin has one large slit). The basins of attraction have multiple slits and are complicated. In particular, while the basin of attraction has only a few slits for $\gamma = 0.001$, the basin has a number of slits, and self-similar patterns are embedded for $\gamma = 0.013$. In order to quantitatively clarify these properties, we examined how many gaps D_1, D_2, D_3, and the basin of attraction have on the line $\theta - \dot{\theta} = 0.5$. As a result, there are zero, one, two, and four gaps in D_1, D_2, D_3, and the basin of attraction, respectively, for $\gamma = 0.001$. In contrast, there are zero, one, two, and infinitely many gaps in D_1, D_2, D_3, and the basin of attraction, respectively, for $\gamma = 0.013$. We further investigated the number of slits in D_1, D_2, D_3, and the basin of attraction for γ based on the gaps on $\theta - \dot{\theta} = 0.5$ in Fig. 2.3E. The number of slits in D_n increases as n increases, and that in the basin of attraction increases exponentially as γ increases. Fractal structures appear in the basin of attraction over $\gamma \approx 0.0075$.

2.3.2 $D_1 \cap R$

Since $D_n = S^{-1}(S^{-1}(\cdots(S^{-1}(D_1 \cap R) \cap R) \cdots \cap R) \cap R)$ approximates the basin of attraction as $n \to \infty$, we begin with $D_1 \cap R$ to investigate the formation mechanism of the basin of attraction. As shown in Fig. 2.3E, the numbers of slits in D_1, D_2, and D_3 remain unchanged for γ. Therefore, we assume that the mechanism is common for γ when n is small. We used $\gamma = 0.013$ to show the results below.

Since $R = S(D_1) = T(U(D_1))$, we first examine $U(D_1)$. In particular, the boundaries of $U(D_1)$ are $\theta = 0, \theta = -\pi/2$, and $2\dot{\theta} = \dot{\varphi}$ from the foot contact conditions (2.4) and (2.5), as shown in Fig. 2.4A. In addition, since D_1 does not intersect with W^{cu}, D_1 and $U(D_1)$ are on the same side with respect to W^{cu}, and $U(D_1)$ also has a boundary near W^{cu} (strictly speaking, D_1 intersects with W^{cu} in a small range of $0 < \theta < \gamma$, but has no influence in the formation of $D_1 \cap R$ and so is ignored). Fig. 2.4B shows the result for $U(D_1)$ projected onto the θ-$\dot{\theta}$ plane (Fig. 2.4C uses $\theta + \dot{\theta}$ and $\theta - \dot{\theta}$ for the axes in order to clarify the geometric characteristics).

Since T is a one-to-one mapping for $[\theta\, \dot{\theta}]$, the boundaries of $U(D_1)$ on the θ-$\dot{\theta}$ plane become the boundaries of R by T, as shown in Fig. 2.4A. Fig. 2.4D shows the result of R obtained from (2.6) (Fig. 2.4E uses $\theta + \dot{\theta}$ and $\theta - \dot{\theta}$ for the axes to clarify the geometric characteristics). The boundaries $\mathrm{a_1b_1}$ and $\mathrm{c_1d_1}$ of $D_1 \cap R$ are obtained by applying T to the boundaries near W^{cu} and $2\dot{\theta} = \dot{\varphi}$, respectively, of $U(D_1)$.

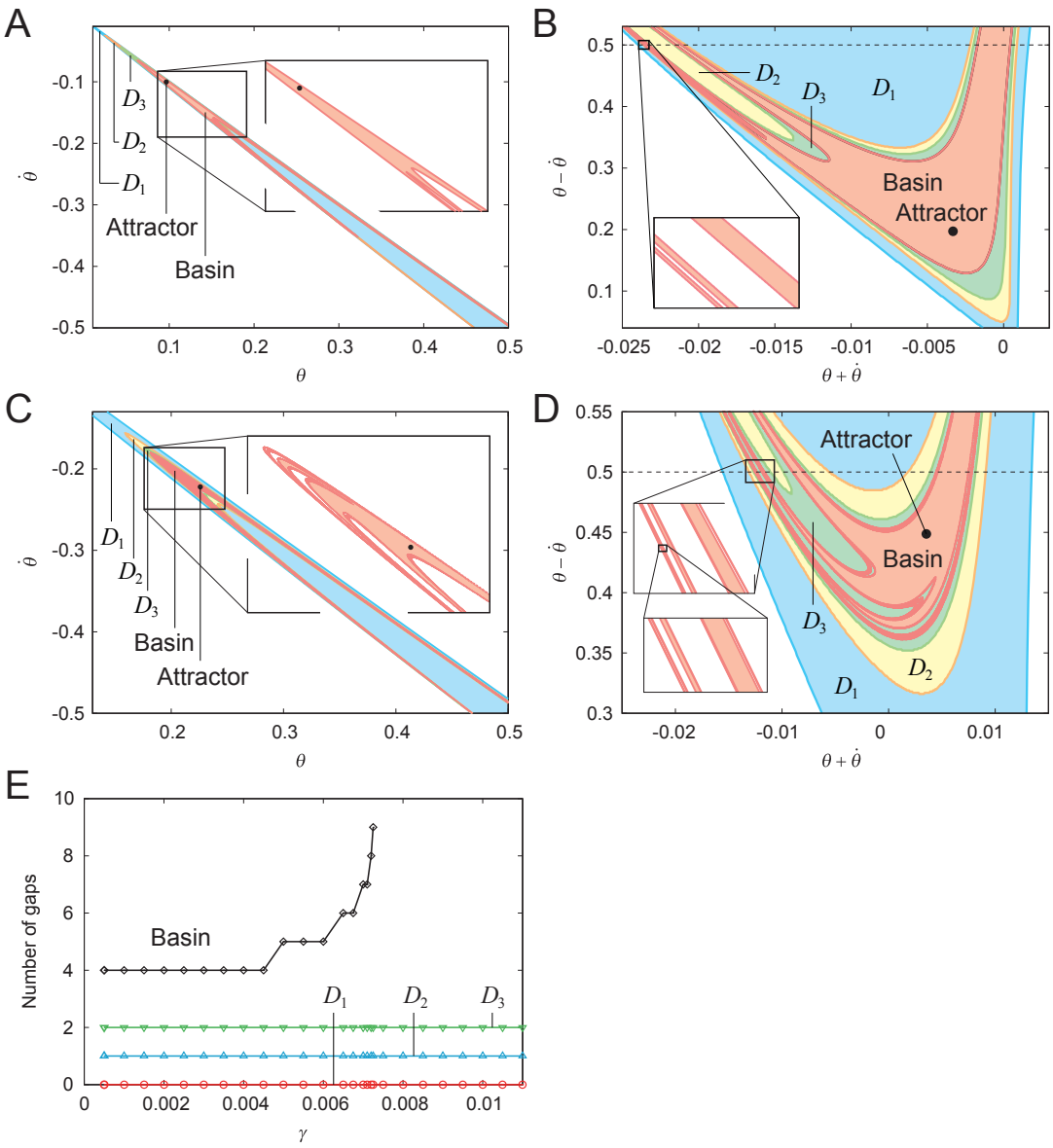

FIGURE 2.3: Evolution of the basin of attraction through D_1, D_2, and D_3. A-D. D_1, D_2, D_3, and the basin of attraction for $\gamma = 0.001$ (A and B) and 0.013 (C and D) in the θ-$\dot{\theta}$ plane and $(\theta+\dot{\theta})$-$(\theta-\dot{\theta})$ plane, respectively. Parts of the basin of attraction are enlarged. E. The number of gaps on $\theta - \dot{\theta} = 0.5$ depending on γ.

2.3.3 Characteristics of S^{-1}

Next, we investigate $D_2 = S^{-1}(D_1 \cap R)$. Since $S^{-1}(D_1 \cap R) = U^{-1}(T^{-1}(D_1 \cap R))$, we first examine $T^{-1}(D_1 \cap R)$. From (2.6), $T^{-1}(D_1 \cap R)$ is described by

$$\left\{ [-\theta^+ \; -2\theta^+ \; \dot{\theta}^+ \sec 2\theta^+ \; \dot{\varphi}^-] \;\middle|\; [\theta^+ \; \varphi^+ \; \dot{\theta}^+ \; \dot{\varphi}^+] \in D_1 \cap R, \; \dot{\varphi}^- \in \mathbb{R} \right\} \tag{2.15}$$

$[\theta \; \varphi \; \dot{\theta}]$ in $T^{-1}(D_1 \cap R)$ is uniquely determined using $D_1 \cap R$ in Fig. 2.4D. Fig. 2.5A shows the result of $T^{-1}(D_1 \cap R)$ in the θ-$\dot{\theta}$ plane. (Fig. 2.5B uses $\theta+\dot{\theta}$ and $\theta-\dot{\theta}$ for the axes to clarify the geometric characteristics.) The boundary $\hat{a}_1\hat{b}_1\hat{c}_1\hat{d}_1$ of $T^{-1}(D_1 \cap R)$ is obtained by applying T^{-1} to the boundary $a_1b_1c_1d_1$ of $D_1 \cap R$ in Fig. 2.4D. Note

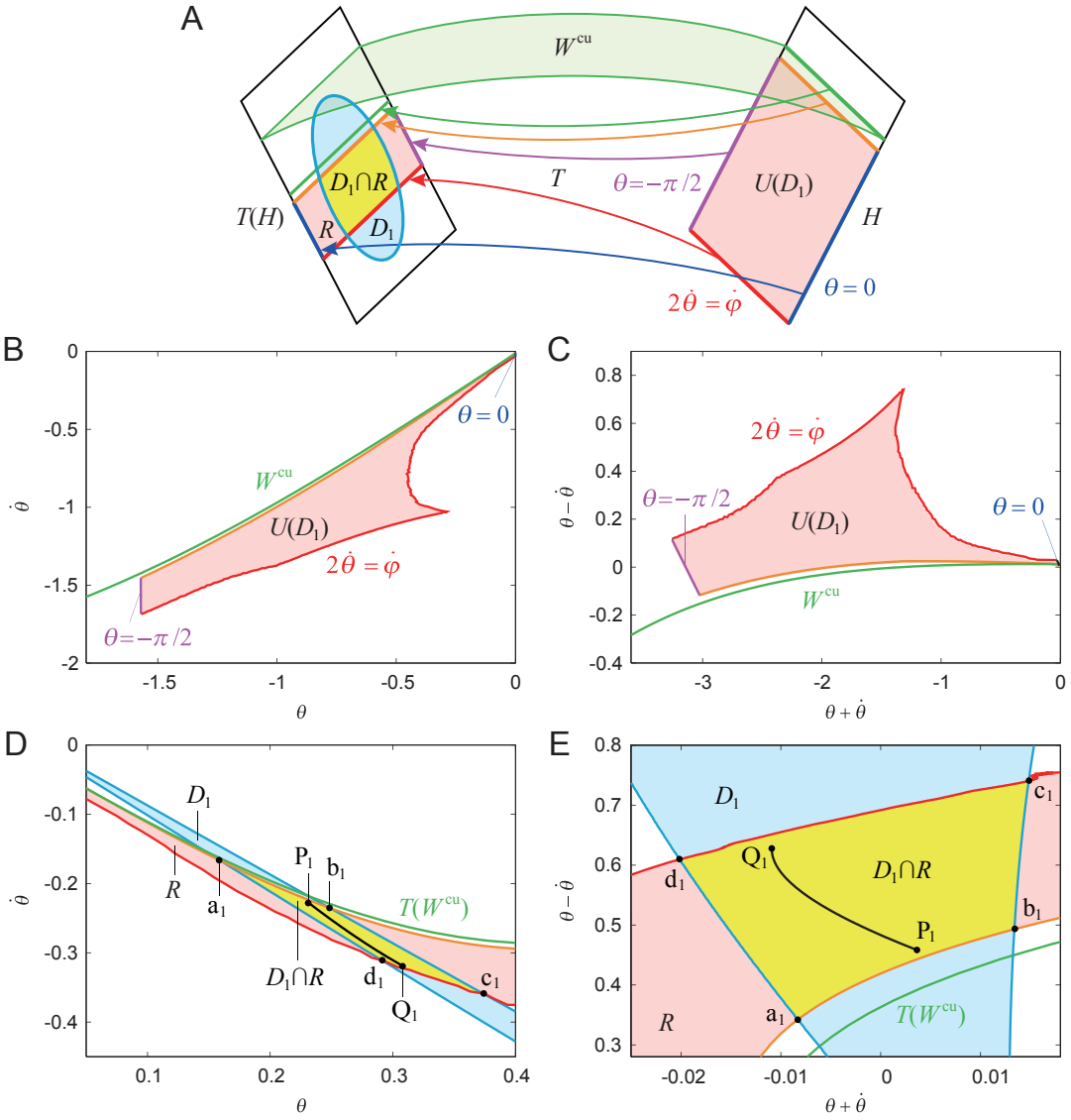

FIGURE 2.4: Relationship among D_1, $U(D_1)$, and R. A. Schematic diagram in phase space. B and C. $U(D_1)$ in the θ-$\dot{\theta}$ plane and $(\theta+\dot{\theta})$-$(\theta-\dot{\theta})$ plane, respectively. D and E. $D_1 \cap R$ in the θ-$\dot{\theta}$ plane and the $(\theta+\dot{\theta})$-$(\theta-\dot{\theta})$ plane, respectively.

that $*_1$ and $\hat{*}_1$ (except for D_1), such as a_1 and $\hat{a}_1$, are used for $D_1 \cap R$ and $T^{-1}(D_1 \cap R)$, respectively. Since $T^{-1}(D_1 \cap R)$ is thin, as shown in Fig. 2.5A, we extract a line segment $\hat{P}_1\hat{Q}_1$ from $T^{-1}(D_1 \cap R)$. However, since $\dot{\varphi}$ in $T^{-1}(D_1 \cap R)$ is not uniquely determined, we consider $T^{-1}(D_1 \cap R)$ as a quadrangular prism, the height of which is in the $\dot{\varphi}$ direction, as shown in Fig. 2.5C. Then, line segment $\hat{P}_1\hat{Q}_1$ is considered to be a plane, which we call plane Z. We apply U^{-1} to the plane Z. Since U^{-1} is the map from H to $T(H)$ and $T(H)$ is a two-dimensional surface that has two constraint conditions (2.7) and (2.8) in the four-dimensional phase space, U^{-1} is applicable only to points in the plane Z that simultaneously satisfy the two conditions when the points are moved in the phase space in the time reverse direction using the equations of motion (2.1) and (2.2), as shown in Fig. 2.5C. These points determine $\dot{\varphi}$ in $T^{-1}(D_1 \cap R)$.

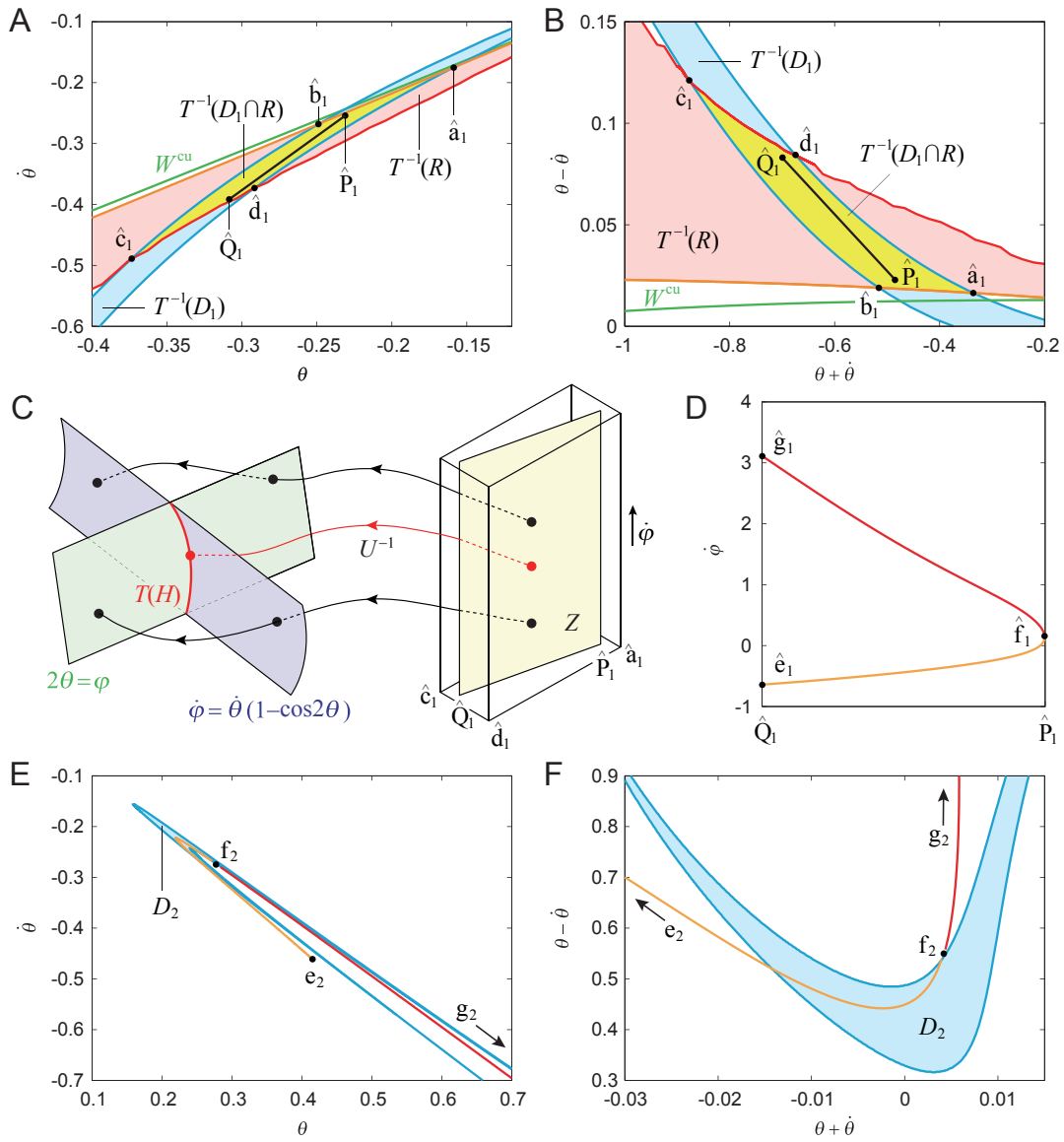

FIGURE 2.5: Characteristics of $S^{-1}(D_1 \cap R) = U^{-1}(T^{-1}(D_1 \cap R))$. A and B. $T^{-1}(D_1 \cap R)$ on H in the θ-$\dot{\theta}$ plane and the $(\theta + \dot{\theta})$-$(\theta - \dot{\theta})$ plane, respectively. C. Schematic diagram of applying U^{-1} to plane Z. D. Curve $\hat{e}_1\hat{f}_1\hat{g}_1$ in Z to which U^{-1} is applicable. E and F. Curve $e_2f_2g_2$ and D_2 in the θ-$\dot{\theta}$ plane and the $(\theta + \dot{\theta})$-$(\theta - \dot{\theta})$ plane, respectively.

Fig. 2.5D shows the result for the collection of the points in the plane Z indicated by the curve $\hat{e}_1\hat{f}_1\hat{g}_1$ to which U^{-1} is applicable. We obtained the curve $e_2f_2g_2$ by applying U^{-1} to this curve $\hat{e}_1\hat{f}_1\hat{g}_1$, as shown in Fig. 2.5E. (Fig. 2.5F uses $\theta + \dot{\theta}$ and $\theta - \dot{\theta}$ for the axes to clarify the geometric characteristics.) Note that $*_2$ (except for D_2), such as e_2, is used for D_2. In order to obtain the curves $e_2f_2g_2$ and $\hat{e}_1\hat{f}_1\hat{g}_1$ in Figs. 2.5D through 2.5F, we linearized the equations of motion (2.1) and (2.2) for θ and φ because the walking behavior appears around the saddle $[\gamma\,0\,0\,0]$. Therefore, there are differences from the exact solution, as the approximately obtained curve $e_2f_2g_2$ is not inside D_2 (Figs. 2.5E and 2.5F, see the appendix for details). The curve $e_2f_2g_2$, specifically the curve e_2f_2 is bent to be V-shaped, as shown in Fig. 2.5E. (Fig. 2.5F

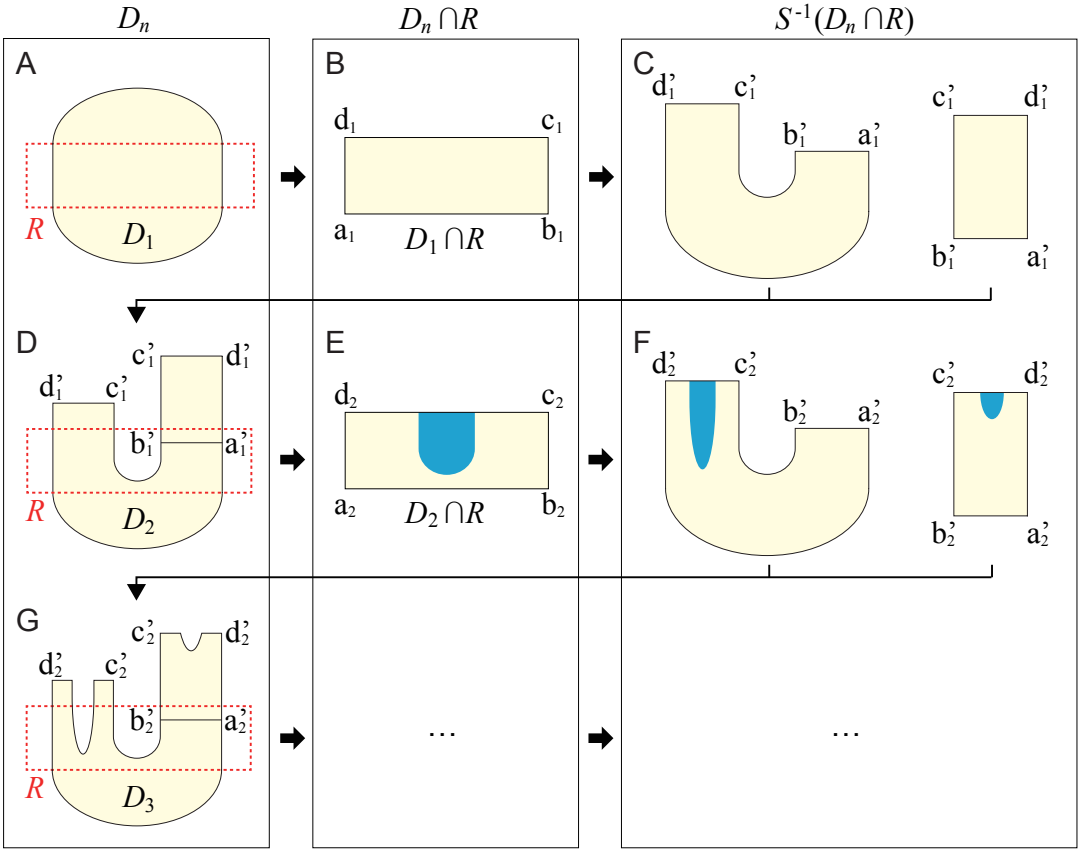

FIGURE 2.6: Schematic diagram of the process used to deform D_1 to D_2 and D_3 and generate slits. $D_1 \cap R$ is extracted from A in B. Two regions are generated by S^{-1} in C and are connected to form D_2 in D. In the same manner, $D_2 \cap R$ is extracted in E. Two regions are generated by S^{-1} in F and are connected to form D_3 in G.

uses $\theta + \dot{\theta}$ and $\theta - \dot{\theta}$ for the axes to clarify the geometric characteristics.)

In order to examine where in $D_1 \cap R$ the curve $e_2f_2g_2$ is moved from by $S^{-1}(= U^{-1} \circ T^{-1})$, we investigate where in $D_1 \cap R$ the curve $\hat{e}_1\hat{f}_1\hat{g}_1$ is moved from by T^{-1}. Since the curve $\hat{e}_1\hat{f}_1\hat{g}_1$ is in $T^{-1}(D_1 \cap R)$, the curve moves in $D_1 \cap R$ by T. Figs. 2.4D and 2.4E show the result indicated by the curve P_1Q_1. This shows that when S^{-1} is applied to the curve P_1Q_1 in $D_1 \cap R$, two curves f_2e_2 and f_2g_2 are obtained in $T(H)$. Since $D_1 \cap R$ is thin, as shown in Fig. 2.4D, the curve P_1Q_1 approximates $D_1 \cap R$. Therefore, the process to obtain the V-shaped curve $e_2f_2g_2$ from the curve P_1Q_1 explains the process by which $D_1 \cap R$ is transferred to D_2.

Figs. 2.6A through 2.6D show a schematic diagram of the summary by which to obtain D_2 from D_1. Specifically, $D_1 \cap R$ is extracted from D_1 (Fig. 2.6B), and two regions are generated by S^{-1}, one of which is stretched and bent (Fig. 2.6C left), and the other of which is only stretched (Fig. 2.6C right). These regions are connected at the boundaries $a_1'b_1'$ to form D_2 (Fig. 2.6D).

Next, we move to $D_3 = S^{-1}(D_2 \cap R)$. Since $D_2 \subseteq D_1$, the deformation from D_2 to D_3 (Figs. 2.6D through 2.6G) is the same as that from D_1 to D_2 (Figs. 2.6A through 2.6D). Since D_2 is V-shaped (Fig. 2.6D), the extracted $D_2 \cap R$ is also V-shaped and has

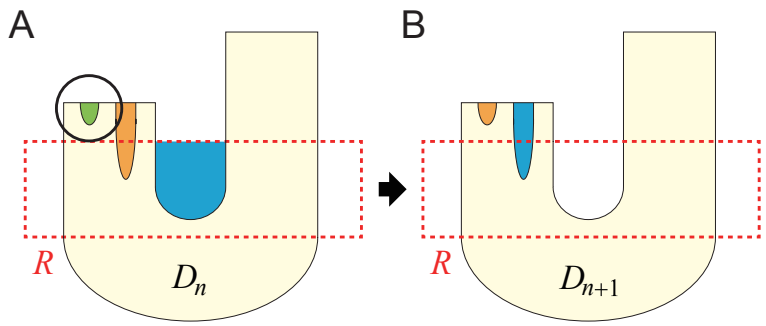

FIGURE 2.7: Unchanged number of slits. When (A) the generated slit in D_n does not reach R, (B) the number of slits remains unchanged in D_{n+1}.

a large slit at the boundary c_2d_2 (Fig. 2.6E). The large slit becomes slits at the boundary $c_2'd_2'$ in D_3 by the deformation (Figs. 2.6F and 2.6G). Although Fig. 2.6F(right) has a slit, it is far from R and so is ignored (Fig. 2.6G).

When the slit generated in D_n reaches, but does not penetrate, R, one slit is added in D_{n+1}, as observed in the process from D_2 to D_3. In contrast, when the generated slit in D_n does not reach R, the number of slits in D_{n+1} remains unchanged, as shown in Fig. 2.7. Moreover, since $D_{n+1} \subseteq D_n$, it is possible that the slit becomes deeper as n increases to reach R and create a new slit. Therefore, when the generated slit in D_n does not penetrate R, the number of slits of D_{n+1} increases by one or remains unchanged.

2.3.4 Appearance of a fractal

We consider the cases in which the generated slit in D_n penetrates R for the first time at $n = N$, as shown in Fig. 2.8A. (There may be multiple slits that do not penetrate $D_N \cap R$ to the left and right of the generated slit, but because they do not affect the explanation below, they are not shown in Fig. 2.8.) By applying S^{-1} to D_N in the same manner as in Fig. 2.6, a penetrating slit appears close to the outer edge of the V-shaped D_{N+1}, as shown in Fig. 2.8D. In addition, since $D_{n+1} \subseteq D_n$ once a slit penetrates R, the slit penetrates R for $n > N$. Furthermore, the penetrating slit close to the outer edge of D_{N+1} generates a slit that penetrates R near the right edge of $D_{N+1} \cap R$, as shown in Fig. 2.8E. As a result, a penetrating slit also appears close to the inner edge of the V-shaped D_{N+2}, as shown in Fig. 2.8G. Furthermore, the penetrating slit produces another penetrating slit in D_{N+3} near the slit generated by the large slit of D_{N+2} due to the V-shape, as shown in Fig. 2.8J. This slit also penetrates R. These penetrating slits produce new penetrating slits near the edge, and the number of slits increases at an accelerated rate as n increases. As a result, a fractal basin of attraction appears.

Figs. 2.9A through 2.9E show D_4 to D_8 for $\gamma = 0.013$. At $N = 5$, the generated slit penetrated R for the first time (Fig. 2.9B). After that, the penetrating slits were

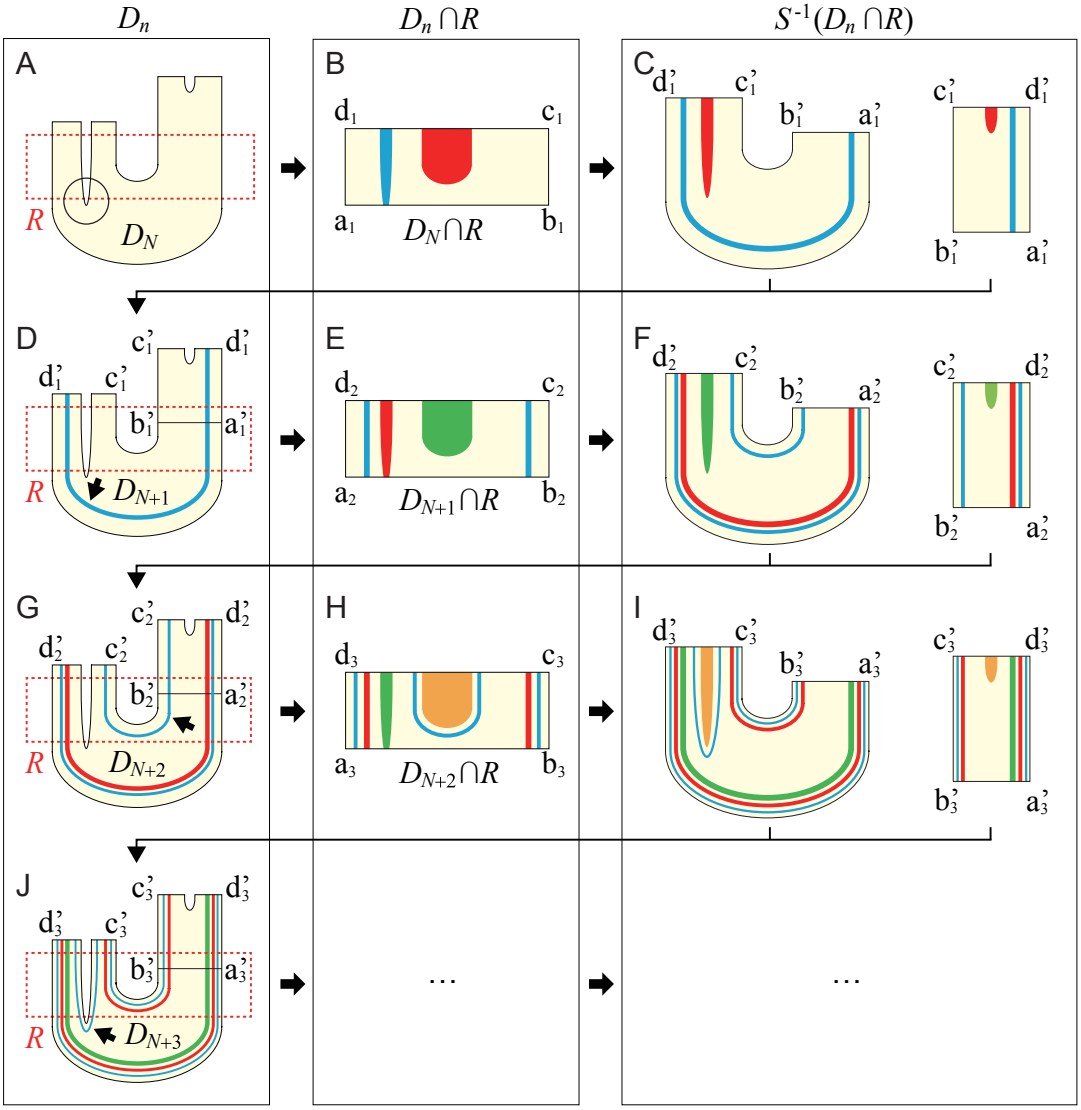

FIGURE 2.8: Schematic diagram of the process by which to deform D_n and generate penetrating slits after the generated slit penetrates R for the first time at $n = N$ in A. A penetrating slit is generated close to the outer edge in D_{N+1} in D. A penetrating slit is generated close to the inner edge in D_{N+2} in G. A penetrating slit is generated close to the generated slit in D_{N+3} in J.

generated close to the outer edge at $n = 6$ (Fig. 2.9C), near the inner edge at $n = 7$ (Fig. 2.9D), and close to the generated slit at $n = 8$ (Fig. 2.9E) in that order. Therefore, infinitely many slits are generated and the fractal basin of attraction appears, as shown in Figs. 2.3C and 2.3D.

2.3.5 No fractal appears

Next, we consider the cases in which no slits in D_n penetrate R, even when S^{-1} is applied several times. In particular, suppose that n is so large that D_n converges and also suppose that D_n has a slit that does not reach R. In this case, since the number

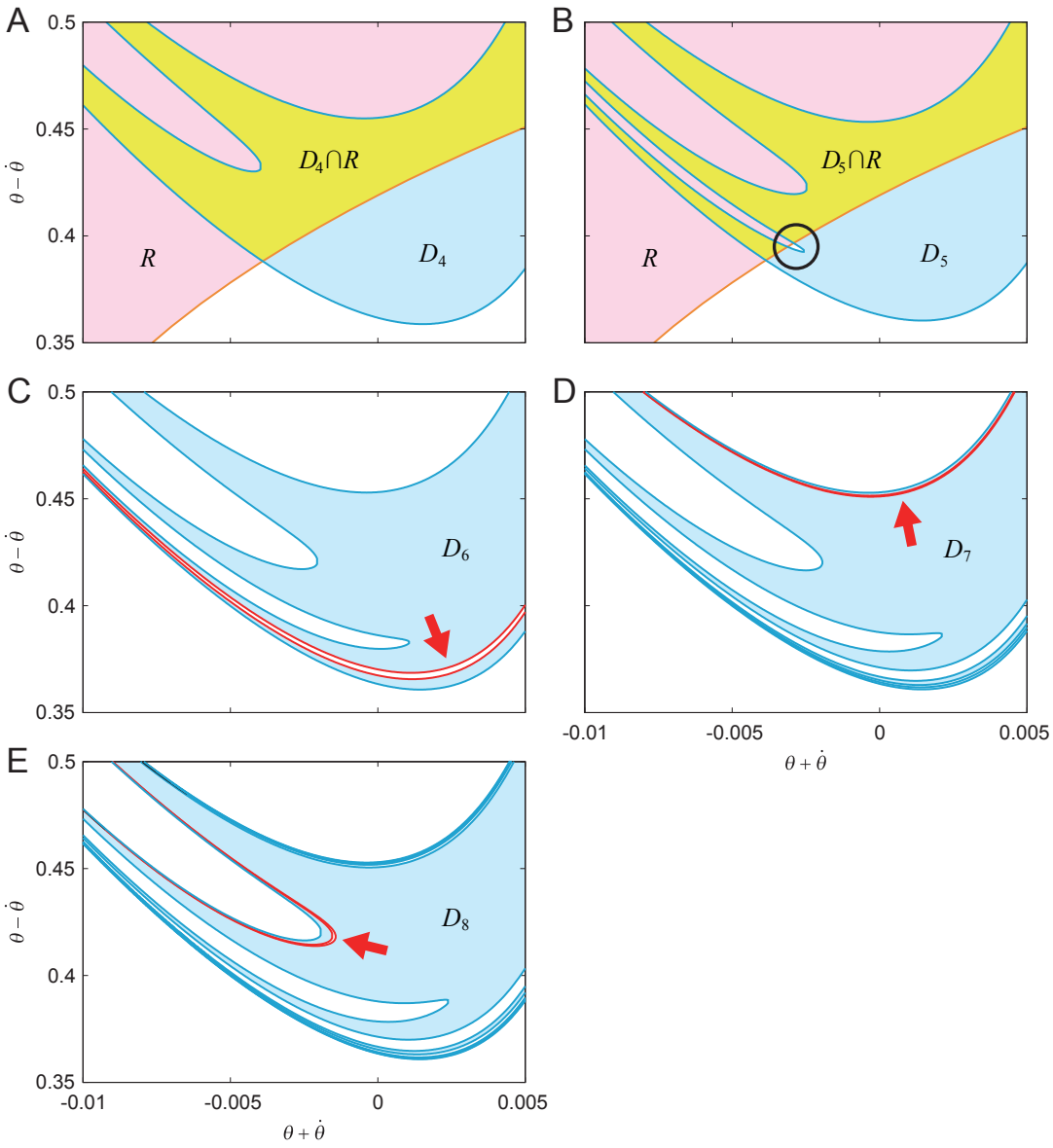

FIGURE 2.9: D_4 to D_8 for $\gamma = 0.013$. A. No slit penetrates R. B. The generated slit penetrates R for the first time. C. A penetrating slit is generated close to the outer edge of D_6. D. A penetrating slit is generated close to the inner edge of D_7. E. A penetrating slit is generated close to the generated slit of D_8.

of slits does not change even when S^{-1} is applied, the basin of attraction does not have a fractal structure and has a finite number of slits.

Figs. 2.10A and 2.10B show D_{50} and D_{51}, respectively, for $\gamma = 0.001$. Here, D_{50} has four slits, and the leftmost slit does not reach R. As a result, D_{51} has four slits as in D_{50}. In addition, D_{50} and D_{51} have no difference and are identical to the basin of attraction (Fig. 2.3B), which we confirmed by comparing the regions using $10^4 \times 10^4$ initial states, and so converge. Therefore, the basin of attraction does not have a fractal structure.

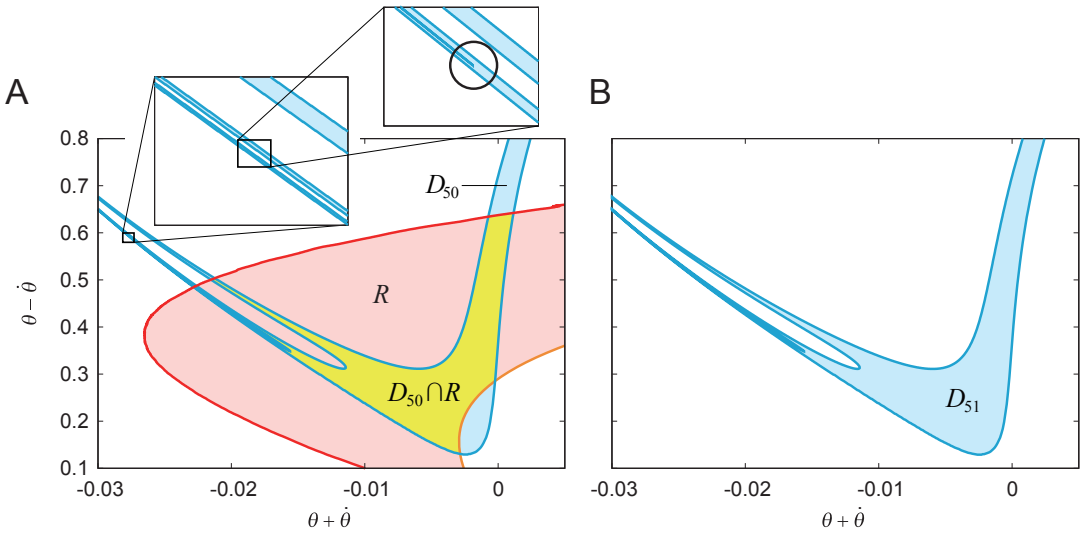

FIGURE 2.10: No appearance of fractal. A and B. D_{50} and D_{51}, respectively, for $\gamma = 0.001$. The generated slit in D_{50} does not reach R. D_{50} and D_{51} have the same shape and converge. The number of slits never increases.

2.4 Discussion

2.4.1 Stability and basin of attraction

Bipedal walking has intrinsic instability due to saddle dynamics, and clarifying the mechanism by which walking can be stabilized is important. Passive dynamic walking is a useful model to examine the mechanism from a dynamic viewpoint. In order to clarify the stabilization mechanism, investigating both the stability and basin of attraction is crucial. However, while previous studies have focused on the stability by the eigenvalue analysis of the linearized Poincaré map around the fixed point on the Poincaré section [16, 36, 40, 49, 58, 118, 130, 131], the basin of attraction has not been well studied. This is partly because while eigenvalue analysis allows us to easily investigate the stability, no general analytical method has been provided for investigating the basin of attraction. We used an analytical approach based on dynamical systems theory to clarify a specific property embedded in the basin of attraction, which is useful to further investigate the characteristics of the basin of attraction in walking. While passive dynamic walking has no control or input, the use of control and input changes the dynamic characteristics of walking and also varies the stability and the basin of attraction [7, 8, 94, 96, 114]. We would like to improve and clarify our analysis in the future.

2.4.2 Initial-value sensitivity and convergence to attractor

The Poincaré map S represents walking one step, and slits are generated by applying the inverse image S^{-1} many times to the region from which the model walks at least one step. These slits come from the large slit of the V-shaped D_2 (Fig. 2.6).

When there are only a finite number of slits in the basin of attraction, the generated slit in D_n does not reach R and is not used in D_{n+1} (Fig. 2.7). Therefore, these slits are not stretched much. In contrast, once the generated slit in D_n penetrates R, the generated slits for $n \geq N$ are stretched greatly and create stripe patterns by producing penetrating slits, especially close to the basin boundary (Fig. 2.8). These penetrating slits become thinner as n increases. Since slits indicate a region in which the model will fall down, whether the model continues to walk or not becomes very sensitive around the basin boundary. Furthermore, since penetrating slits become thinner, two states located at different sides of the large slit of D_2 become closer as S^{-1} is applied to the two states many times. This means that two states located at different sides of a thin slit in the basin of attraction move away from each other as S is applied many times and the two states come to reach different sides of the large slit of D_2.

When the basin of attraction is fractal, there are infinitely many penetrating slits close to the basin boundary. Therefore, when the model walks from an initial state near the boundary on the basin of attraction, there are numerous penetrating slits between the initial state and the attractor, and the model must traverse the slits for the state to approach the attractor. The model must walk at least the steps that are required to generate the penetrating slits by applying S^{-1}. Therefore, the model takes a long time to approach the attractor, depending on the initial state.

2.4.3 Limitations of our analysis

In the present study, we clarified that the fractal basin of attraction appears when the generated slit in D_n penetrates R and that fractal basin of attraction does not appear when the generated slit in D_n does not reach R for an n so large that D_n converges. However, it is possible that the generated slit in D_n reaches, but does not penetrate, R for so large n that D_n converges. In this case, although it is not at an accelerated rate, the number of slits increases as n increases. While infinitely many slits appear in the basin of attraction, no penetrating slits are generated. Although our analysis does not exclude this possibility, our simulation results did not show such a case for any γ.

We used the simplest walking model for the analysis of passive dynamic walking, i.e., we assumed the extreme case $m/M \to 0$ and $b/l \to 1$ for the compass-type model [36]. Therefore, we did not explain the mechanism of the basin of attraction for general models of passive dynamic walking. However, the period-doubling cascade to chaos appears and the fractal basin of attraction is observed without the period doubling even when the extreme case is not assumed [2]. This suggests that similar mechanisms to those observed herein are embedded in general models of passive dynamic walking.

2.4.4 Biological relevance

The fractal appears in human walking, especially in the gait rhythm [39, 53–55]. However, unlike passive dynamic walking, human walking is generated through the control. The basin of attraction of compass-type models used in passive dynamic walking is enlarged by the control and the number of slit changes [93, 96, 114]. However, the stance leg during human walking is almost straight and rotates around the foot contact point like an inverted pendulum [90]. In addition, the stance and swing legs are switched by the foot contact and lift off. Therefore, saddle instability and hybrid properties are inevitable in the gait dynamics, as in passive dynamic walking, and the stretching and bending deformation remains crucial for the formation mechanism of basin of attraction. In fact, our previous study [93, 96] showed that even when a controller inspired by spinal central pattern generators [98] is incorporated in a compass-type model, the basin of attraction has slits due to the deformation.

Human walking is generated through the central nervous system and the body mechanical system. Fractal properties are reduced by aging and pathological disorders such as Parkinson's and Huntington's diseases [39, 53]. A simple neuromechanical model demonstrated that fractal properties are reduced by changing the motor control model to emulate the pathological disorder [31]. These properties suggest that the neural system contributes to the fractal in human walking. In contrast, the body mechanical system also has potential to contribute to the fractal in human walking. Passive dynamic walking exhibits a chaos attractor depending on the model parameter [36, 40] and shows a fractal basin of attraction even for the single attractor as shown in the present study. The steady state of a dynamical system with a single attractor never shows a fractal, but instead shows regular behavior, unless the system is disturbed. However, when the dynamical system is specific and has a fractal basin of attraction, fractal behavior can be induced by a disturbance or noise without fractal properties. In fact, the fractal appears in walking of compass-type models with a controller and noise without fractal properties [1, 38]. Even for passive dynamic walking, the mechanisms for fractal and non-fractal basins of attraction clarified in the present study will provide useful insights for understanding human walking. The analysis of measured human data has limitations for elucidating the underlying mechanism in human walking, and physical models are useful to overcome the limitations.

Chapter 3

Mechanism of changes in spatial fractal in basin of attraction in passive dynamic walking

3.1 Introduction

A passive dynamic walker is a mechanical system that walks down a slope without any control [85], and gives useful insights into the dynamic mechanism of stable walking. This system has been used extensively for the study of human walking with low energy consumption [12,15,23,60,71–73,91,110,119] and has been the basis for the design of energy-efficient bipedal robots [8,9,17,18,58,70,89,130,131]. Because the walking speed for this system changes with slope angle, it is important to clarify its influence on walking. In particular, this system shows specific characteristics due to nonlinear dynamics depending on the slope angle. For example, a chaotic attractor appears through a period-doubling cascade when the slope angle increases [40], and it abruptly disappears at a critical slope angle [47,94]. Furthermore, fractal basin boundaries appear even without period-doubling [2,94,112]. To understand the dynamics that generate walking, it is important to elucidate the mechanism for these characteristics.

The change in the attractor by the slope angle and its mechanism have been clarified in previous studies [35, 36, 40, 47–49], whereas the change in the basin of attraction and its mechanism remain largely unclear. In our previous studies [94, 97], we showed that the basin of attraction is produced through iterative stretching and bending deformation by the inverse image of the Poincaré map. As a result, the basin boundaries become fractal when the slope angle exceeds a critical value. However, other characteristics of the basin of attraction remain unclear.

In this study, we focused on the size, fractality, and disappearance of the basin of attraction. Because the basin of attraction is the set of initial states that converge to an attractor, the basin size indicates the robustness of walking and is thus an important feature for walking. The fractal basin boundary has a final state sensitivity [41, 84]. This means that even when the system is deterministic, unpredictability exists for the attractor or final state when the initial condition contains uncertainties. Although

the unpredictability of chaotic attractors has been investigated based on the initial-state sensitivity [36, 40], the final state sensitivity in fractal basin boundaries has not been investigated thoroughly. The final state sensitivity makes the prediction of walking easily affected by inevitable noise and is thus also an important feature for walking. The disappearance of the chaotic attractor and its basin of attraction indicates that the system cannot produce stable walking and falls down regardless of the initial state. While the disappearance of the chaotic attractor can be explained by a boundary crisis [47, 94], the mechanism for the disappearance of the basin of attraction remains unclear.

The stretching-bending deformation revealed in our previous study [97] creates horseshoes [115] that cause complex phenomena, such as chaos and fractals, and is an important property in nonlinear dynamics. It is expected to play an important role in determining the size, fractality, and disappearance of the basin of attraction in passive dynamic walking. In the present study, we first calculated the size and fractality of the basin of attraction for passive dynamic walking depending on the slope angle using the simplest walking model, which is useful for the analysis of passive dynamic walking, and found sharp changes in these parameters at specific slope angles. We then clarified the mechanism for the sharp changes and disappearance of the basin of attraction based on stretching-bending deformation in the basin of attraction by improving our previous analysis [97].

3.2 Passive dynamic walking

3.2.1 Model

In this study, we analyzed passive dynamic walking using the simplest walking model [36] (Fig. 3.1). This model has two legs, swing and stance legs, connected by a frictionless hip joint and walks down a slope of angle γ without any control. The leg length is l. The tip of the stance leg is fixed on the slope, and the stance leg rotates around the leg tip without friction. The angles between the stance leg and slope normal and between the stance and swing legs are denoted by θ and φ, respectively. The hip mass and leg tip mass are M and m, respectively. We assumed $m/M \to 0$ as in [36]. The gravitational acceleration is g.

3.2.2 Governing equations

This model is governed by hybrid dynamics that consist of continuous dynamics generated by the equations of motion when the swing leg is in motion and discontinuous dynamics generated by the impact when the foot makes contact with the ground.

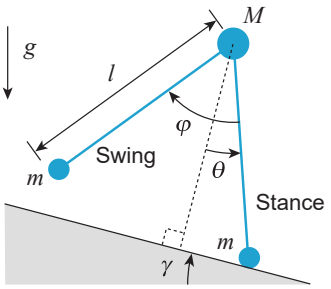

FIGURE 3.1: Simplest walking model for analysis of passive dynamic walking.

The equations of motion are given by

$$\ddot{\theta} - \sin(\theta - \gamma) = 0 \tag{3.1}$$

$$(\cos\varphi - 1)\ddot{\theta} + \ddot{\varphi} - \dot{\theta}^2 \sin\varphi + \sin(\varphi - \theta + \gamma) = 0. \tag{3.2}$$

The equations are made dimensionless by the timescale $\sqrt{l/g}$. The swing leg tip touches the slope (touchdown) when the following conditions are satisfied:

$$2\theta - \varphi = 0 \tag{3.3}$$

$$\theta < 0 \tag{3.4}$$

$$2\dot{\theta} - \dot{\varphi} < 0. \tag{3.5}$$

We utilized the condition (3.4) to ensure that touchdown takes place exclusively in front of the model to move forward, and condition (3.5) to disregard the scuffing of the leg tip on the slope when the swing leg moves forward. We considered the touchdown as a completely inelastic collision, where no slip or bounce occurs, and assumed that the stance leg lifts off without interaction just after touchdown. Because the roles of the swing and stance legs are reversed just after touchdown, we obtain

$$\begin{bmatrix} \theta^+ \\ \dot{\theta}^+ \\ \varphi^+ \\ \dot{\varphi}^+ \end{bmatrix} = \begin{bmatrix} -\theta^- \\ \dot{\theta}^- \cos 2\theta^- \\ -2\theta^- \\ \cos 2\theta^- \,(1 - \cos 2\theta^-)\,\dot{\theta}^- \end{bmatrix} \tag{3.6}$$

where the notations $*^-$ and $*^+$ indicate the state of $*$ just before and after touchdown, respectively. The key aspect of this relationship is that the state just after touchdown, denoted by $(\theta^+, \dot{\theta}^+, \varphi^+, \dot{\varphi}^+)$, depends solely on $(\theta^-, \dot{\theta}^-)$ and is not influenced by $(\varphi^-, \dot{\varphi}^-)$.

3.2.3 Structure of phase space by hybrid dynamics

The structure of the phase space is determined by the hybrid dynamic system, as shown in Fig. 3.2A. The section H is defined by the touchdown conditions (3.3)–(3.5) and forms a three-dimensional space in four-dimensional phase space. The

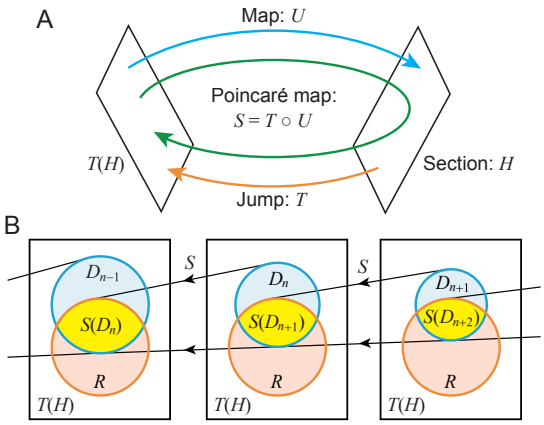

FIGURE 3.2: Schematic diagram of the structure of phase space. (A) Hybrid dynamics composed of the section H, jump T, map U, and Poincaré map S. (B) Relationship among the regions D_n and $S(D_n)$, and the range R of S on $T(H)$.

jump T in the phase space from the state just before touchdown to the state just after touchdown is defined by (3.6). Therefore, the image of T, $T(H)$, represents all states just after touchdown, and a new step starts from $T(H)$. The map U is defined by the equations of motion (3.1) and (3.2) from the start of a step to the next touchdown instance, i.e., from $T(H)$ to H. The Poincaré section is defined as $T(H)$ and the Poincaré map S is defined by $S = T \circ U : T(H) \to T(H)$, which represents one step. $T(H)$ is two-dimensional in the simplest walking model as shown in (3.6), which is useful for analyzing S. S is parameterized only by the slope angle γ and an attractor of S represents stable walking. In particular, S has an attracting fixed point at $0 < \gamma < 0.015$, and there is a period-doubling cascade to chaos for $0.015 < \gamma < 0.019$ [36]. While the basin of attraction of S has smooth boundaries for $\gamma < 0.0075$, it has fractal boundaries for $\gamma > 0.0075$ [97].

3.3 Characteristics of basin of attraction

3.3.1 Basin size

Because the basin of attraction is the collection of initial conditions on $T(H)$ from which the model keeps walking, we computed the basin using the governing equations (3.1)–(3.6). Specifically, we used 1560 bins for $0.1 < \theta \leq \pi/2$ with increments of 0.001 and 1500 bins for $-1.5 < \dot{\theta} \leq 0$ with increments of 0.001 for the initial conditions on $T(H)$; that is, we used 2.34×10^6 initial conditions in total. This range of θ and $\dot{\theta}$ was sufficient to contain the basin of attraction irrespective of γ. We approximated the basin of attraction by the set of initial states from which the model can walk at least 50 steps, and determined the size of the basin of attraction by counting the number of initial conditions within it.

Figure 3.3A shows the basins of attraction for $\gamma = 0.01$, 0.012, and 0.016, where $\theta + \dot{\theta}$ and $\theta - \dot{\theta}$ are used for the axes to clarify the geometric characteristics as in [93,

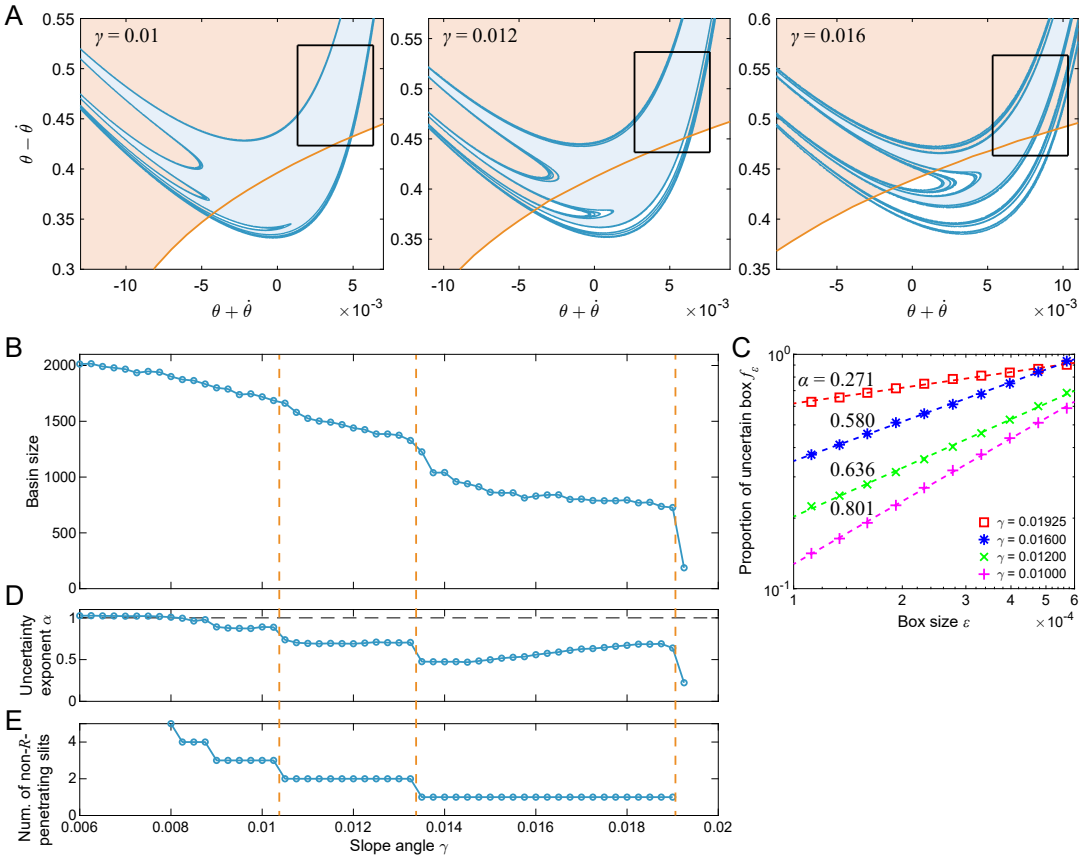

FIGURE 3.3: Basin of attraction for γ. (A) Basin of attraction for $\gamma = 0.01$, 0.012, and 0.016. Blue and orange lines show the boundaries of the basin of attractions and the lower edge of range R, respectively. Black lines show the regions used to calculate the uncertainty exponent α: $(\theta + \dot{\theta} \times \theta - \dot{\theta}) = [0.00133, 0.00633] \times [0.4233, 0.5233]$ for $\gamma = 0.010$, $[0.00266, 0.00766] \times [0.4366, 0.5366]$ for $\gamma = 0.012$, and $[0.00533, 0.01033] \times [0.4633, 0.5633]$ for $\gamma = 0.016$. (B) Basin size versus γ. (C) Proportion of uncertainty box f_ε versus ε for various γ values. Dotted lines represent corresponding linear regression lines. (D) Uncertainty exponent α versus γ. (E) Number of non-R-penetrating slits versus γ.

94, 97]. Because $\gamma > 0.0075$ in these figures, the basins have an infinite number of slits and fractal boundaries [97]. The size of the basin decreases as γ increases, as shown in Fig. 3.3B. In particular, it abruptly decreases around $\gamma = 0.0103$, 0.0135, and 0.019.

3.3.2 Fractality of basin boundary

We evaluated the fractality of the basin boundary based on the uncertainty exponent [41, 84], which is defined as follows:

$$\alpha = \dim(B) - \dim(\partial B) \tag{3.7}$$

where α is the uncertainty exponent, B is the basin of attraction, ∂B is the basin boundary, and $\dim(\xi)$ is the dimension of set ξ. If $0 < \alpha < 1$, the basin boundary

has a non-integer dimension and is fractal.

We calculated the uncertainty exponent α using a previously reported method [41,84]. First, we placed many squares with a length ε, which is sufficiently larger than the bin size in the initial conditions, randomly on a limited range of the Poincaré section. We calculated the proportion f_ε of the squares that touch the basin boundary. When the square is coarse-grained as a single point, it is "uncertain" whether the point is inside or outside the basin. Therefore, α describes not only the fractality but also the final state sensitivity. The following relationship between α and ε holds:

$$f_\varepsilon \propto \varepsilon^\alpha. \tag{3.8}$$

Therefore, we can obtain α by calculating the slope of the linear regression line for f_ε versus ε using a log-log plot.

We placed 30,000 squares randomly in a limited region to calculate α, as shown in Fig. 3.3A. Because the basin of attraction moves depending on γ, the limited region moves in the same way as the basin of attraction. However, the area of the limited region is identical for all γ. Figure 3.3C shows f_ε versus ε for $\gamma = 0.01$, 0.012, 0.016, and 0.01925, and linear regression lines using a log-log graph. We obtained the uncertainty exponent α from the coefficient for this regression. Figure 3.3D shows a plot of α versus γ. When $\gamma < 0.008$, the basin boundary is not fractal because $\alpha \approx 1$. When $\gamma > 0.008$, the basin boundary becomes fractal because $0 < \alpha < 1$. We can find dramatic changes in α at certain values of γ, which include $\gamma \approx 0.0103, 0.0135$, and 0.019, where the basin size shows remarkable changes in Fig. 3.3C.

3.4 Mechanism for sharp changes in the basin of attraction

3.4.1 Formation of basin of attraction through stretch-bending deformation by S^{-1}

We introduce the notation D_n $(n = 1, 2, \ldots)$ to denote the set of initial conditions on the Poincaré section $T(H)$ from which the model walks at least n steps. As n increases to infinity, D_n approximates the basin of attraction. Furthermore, this set satisfies $D_{n+1} \subseteq D_n$ (Fig. 3.2B), which means that if the initial condition is in D_n but not in D_{n+1}, the model will fall down at the $(n+1)$th step. In our previous study [97], we showed that $S(D_n)$ represents the state on $T(H)$ after the model walked one step starting from D_n, which is in D_{n-1} (Fig. 3.2B) because the Poincaré map S represents walking one step. Moreover, $S(D_n)$ is also in the range R of S, which is given by $R = S(D_1)$ because D_1 is the domain of S. Therefore, the following condition is satisfied: $S(D_n) = D_{n-1} \cap R$, which gives

$$D_n = S^{-1}(S^{-1}(\cdots(S^{-1}(D_1 \cap R) \cap R)\cdots \cap R) \cap R). \tag{3.9}$$

This indicates that the basin of attraction is obtained by iterative processes to extract the intersection with R of S and to apply the inverse image S^{-1} starting from D_1. Because saddle instability due to the inverted pendulum induces a stretching-bending effect in S^{-1} [94, 97], D_1 is stretched and bent many times to create many slits (Fig. 3.4).

Suppose that a slit (red) in D_n penetrates the lower edge of R for the first time at $n = N$, as shown in Fig. 3.5A. By applying S^{-1} to $D_N \cap R$ (Fig. 3.5B) in the same manner as in Fig. 3.4, the slit penetrates the U-shaped D_{N+1} along and near the outer edge (Fig. 3.5C). When a slit penetrates D_n, we call it a D_n-penetrating slit. When it does not, we call it a non-D_n-penetrating slit. The D_n-penetrating slit in D_{N+1} corresponds to two slits near the left and right edges in $D_{N+1} \cap R$ (Fig. 3.5D). The right slit penetrates D_{N+2} along and near the inner edge and surrounds the slit (blue) generated by the inner edge (Fig. 3.5E). Because these slits do not penetrate R, they remain in $D_{N+2} \cap R$ (Fig. 3.5F) and D_{N+3} (Fig. 3.5G). However, these two slits in D_{N+3} penetrate R and one of them (red) corresponds to two slits in $D_{N+3} \cap R$ (Fig. 3.5H). The number of slits increases at an accelerated rate as n increases, and some slits are surrounded by many D_n-penetrating slits (Fig. 3.5I). Through these procedures, the basin boundaries become fractal in $\gamma > 0.0075$.

3.4.2 Comparison of basin state before and after sharp changes in its characteristics

Figures 3.6A and B show the basin of attraction at $\gamma = 0.0134$ (before the sharp changes in the basin characteristics at $\gamma \approx 0.0135$) and $\gamma = 0.0136$ (after the sharp changes), respectively. In the specific region of each figure, we used at least 1500×1500 initial conditions to obtain accurate boundaries, which was confirmed by investigating if the boundary remained unchanged even when we used 3000×3000 initial conditions (we used the same conditions to calculate D_n in the following sections). As shown in the enlarged figures, a purple non-D_n-penetrating slit is surrounded by D_n-penetrating slits. While these slits do not reach the lower edge of the range R in Fig. 3.6A, many slits reach and penetrate the lower edge of R in Fig. 3.6B. This difference could cause the sharp changes in the basin characteristics.

When the basin boundaries become fractal ($\gamma > 0.0075$), non-D_n-penetrating slits are surrounded by D_n-penetrating slits through the formation process for the basin of attraction, as shown in Figs. 3.5E and G. For large enough n, D_n has many such D_n-penetrating slits and consists of an infinite number of regions separated by the D_n-penetrating slits. We define $D_n = \bigcup_{i=1}^{\infty} D_n^i$ as shown in Fig. 3.7A, where D_n^i ($i = 1, 2, \dots$) is the separated region and D_n^1 contains the attractor. If a non-D_n-penetrating slit in D_n^1 reaches and penetrates the lower edge of R, we call it a R-penetrating slit (Fig. 3.7B). If it does not penetrate the lower edge, we call it a non-R-penetrating slit.

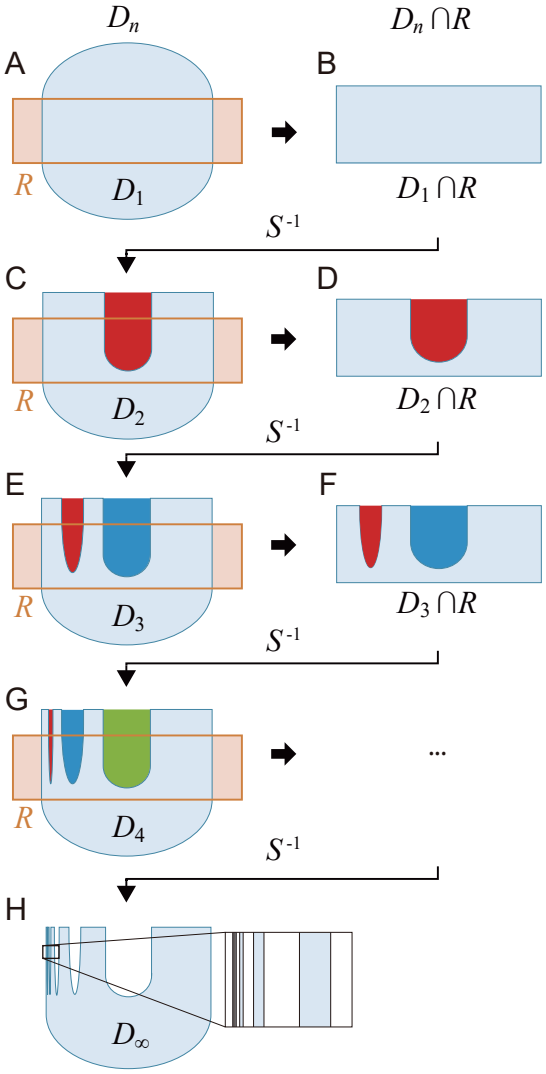

FIGURE 3.4: Schematic diagram of process to deform D_1 to D_2, to $D_3, \cdots$, to D_∞ and generate slits. $D_1 \cap R$ (B) is extracted from D_1 (A) and stretched and bent by S^{-1} to form U-shaped D_2 with one slit (C). In the same way, $D_2 \cap R$ is extracted (D) and stretched and bent by S^{-1} to form D_3 with two slits (E). $D_3 \cap R$ is extracted (F) and stretched and bent by S^{-1} to form D_4 with three slits (G). D_∞ has many slits through this process (H).

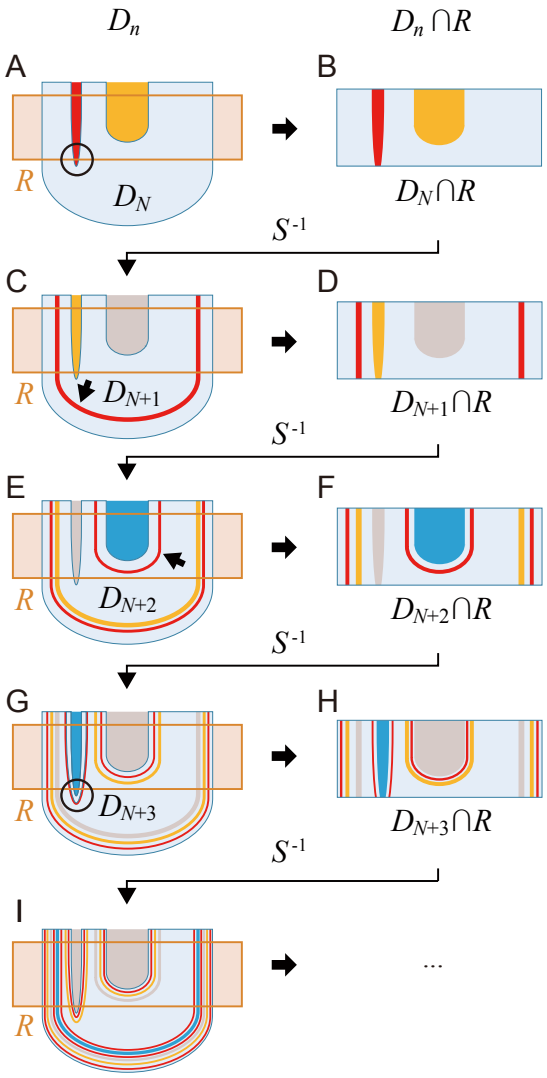

FIGURE 3.5: Formation process for fractal basin of attraction. When a red slit in D_N penetrates the lower edge of the range R for the first time (A), $D_N \cap R$ is separated into two regions (B). D_{N+1} has a red D_n-penetrating slit near the outer edge (C) and it is separated into two red slits in $D_{N+1} \cap R$ (D). D_{N+2} and $D_{N+2} \cap R$ have a red D_n-penetrating slit, which surrounds the center blue slit (E, F). D_{N+3} has a red D_n-penetrating slit, which surrounds a blue slit and penetrates the lower edge of R (G), and it is also separated into two red slits in $D_{N+3} \cap R$ (H). These slits produce new penetrating slits, and the number of slits increases at an accelerated rate as n increases after D_{N+4} (I).

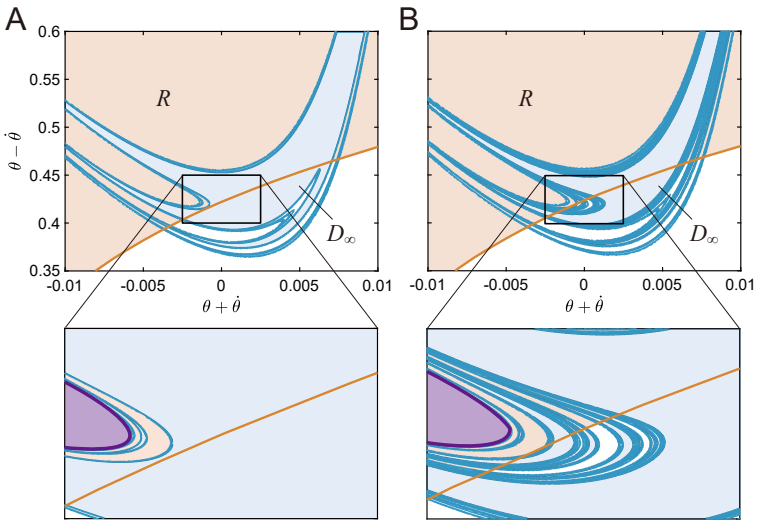

FIGURE 3.6: Penetration of the lower edge of the range R by D_n-penetrating slits in the basin of attraction at $\gamma \approx 0.0135$. (A) $\gamma = 0.0134$ (before penetration). (B) $\gamma = 0.0136$ (after penetration). The orange and blue regions are R and the basin of attraction D_∞, respectively. The orange, blue, and red lines are the boundaries of R, D_∞, and D^1_∞, respectively.

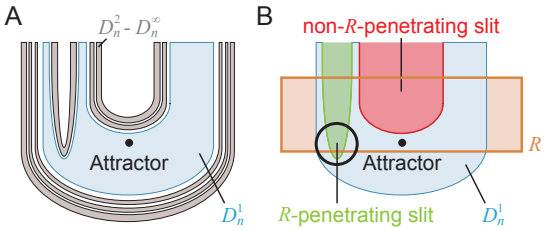

FIGURE 3.7: Regions and slits when basin boundaries become fractal. (A) D_n is separated into D_n^i $(i = 1, 2, \ldots, \infty)$ by D_n-penetrating slits, where D_n^1 contains the attractor. (B) R-penetrating and non-R-penetrating slits in D_n^1. A R-penetrating slit reaches and penetrates the lower edge of R and a non-R-penetrating slit does not.

In Fig. 3.3A, we can find three non-R-penetrating slits in $D^1_{50}(\approx D^1_\infty)$ for $\gamma = 0.01$, two for $\gamma = 0.012$, and one for $\gamma = 0.016$, which means that the number of non-R-penetrating slits decreases as they penetrate R through the increase of γ. Figure 3.3E shows the number of non-R-penetrating slits versus γ and confirms that it decreases as γ increases. There could be an infinite number of non-R-penetrating slits for $\gamma \approx 0.0075$, where fractal basin boundaries appear. By comparing Figs. 3.3C–E, we can find that when the number of non-R-penetrating slits changes, the basin characteristics sharply change.

3.4.3 Mechanism for sharp changes in basin characteristics based on the number of non-R-penetrating slits

Because the basin of attraction is the set of initial states that asymptotically converge to an attractor, any state in the basin of attraction moves toward the attractor by

repeated application of S. That is, the basin of attraction is obtained by the iterative application of the inverse image S^{-1} to the proximity of the attractor. Therefore, the formation process for the basin of attraction can be explained by the iterative application of S^{-1} not only to D_n as in Figs. 3.4 and 3.5, but also to D_n^1 that contains the attractor.

We investigated the relationship between the sharp change in the basin characteristics with γ and the change in the number of non-R-penetrating slits in D_∞^1. First, we examined how the number of slits increases in the formation process for the basin of attraction by focusing on the deformation of D_n^1 with n when the basin boundary is not fractal, when it is fractal with one non-R-penetrating slit, and when it is fractal with two non-R-penetrating slits. Second, we investigated the mechanism for the sharp changes in the basin characteristics when the number of non-R-penetrating slits decreases from 2 to 1. Finally, we determined that this mechanism is applicable when the number of non-R-penetrating slits decreases from $k+1$ to k ($k = 1, 2, \dots$).

Increase of number of slits in formation process for basin of attraction for n

First, we investigated how the number of slits increases in the formation process for the basin of attraction when no slit reaches the lower edge of R and the basin boundary is not fractal as in Fig. 3.4 ($\gamma < 0.0075$). Although a red slit in D_2 in Fig. 3.4C is stretched and bent by S^{-1}, it never reaches the lower edge of R and there is only one red slit in both D_3 in Fig. 3.4E and D_4 in Fig. 3.4G. No matter how many times S^{-1} is applied, there is only one red slit in D_n ($n \geq 2$).

Second, we investigated how the number of slits increases when the basin boundary is fractal and there is one non-R-penetrating slit in D_∞^1 ($0.0135 < \gamma < 0.019$). Because the formation process for the basin of attraction is explained by D_n^1, Fig. 3.5 explains the basin formation for one non-R-penetrating slit by replacing D_N by D_N^1 in Fig. 3.5A. We define $\hat{D}_n^1$ ($n \geq N+1$) as the region obtained by applying S^{-1} to D_N^1. Fig. 3.5A shows one red R-penetrating slit and one yellow non-R-penetrating slit in D_N^1. The red R-penetrating slit generates red D_n-penetrating slits in $\hat{D}_{N+1}^1$, $\hat{D}_{N+2}^1$, and $\hat{D}_{N+3}^1$ in Figs. 3.5C, E, and G, respectively. Because these D_n-penetrating slits also reach and penetrate the lower edge of R, these slits are divided into two slits in $\hat{D}_{N+1}^1 \cap R$, $\hat{D}_{N+2}^1 \cap R$, and $\hat{D}_{N+3}^1 \cap R$ in Figs. 3.5D, F, and H, respectively. Therefore, the number of red D_n-penetrating slits increases one by one in $\hat{D}_{N+1}^1 \to \hat{D}_{N+2}^1 \to \hat{D}_{N+3}^1$ (one red slit in $\hat{D}_{N+1}^1$, two red slits in $\hat{D}_{N+2}^1$, and three red slits in $\hat{D}_{N+3}^1$). In addition, $\hat{D}_{N+3}^1$ has a red D_n-penetrating slit, which surrounds a blue R-penetrating slit and penetrates the lower edge of R as shown in Fig. 3.5G. This red slit is also divided into two slits in $\hat{D}_{N+3}^1 \cap R$, as shown in Fig. 3.5H. Therefore, while the number of red slits increases one by one in $\hat{D}_{N+1}^1 \to \hat{D}_{N+2}^1 \to \hat{D}_{N+3}^1$, it increases by two in $\hat{D}_{N+3}^1 \to \hat{D}_{N+4}^1$. In addition, the red slits divided in $\hat{D}_{N+3}^1 \cap R$ generate two D_n-penetrating slits in $\hat{D}_{N+4}^1$ (Fig. 3.5I), each of which is also divided into

two slits in $\hat{D}^1_{N+4} \cap R$. These findings indicate that the number of red slits increases at an accelerating rate by two effects: a D_n-penetrating slit at the left of $\hat{D}^1_n$ is divided into two slits in $\hat{D}^1_n \cap R$ and a D_n-penetrating slit surrounding a R-penetrating slit is divided into two slits in $\hat{D}^1_n \cap R$. Figure 3.8 shows the formation process for the basin of attraction for $\gamma = 0.018$, where the basin boundary is fractal and there is one non-R-penetrating slit. A non-D_n-penetrating slit penetrates the lower edge of R in D_4 ($N = 4$, $D^1_4 = D_4$). A D_n-penetrating slit surrounds the R-penetrating slit in D_7 ($N + 3 = 7$, $\hat{D}^1_7 = D_7$), which penetrates the lower edge of R and is divided into two slits in $D_7 \cap R$.

Finally, we investigated how the number of slits increases when the basin boundary is fractal and there are two non-R-penetrating slits in D^1_∞ ($0.0103 < \gamma < 0.0135$). Figure 3.9 explains the basin formation process for two non-R-penetrating slits. Fig. 3.9A shows one red R-penetrating slit and one blue and one purple non-R-penetrating slits in D^1_N. The red R-penetrating slit generates red D_n-penetrating slits in $\hat{D}^1_{N+1}$, $\hat{D}^1_{N+2}$, $\hat{D}^1_{N+3}$, and $\hat{D}^1_{N+4}$ in Figs. 3.9C, E, G, and I, respectively. Because these D_n-penetrating slits also reach and penetrate the lower edge of R, these slits are divided into two slits in $\hat{D}^1_{N+1} \cap R$, $\hat{D}^1_{N+2} \cap R$, $\hat{D}^1_{N+3} \cap R$, and $\hat{D}^1_{N+4} \cap R$ in Figs. 3.5D, F, H, and J, respectively. Therefore, the number of red D_n-penetrating slits increases one by one in $\hat{D}^1_{N+1} \to \hat{D}^1_{N+2} \to \hat{D}^1_{N+3} \to \hat{D}^1_{N+4}$ (one red slit in $\hat{D}^1_{N+1}$, two red slits in $\hat{D}^1_{N+2}$, three red slits in $\hat{D}^1_{N+3}$, and four red slits in $\hat{D}^1_{N+4}$). In addition, $\hat{D}^1_{N+4}$ has a red D_n-penetrating slit, which surrounds a yellow R-penetrating slit and penetrates the lower edge of R, as shown in Fig. 3.9I. This red slit is divided into two slits in $\hat{D}^1_{N+4} \cap R$, as shown in Fig. 3.9J. In addition, the red slits divided in $\hat{D}^1_{N+4} \cap R$ generate two D_n-penetrating slits in $\hat{D}^1_{N+5}$, each of which is also divided into two slits in $\hat{D}^1_{N+5} \cap R$. The number of red slits increases at an accelerating rate in the same way as that when there is one non-R-penetrating slit in D^1_∞. Figure 3.10 shows the formation process for the basin of attraction for $\gamma = 0.013$, where the basin boundary is fractal and there are two non-R-penetrating slits. A non-D_n-penetrating slit penetrates the lower edge of R in D_5 ($N = 5$, $D^1_5 = D_5$). A D_n-penetrating slit surrounds the R-penetrating slit in D_9 ($N + 4 = 9$, $\hat{D}^1_9 = D_9$), which penetrates the lower edge of R and is divided into two slits in $D_9 \cap R$.

Mechanism for sharp changes in basin characteristics when number of non-R-penetrating slits decreases from 2 to 1

In the comparison of the basin formation processes when one non-R-penetrating slit exists in D^1_∞ and when two exist, it is common that the number of slits in D^1_n increases at an accelerating rate to generate fractal basin boundaries. However, how the number of slits increases in the basin formation processes is different. Specifically, it takes three applications of S^{-1} to surround the R-penetrating slit by a D_n-penetrating slit and to be divided into two slits in $\hat{D}^1_n \cap R$ for one non-R-penetrating

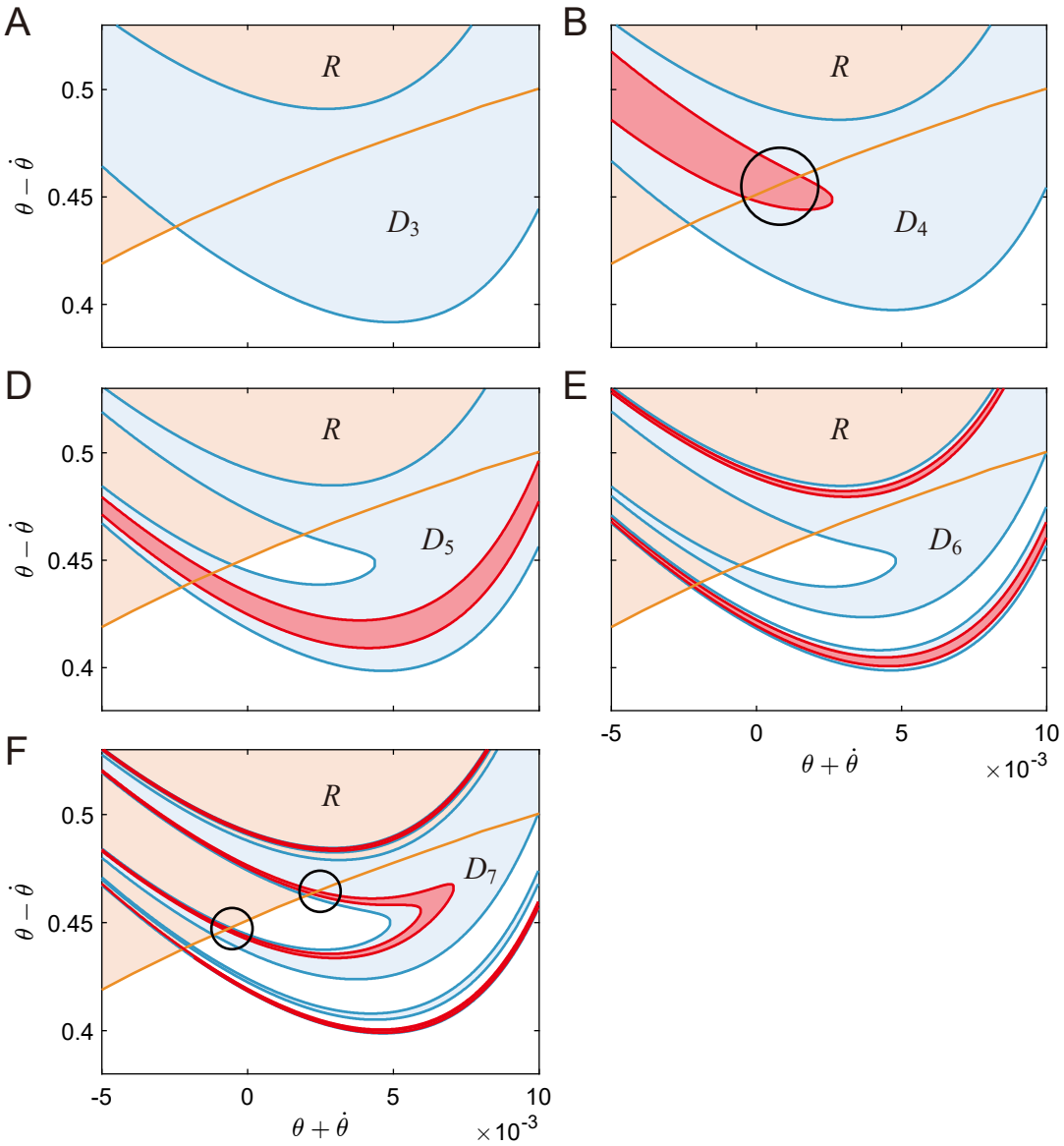

FIGURE 3.8: Formation process for basin of attraction from D_3 to D_7 (A–F) for $\gamma = 0.018$, where there is one non-R-penetrating slit in D_∞^1. The red slits correspond to those for $N = 4$ in Fig. 3.5. A non-D_n-penetrating slit penetrates the lower edge of the range of R in D_4 and a D_n-penetrating slit surrounding the R-penetrating slit penetrates R in D_7.

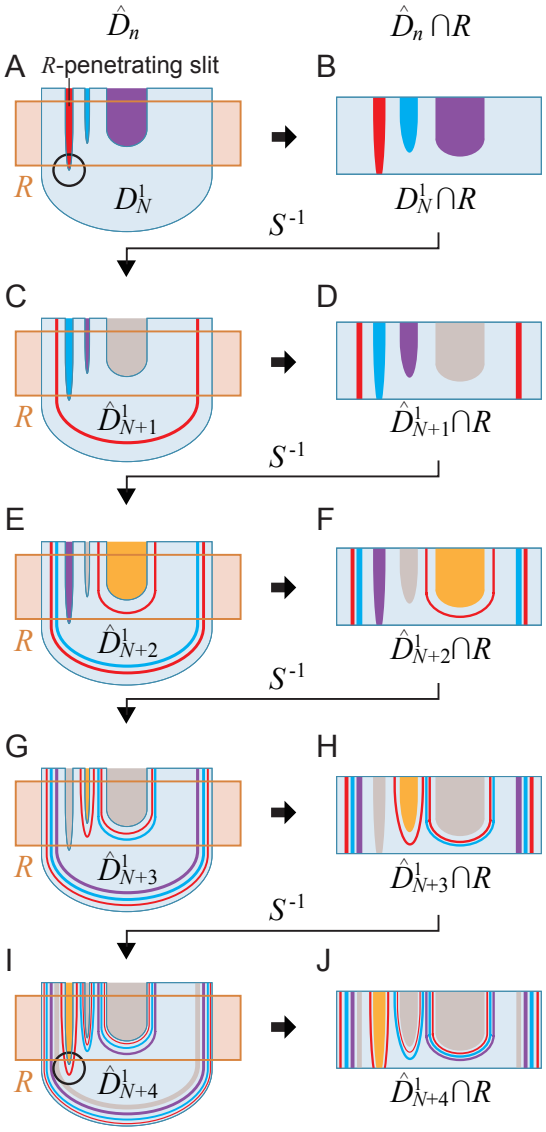

FIGURE 3.9: Formation process for fractal basin of attraction when there are two non-R-penetrating slits. When a red slit in D_N penetrates the lower edge of the range R for the first time (A), $D_N \cap R$ is separated into two regions (B). D_{N+1} has a red D_n-penetrating slit near the outer edge (C), and it is separated into two red slits in $D_{N+1} \cap R$ (D). D_{N+2} and $D_{N+2} \cap R$ have a red D_n-penetrating slit, which surrounds the center, yellow non-R-penetrating slit (E, F). D_{N+3} and $D_{N+3} \cap R$ have a red D_n-penetrating slit, which surrounds the non-R-penetrating slit at the left of the center, yellow non-R-penetrating slit (G, H). D_{N+4} has a red D_n-penetrating slit, which surrounds a yellow R-penetrating slit and penetrates the lower edge of R (I), and it is also separated into two red slits in $D_{N+4} \cap R$ (J). While it takes three applications of S^{-1} to surround the R-penetrating slit by a D_n-penetrating slit for one non-R-penetrating slit (Fig. 3.5), it takes four applications for two non-R-penetrating slits.

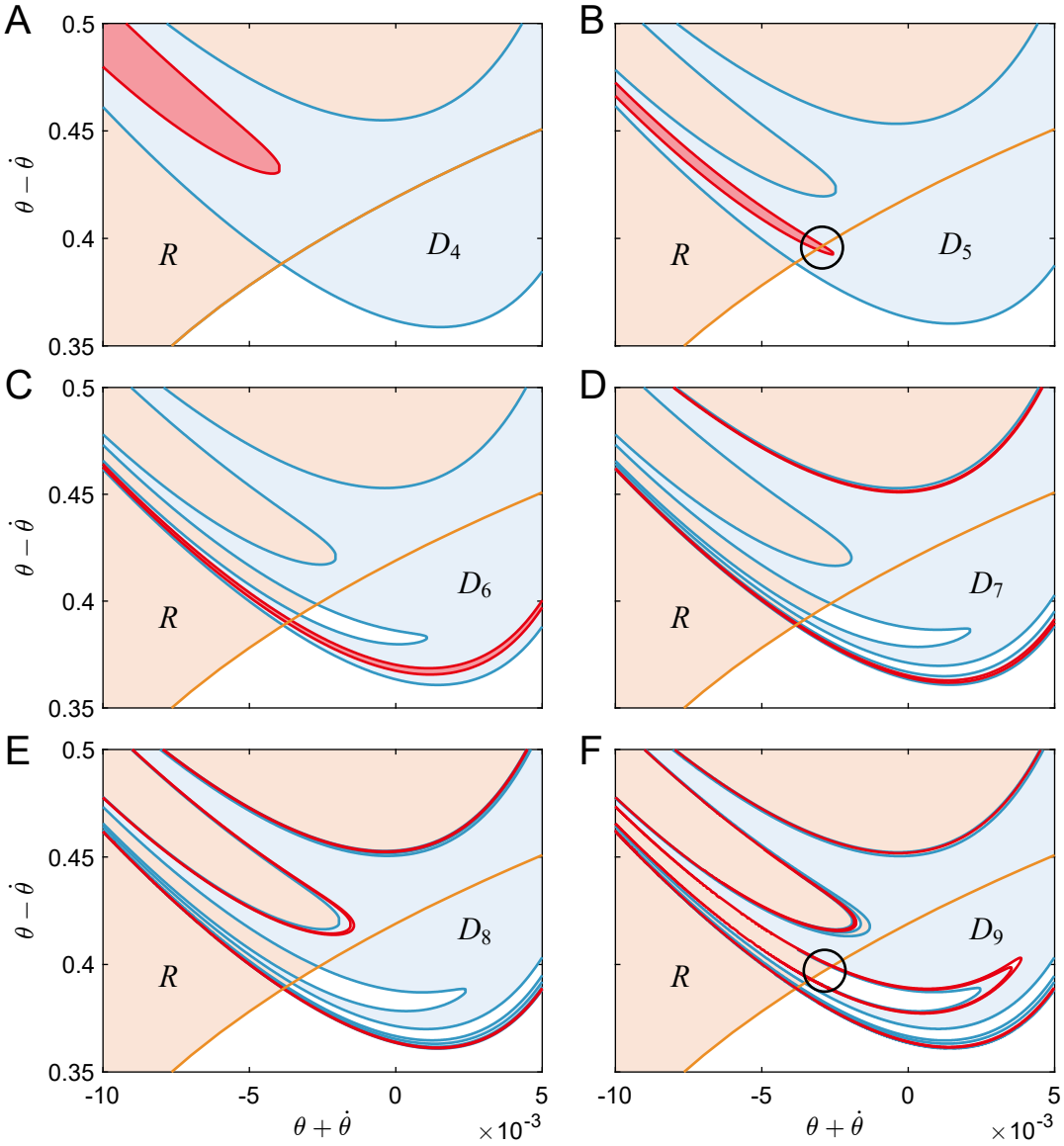

FIGURE 3.10: Formation process for basin of attraction from D_4 to D_9 (A–G) for $\gamma = 0.013$, where two non-R-penetrating slits exist in D_∞^1. The red slits correspond to those for $N = 5$ in Fig. 3.9. A non-D_n-penetrating slit penetrates the lower edge of the range of R in D_5 and a D_n-penetrating slit surrounding the R-penetrating slit penetrates R in D_9.

slit. In contrast, it takes four applications for two non-R-penetrating slits. This implies that one non-R-penetrating slit has a faster rate of increase than two non-R-penetrating slits. This difference is due to the formation process for D_n-penetrating slits. Specifically, $\hat{D}^1_{N+1}$ has a red D_n-penetrating slit near the outer edge, as shown in Figs. 3.5C and 3.9C. $\hat{D}^1_{N+2}$ also has another red D_n-penetrating slit, which surrounds the non-R-penetrating slit at the middle, as shown in Figs. 3.5E and 3.9E. For two non-R-penetrating slits, $\hat{D}^1_{N+3}$ has another red D_n-penetrating slit, which surrounds the non-R-penetrating slit left of the middle non-R-penetrating slit, as shown in Fig. 3.9G. Finally, $\hat{D}^1_{N+3}$ for one non-R-penetrating slit and $\hat{D}^1_{N+4}$ for two non-R-penetrating slits have a red D_n-penetrating slit, which surrounds a R-penetrating slit, as shown in Figs. 3.5G and 3.9I. This means that the surrounding D_n-penetrating slits appear one by one from D^1_{N+2} to D^1_{N+k+2}, where k is the number of non-R-penetrating slits. As a result, one non-R-penetrating slit forms a larger number of slits and more complex boundaries in D_n for any n than two non-R-penetrating slits, which leads to a smaller basin size and a lower uncertainty exponent for basin boundaries. This mechanism induces the sharp changes in the basin characteristics at $\gamma \approx 0.0135$, where the number of non-R-penetrating slits decreases from 2 to 1.

Mechanism for sharp changes in basin characteristics when number of non-R-penetrating slits decreases from $k+1$ to k

The mechanism for the sharp change in the basin characteristics described in the previous section is applicable when the number of non-R-penetrating slits decreases from $k+1$ to k ($k = 1, 2, \dots$). Suppose that there are $(k+1)$ non-R-penetrating slits. When $\hat{D}^1_N$ has an R-penetrating slit, $\hat{D}^1_{N+1}$ has a D_n-penetrating slit near the outer edge in the same way for one and two non-R-penetrating slits in Figs. 3.5C and 3.9C, respectively. $\hat{D}^1_{N+2}$ has a D_n-penetrating slit, which surrounds the center non-R-penetrating slit. $\hat{D}^1_{N+n}$ ($3 \leq n \leq k+2$) has a D_n-penetrating slit, which surrounds the non-R-penetrating slit at the $(n-2)$th slit left from the center non-R-penetrating slit. Finally, $\hat{D}^1_{N+k+3}$ has a D_n-penetrating slit that surrounds an R-penetrating slit. This means that it takes $k+3$ applications of S^{-1} to generate the D_n-penetrating slit that surrounds the R-penetrating slit. Therefore, when the number of non-R-penetrating slits decreases from $k+1$ to k, the number of iterations changes from $k+3$ to $k+2$. The rate of this change is $\frac{k+2}{k+3}$, which is $\frac{3}{4}$ for $k = 1$ for $\gamma \approx 0.0135$ and $\frac{4}{5}$ for $k = 2$ at $\gamma \approx 0.0105$. It is almost 1 for $k \gg 1$ for $0.0075 < \gamma < 0.01$. Therefore, the change in the basin of attraction is most remarkable for $\gamma \approx 0.0135$ with $k = 1$, and is less significant for smaller γ with larger k, as shown in Figs. 3.3C and D. In particular, the changes for $0.0075 < \gamma < 0.01$ are difficult to recognize.

3.4.4 Mechanism for disappearance of basin of attraction

The mechanism for the sharp changes in the basin characteristics described in the previous section is applicable when the number of non-R-penetrating slits decreases from $k+1$ to k for $k = 1, 2, \ldots$. In this section, we investigate the formation process for the basin of attraction when the number of non-R-penetrating slits decreases from 1 to 0 and all non-D_n-penetrating slits penetrate the lower edge of R.

Figure 3.11 explains the basin formation process when all non-D_n-penetrating slits penetrate the lower edge of R. Suppose that all non-D_n-penetrating slits penetrate R at $n = N$ in D_N^1 (Fig. 3.11A). Then, a D_n-penetrating slit is generated in $\hat{D}_{N+1}^1$, which penetrates the lower edge of R (Fig. 3.11C) and is divided into two slits in $\hat{D}_{N+1}^1 \cap R$ (Fig. 3.11D). Moreover, each divided slit also penetrates the lower edge of R in $\hat{D}_{N+2}^1$ (Fig. 3.11E) and is divided into two slits in $\hat{D}_{N+2}^1 \cap R$ (Fig. 3.11F). Each application of S^{-1} produces this penetration of R and subsequent division into two slits. This formation process for the basin of attraction can be assumed as a one-dimensional Cantor set [117]. Therefore, the area of $\hat{D}_n^1$ decreases as n increases and it finally disappears. That is, the basin of attraction disappears when the number of non-R-penetrating slits decreases from 1 to 0. However, note that we cannot observe that the number of non-R-penetrating slits is 0 as in Fig. 3.3E. This is because we cannot calculate the number of non-R-penetrating slits when the basin of attraction disappears. (Actually, D_n^1 does not exist when all non-D_n-penetrating slits penetrate R because there is neither an attractor nor a basin of attraction. However, we used it only in the basin formation process to simply explain the disappearance mechanism for the basin of attraction.)

Figure 3.12 shows the disappearance process for the basin of attraction for $\gamma = 0.021$, where all non-D_n-penetrating slits penetrate the lower edge of R. A non-D_n-penetrating slit penetrates R in D_6^1 ($N = 6$) and non-R-penetrating slits disappear in Fig. 3.12B. As a result, D_7 has one red D_n-penetrating slit (Fig. 3.12C), as shown in Fig. 3.11C. Furthermore, D_8 and D_9 have two and four red D_n-penetrating slits (Figs. 3.12D and E), respectively. D_n becomes thinner as n increases. By repeating these processes, the basin of attraction disappears.

3.5 Discussion

In this study, we showed that sharp changes in the size and fractality of the basin of attraction for passive dynamic walking depends on the slope angle γ. In addition, we clarified the mechanism for the sharp changes based on the formation process by improving our previous analysis. We also proposed a mechanism for the disappearance of the basin of attraction, which was previously explained by a boundary crisis [47,94], based on the formation process for the basin of attraction. These mechanisms are commonly based on the stretching-bending deformation caused by the

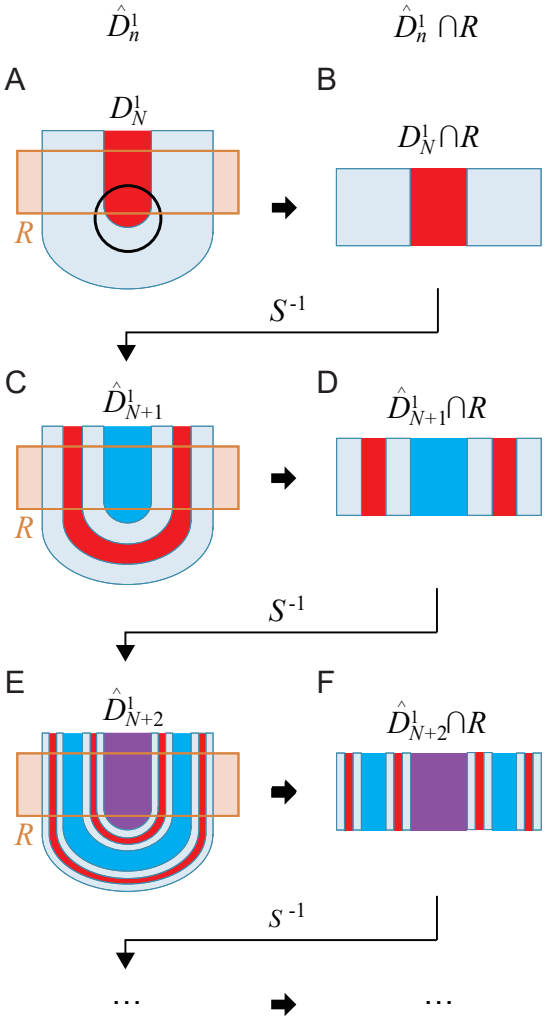

FIGURE 3.11: Formation process for basin of attraction when all non-D_n-penetrating slits penetrate lower edge of range R. When the last non-R-penetrating slit penetrates R at $n = N$ (A), $D_N^1 \cap R$ has one red slit (B). $\hat{D}_{N+1}^1$ has one red D_n-penetrating slit inside the U-shaped region (C). $\hat{D}_{N+1}^1 \cap R$ has two red slits (D). $\hat{D}_{N+2}^1$ has two red D_n-penetrating slits inside the U-shaped region (E). $\hat{D}_{N+2}^1 \cap R$ has four red slits (D). $\hat{D}_n^1 \cap R$ ($n = N, N+1, \dots$) can be assumed as a one-dimensional Cantor set.

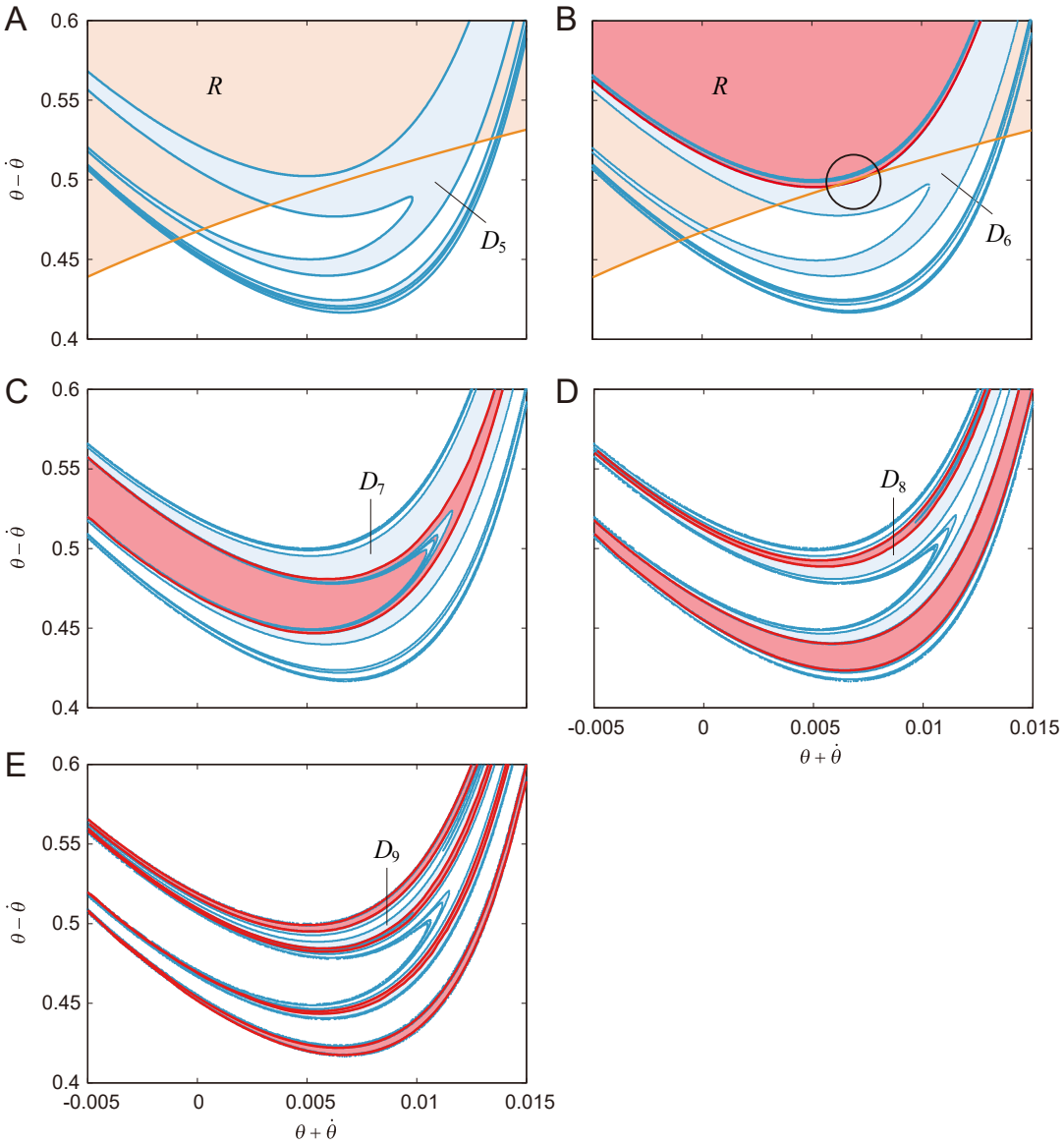

FIGURE 3.12: Formation process for basin of attraction from D_5 to D_9 (A–E) for $\gamma = 0.021$, where all non-D_n-penetrating slits penetrate lower edge of range R. The red slits correspond to the red slits for $N = 6$ in Fig. 3.11. D_7 has one red D_n-penetrating slit inside the U-shaped region. D_8 and D_9 have two and four red D_n-penetrating slits, respectively.

inverse image of the Poincaré map. Specifically, abrupt alterations of the overlap between region D_n and the range R of the Poincaré map in the formation process for the basin of attraction induce these sharp changes in the basin of attraction.

We used a computational resolution that allowed us to identify sharp changes in fractal dimension at $\gamma = 0.0103$, 0.0135, and 0.019. However, even at higher resolution, two technical difficulties prevented us from finding sharp changes for $0.0075 < \gamma < 0.01$. The first difficulty is the regional dependence of the fractal dimension, since different parts of the basin of attraction have different fractal dimensions. In addition, the basin of attraction moves in phase space depending on γ. Because we cannot necessarily calculate the fractal dimension in the same region of the basin boundary for each γ, this region-dependent effect is a serious problem. The second difficulty is the accuracy of the calculation for the basin of attraction. To determine if an initial state is inside or outside the basin of attraction, we determined whether or not the model fell within 50 steps, as described in Sect. 3.3.1. Near the fractal basin boundary, it takes an extremely long time for the model to fall, which affects the fractality of the basin boundary.

Our model is a hybrid system. The boundaries of the domain and the range of the Poincaré map for our model are mainly obtained from touchdown conditions (Eqs. (3.4) and (3.5), respectively), as previously described [94,97]. Because the basin boundary is obtained from the inverse image of the Poincaré map of these boundaries, it can be considered to have the same properties as the boundaries for the domain and the range. Therefore, the basin boundary in our model is dominated by the touchdown conditions and does not correspond to a stable manifold as in continuous systems. In future studies, we intend to investigate the relationship between manifolds and basin boundaries.

Sharp changes in the basin of attraction are also observed in the Hénon map, which is a well-studied example of a nonlinear dynamical system exhibiting chaotic attractors [42]. Because the inverse image of the Hénon map also induces a stretching-bending effect, a common mechanism is expected for the sharp changes in the basin of attraction between passive dynamic walking and the Hénon map. However, sharp changes occur countless times during passive dynamic walking, whereas they occur only twice in the Hénon map [42]. Furthermore, the Poincaré map for passive dynamic walking is neither surjective nor injective because the system is a hybrid system, whereas the Hénon map is bijective. Therefore, different mechanisms are expected for the Hénon map. Clarifying common and specific features of the basin of attraction for dynamical systems is a subject for future study.

To understand the stabilization mechanism for bipedal walking, not only the simplest walking model used in this study, but also more general models with knees and an upper body have been considered [18,21,35]. To carry out a stability analysis of these models, a method for designing an explicit expression for the Poincaré map

has been proposed [134–136]. The disappearance of attractors in these models is not solely attributed to the boundary crisis, but also to other bifurcations, such as flip bifurcation and saddle-node bifurcation [21, 45, 46]. However, the basin characteristics for these models remain largely unclear. The principal dynamic characteristic of bipedal walking is saddle instability due to the inverted pendulum, which induces the stretching-bending effect in the inverse image of the Poincaré map [94]. Therefore, the formation process for the basin of attraction clarified in this study is expected to be applicable to the formation mechanisms for the basin of attraction of other models, and for clarifying their basin characteristics.

Chapter 4

Mechanism of changes in temporal fractal in stride intervals in simple neuromechanical model

4.1 Introduction

Human walking is not perfectly periodic. The stride interval fluctuates from one stride to the next, exhibiting statistical persistence [22, 54, 125, 126], which indicates that deviations in a time series are statistically more likely to be followed by subsequent deviations in the same direction. Although the stride interval fluctuations change depending on the gait speed and during development from childhood to adulthood, the statistical persistence remains unchanged [55, 56]. However, the stride interval fluctuations for elderly subjects [53] and patients with Huntington's disease [53] or Parkinson's disease [30] become uncorrelated. Experimental interventions for walking, such as the use of a metronome, also make the stride interval fluctuations uncorrelated [55]. It is largely unclear why statistical persistence appears in stride intervals in human walking and why this statistical property is changed by aging, neural disorders, and experimental interventions.

It has been hypothesized that the central nervous system has an underlying persistence and is responsible for the statistical persistence in stride intervals. This is supported by the finding that statistical persistence remains in patients with significant peripheral nerve degeneration [37]. Various neural system models have been developed to reproduce the statistical persistence and investigate the associated mechanisms. [54] developed a model of the central pattern generators (CPGs) in the spinal cord and introduced "memory" into the CPG model by allowing transitions from frequency to frequency. [10] extended this model by introducing a random walk for the signal transmission of neural circuits. [127] developed a "Super CPG" model that introduces external interventions via a forced van der Pol oscillator.

Human walking is a complex phenomenon generated through dynamic interactions between the central nervous system and the biomechanical system. It has also been hypothesized that the statistical persistence in stride intervals emerges through

complex interactions during walking. [31] integrated a biomechanical model composed of seven rigid links with a CPG model, which incorporated a phase resetting mechanism as sensory feedback as well as feedforward, trajectory tracking, and intermittent feedback controllers, to reproduce statistical persistence. They showed that a lack of phase resetting induces a loss of statistical persistence. However, it is difficult to fully understand the essential mechanisms responsible for generating and changing this statistical property because of the complexity of the neural and biomechanical models.

In human walking, the stance leg, which is almost straight, rotates around the foot contact point like an inverted pendulum. To investigate the essential mechanisms responsible for generating human walking from a dynamic viewpoint, simple compass-type mechanical models have been used [12, 23, 71, 73, 97]. [38] and [1] reproduced the statistical persistence in stride intervals using simple compass-type models with sensory feedback controllers. However, they did not investigate the contribution of the feedback controllers to changes in the statistical persistence; thus, the essential mechanisms remain unclear.

The aim of this study is to clarify the contribution of phase resetting to the generation and change in the statistical persistence using a simple model. Specifically, we used a simplified neuromechanical model composed of a simple compass-type biomechanical model and a simple CPG model that incorporates phase resetting and a feedforward controller. Our model reproduced the statistical persistence in stride intervals. A lack of phase resetting induced a loss of statistical persistence, as observed in [31]. Furthermore, we clarified the mechanisms responsible for changes in this statistical property caused by phase resetting based on the phase response characteristics. Our findings provide important insights into the mechanisms underlying the generation and change of the statistical persistence in the stride intervals in human walking.

4.2 Methods

4.2.1 Mechanical model

We used a simple compass-type model (Fig. 4.1). This model has two legs (swing and stance legs), the lengths of which are both l, connected by a frictionless hip joint. The masses are located at the hip and on the legs at a distance b from the hip joint; M is the hip mass and m is the leg mass. θ_1 is the angle of the stance leg with respect to the vertical, and θ_2 is the relative angle between the stance and swing legs. The tip of the stance leg, which corresponds to the ankle, is fixed on the ground. The stance leg rotates freely without friction. This model walks on level ground via joint torques u_1 (at the ankle) and u_2 (at the hip). g is the acceleration due to gravity.

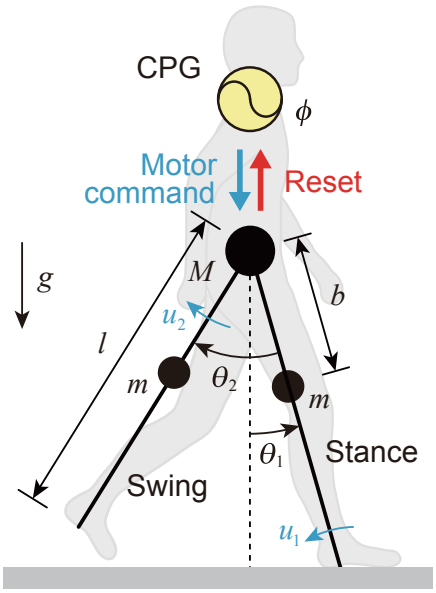

FIGURE 4.1: Neuromechanical model of human walking composed of CPG model with phase resetting and compass-type biomechanical model.

We used the following model parameters based on [129]: $M = 50$ kg, $m = 11$ kg, $l = 1$ m, $b = 0.4$ m, and $g = 9.8$ m/s^2.

When the tip of the swing leg is in the air, the equations of motion for our model are

$$\begin{bmatrix} Ml^2 + m\{l^2 + (l-b)^2\} - 2mlb\cos\theta_2 + mb^2 & mlb\cos\theta_2 - mb^2 \\ mlb\cos\theta_2 - mb^2 & mb^2 \end{bmatrix} \begin{bmatrix} \ddot{\theta}_1 \\ \ddot{\theta}_2 \end{bmatrix} + \begin{bmatrix} -mlb(\dot{\theta}_2 - 2\dot{\theta}_1)\dot{\theta}_2 \sin\theta_2 \\ -mlb\dot{\theta}_1^2 \sin\theta_2 \end{bmatrix} + \begin{bmatrix} -\{gm(2l-b) + gMl\}\sin\theta_1 - gmb\sin(\theta_2 - \theta_1) \\ gmb\sin(\theta_2 - \theta_1) \end{bmatrix} = \begin{bmatrix} u_1 \\ u_2 \end{bmatrix} \tag{4.1}$$

The tip of the swing leg touches the ground (touchdown) when the following conditions are satisfied:

$$2\theta_1 - \theta_2 = 0 \tag{4.2}$$

$$\theta_1 < 0 \tag{4.3}$$

$$2\dot{\theta}_1 - \dot{\theta}_2 < 0 \tag{4.4}$$

We used condition (4.3) so that touchdown occurs only in front of the model to move forward, and condition (4.4) to ignore the scuffing of the leg tip on the ground when the swing leg is swung forward. We assumed that touchdown is a fully inelastic collision (no slip, no bounce) and that the stance leg lifts off the ground just after touchdown. Because the roles of the swing and stance legs are reversed just after

touchdown, we obtain

$$\theta_1^+ = -\theta_1^- \tag{4.5}$$
$$\theta_2^+ = -\theta_2^- \tag{4.6}$$

where $*^-$ and $*^+$ are the state $*$ just before and after touchdown, respectively. Due to this collision, the angular velocities discontinuously change. We assumed that when the stance leg leaves the ground, it does not interact with the ground and the work of the joint torques can be neglected. These assumptions yield

$$\begin{bmatrix} \dot{\theta}_1^+ \\ \dot{\theta}_2^+ \end{bmatrix} = \{Q^+(\theta_1^-)\}^{-1} Q^-(\theta_1^-) \begin{bmatrix} \dot{\theta}_1^- \\ \dot{\theta}_2^- \end{bmatrix} \tag{4.7}$$

where

$$Q^+(\theta_1^-) = \begin{bmatrix} -Ml^2 - 2m(l-b)^2 - 2mlb(1-\cos 2\theta_1^-) & mb(b - l\cos 2\theta_1^-) \\ -ml(b - l\cos 2\theta_1^-) & mlb \end{bmatrix}$$
$$Q^-(\theta_1^-) = \begin{bmatrix} 2m(l-b)(b - l\cos 2\theta_1^-) - Ml^2\cos 2\theta_1^- & -m(l-b)b \\ ml(l-b) & 0 \end{bmatrix}$$

4.2.2 CPG model

The CPGs in the spinal cord are largely responsible for rhythmic leg movements, such as during locomotion [43, 98, 113]. They can produce oscillatory behavior even in the absence of rhythmic input and sensory feedback. However, sensory feedback is crucial for producing adaptive locomotor behavior. To investigate the contribution of CPGs to adaptive locomotion in humans, various oscillator models, such as the van der Pol oscillator [24, 127], Matsuoka oscillator [52, 69, 81, 95, 120, 121], and phase oscillator [3–5, 26, 31, 99, 122, 133], have been developed.

In this study, we used a phase oscillator, whose phase is ϕ $(0 \leq \phi < 2\pi)$, to generate the motor commands for our model. The oscillator phase follows the dynamics expressed by

$$\dot{\phi} = \omega \tag{4.8}$$

where ω is the basic frequency. We determined the joint torques u_1 and u_2 as

$$u_1 = A_1 \cos\phi + \sigma_1 \tag{4.9}$$
$$u_2 = A_2 \cos(\phi + \Delta) + \sigma_2 \tag{4.10}$$

where A_1 and A_2 are the amplitudes, σ_1 and σ_2 are noise terms, and Δ is the phase difference between u_1 and u_2.

It has been reported that locomotion rhythm and phase are regulated by the production of a phase shift and rhythm resetting (phase resetting) for periodic motor commands in response to sensory feedback [75, 108]. Cutaneous feedback has been observed to contribute to phase shift and rhythm resetting behavior [25, 111]. Phase

resetting has thus been modeled so that the oscillator phase is reset based on foot contact information [3, 5, 31, 122, 133]. In this study, we used the following relationship at touchdown:

$$\phi^+ = \phi_0 \tag{4.11}$$

where ϕ_0 is a constant. When phase resetting is not applied, ϕ is not regulated at touchdown. However, because the roles of the swing and stance legs are reversed just after touchdown so that $\theta_i^+ = -\theta_i^-$ $(i = 1, 2)$, we used the following relationship at touchdown:

$$\phi^+ = \phi^- - \pi \tag{4.12}$$

so that $u_i^+ = -u_i^-$ $(i = 1, 2)$ when the noise terms σ_1 and σ_2 are neglected. We designated ϕ_0 as the value to which ϕ^+ converged during steady walking (limit cycle) for the model without phase resetting and noise. Therefore, steady walking is identical between the models with and without phase resetting in the absence of noise. This allows us to clearly investigate the difference in the response to torque noise between cases with and without phase resetting.

This CPG model has four parameters, namely ω, A_1, A_2, and Δ. We used $\omega = 4.8$ rad/s based on [55]. Without noise ($\sigma_1 = \sigma_2 = 0$), we first investigated the dependence of gait speed during steady walking on A_1, A_2, and Δ, and then calculated the energy cost $\varepsilon = \int (u_1^2 + u_2^2) dt$ for one step cycle for A_1, A_2, and Δ. We determined the parameter set (A_1, A_2, Δ) required to minimize ε for each gait speed. When phase resetting was used, we determined ϕ_0 for each gait speed using the obtained parameter set.

4.2.3 Torque noise

To simulate the stochastic fluctuation of the gait, we used two independent series of white Gaussian noise for torque noise terms σ_1 and σ_2 in (4.9) and (4.10), respectively, as follows:

$$\sigma_i = \xi U_i \qquad i = 1, 2 \tag{4.13}$$

where ξ is the amplitude of the noise, and U_1 and U_2 are independent white Gaussian noise with standard deviation 1. This torque noise never induces consecutive touchdowns at extremely short intervals because of discontinuous and large changes in the state variables (4.5)–(4.7) at touchdown. We numerically solved the governing equations using the Euler-Maruyama method [57] with a time step of 10^{-5} s.

To be consistent with previous experiments on humans [53–55], a stride was defined as two consecutive steps. Stride intervals were calculated based on the time difference between every other touchdown (strides did not overlap). Each simulation trial required the model to walk 1300 steps (650 strides). The first 150 strides were omitted from the analysis to remove transient behavior due to initial conditions.

4.2.4 Detrended fluctuation analysis

We used detrended fluctuation analysis (DFA) to determine the statistical persistence in the time series of stride intervals for each trial of the computer simulation. This method decreases the effect of noise and removes local trends, making it less affected by non-stationarities. The details of the method can be found elsewhere [51, 54, 62, 101–103]. Briefly, the feature amount $F(n)$ constructed from segments of length n of the time series exhibits a power-law relationship, indicating the presence of scaling as $F(n) \sim n^{\alpha}$. We investigate the scaling exponent α to determine the statistical persistence for the time series data.

In this study, we first formed the following accumulated sum using the sequence of stride intervals $x(i)$ for $i = 1, 2, \ldots, N$, where N is the total number of strides ($N = 500$):

$$y(i) = \sum_{k=1}^{i} [x(k) - \bar{x}] \qquad i = 1, 2, \ldots, N \tag{4.14}$$

where $\bar{x}$ is the mean stride interval from $x(1)$ to $x(N)$. We then divided the integrated series $y(i)$ into segments of length n ($n < N$), $y_j(s)$ ($j = 1, 2, \ldots, N/n, s = 1, 2, \ldots, n$), so that each segment is equal in length and non-overlapping. We next detrended each segment $y_j(s)$ by subtracting a least squares linear regression line $\hat{y}_j(s)$ fit to $y_j(s)$, and averaged the squares of the detrended data (i.e., the residuals). We thus obtained the standard deviation $F(n)$ as

$$F(n) = \sqrt{\frac{1}{n} \sum_{s=1}^{n} \left[y_j(s) - \hat{y}_j(s) \right]^2} \tag{4.15}$$

We used a set of n distributed equally on a logarithmic scale between 4 and $N/4$ [68], specifically, $n = 4, 5, 6, ..., 87, 104$, and 125 (sample size is 20).

In general, $F(n)$ increases with increasing n and a graph of $\log F(n)$ versus $\log n$ exhibits a power-law relationship, indicating the presence of scaling as $F(n) \sim n^{\alpha}$. We fit $\log F(n)$ versus $\log n$ plots with a linear function using a standard least squares regression approach, and obtained the scaling exponent α from the slope of this line. In particular, $\alpha = 0.5$ indicates that the stride intervals are completely uncorrelated (i.e., white noise). That is, DFA will still produce $\alpha = 0.5$ even if the time series is rearranged in any manner (through surrogate data analysis). In contrast, $\alpha < 0.5$ indicates statistical anti-persistence in stride intervals and $0.5 < \alpha \leq 1.0$ indicates statistical persistence. When $\alpha > 1.0$, the time series is brown noise (i.e., integrated white noise) [54].

4.3 Results

4.3.1 Determination of parameters for each gait speed

Without noise ($\xi = 0$), our model achieved stable walking with a gait speed v of 0.25 to 0.6 m/s depending on the parameters A_1, A_2, and Δ. Figure 4.2A shows the contour of the evaluation criterion ε for A_1, A_2, and Δ, which generated $v = 0.3$, 0.4, and 0.5 m/s. Figure 4.2B shows the parameter sets (A_1, A_2, Δ), each of which minimized ε for a given gait speed v. The use of phase resetting did not affect these results. We use the parameter set $A_1 = A_1(v)$, $A_2 = A_2(v)$, and $\Delta = \Delta(v)$ in the following sections.

4.3.2 Stride interval fluctuations

Figure 4.3 compares the simulation results between the models with and without phase resetting at a walking speed of 0.4 m/s ($A_1 = 4.9, A_2 = 10, \Delta = 0.47$) using the noise amplitude $\xi = 1$. Figures 4.3A and B show the angles θ_1 and θ_2 and the stride intervals, respectively, during 500 strides. Although ξ is identical between the models, the model without phase resetting has larger stride interval fluctuations than those for the model with phase resetting. Figure 4.3C shows a plot of $\log F(n)$ for $\log n$ and the scaling exponent α obtained from the slope of the fitted line. The model with phase resetting exhibits statistical persistence in stride intervals ($0.5 < \alpha \leq 1.0$), which is consistent with observations of healthy adults [54]. Furthermore, the standard deviation of stride interval fluctuations of the model with phase resetting is 0.03, which is also consistent with observations of healthy adults [54]. In contrast, the model without phase resetting exhibits statistical anti-persistence in stride intervals ($\alpha < 0.5$). Figure 4.4 shows the dependence of α on ξ. The models with and without phase resetting, both of which kept walking when $\xi \leq 1$, exhibited statistical persistence and anti-persistence, respectively, regardless of ξ.

Figure 4.5 compares the simulation results for the models with and without phase resetting for various values of gait speed v using $\xi = 10^{-2}$. Figures 4.5A and B show the stride intervals and $\log F(n)$ plot, respectively, for $v = 0.3$ m/s ($A_1 = 1.3, A_2 = 6.1, \Delta = 0.57$), 0.4 m/s ($A_1 = 4.9, A_2 = 10, \Delta = 0.47$), and 0.5 m/s ($A_1 = 14, A_2 = 15, \Delta = 0.37$). Figure 4.5C shows the dependence of α on v. The model with phase resetting exhibits statistical persistence regardless of v, which is consistent with observations of healthy adults [55]. In contrast, the model without phase resetting exhibits statistical anti-persistence regardless of v.

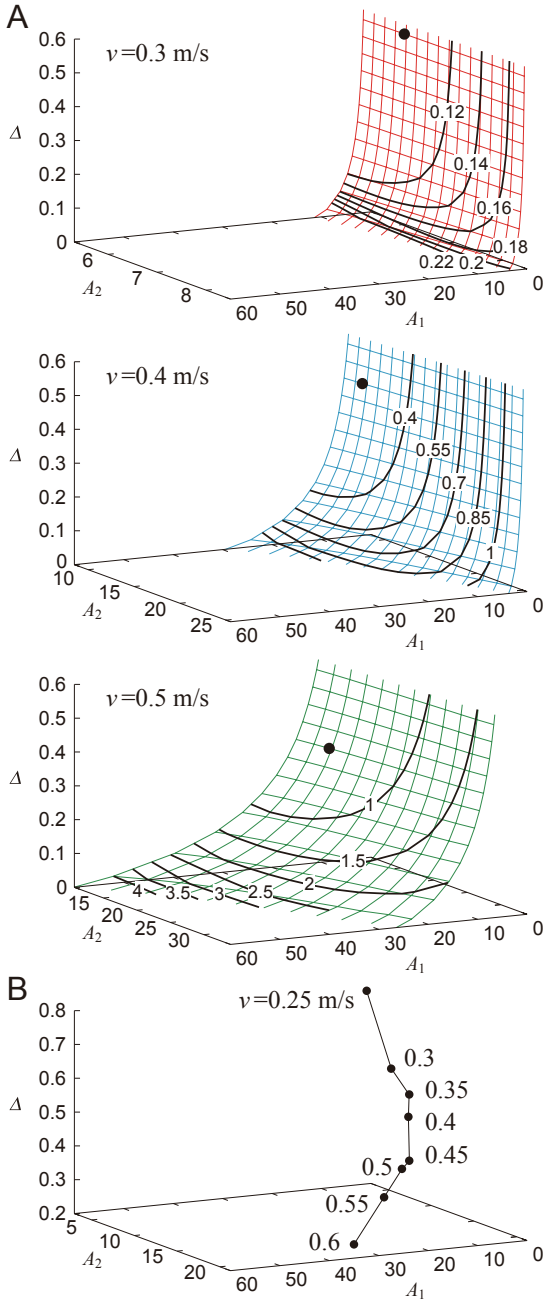

FIGURE 4.2: Dependence of gait performance on parameters A_1, A_2, and Δ without noise. A. Contour of evaluation criterion ε for parameters that generate gait speed $v = 0.3$, 0.4, and 0.5 m/s. Data point indicates the parameter set that minimizes ε. B. Parameter sets that minimize ε for each gait speed v.

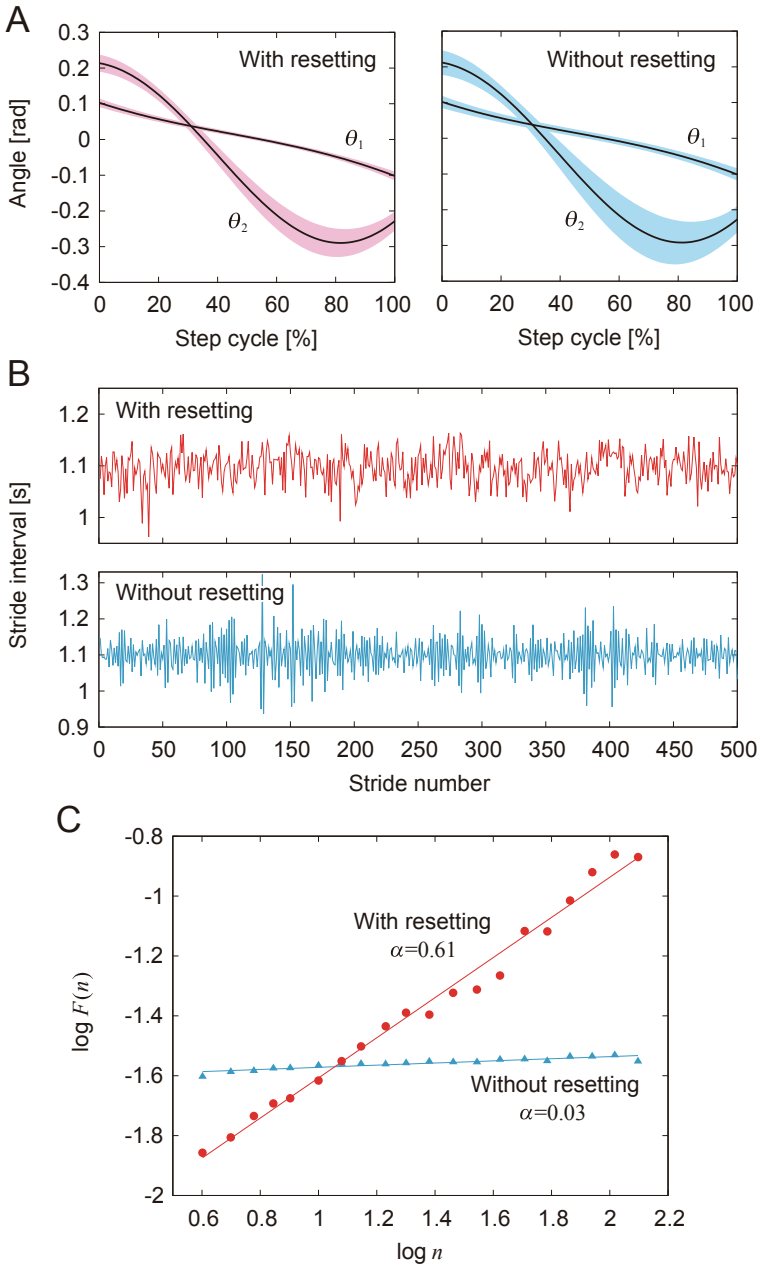

FIGURE 4.3: Comparison of gait fluctuations between models with and without phase resetting at gait speed $v = 0.4$ m/s using noise amplitude $\xi = 1$ (see Supplementary Movie). A. Angles θ_1 and θ_2. Black lines and colored areas indicate the average and standard deviation, respectively. B. Stride intervals. C. Plot of $\log F(n)$ for $\log n$ and scaling exponent α obtained from slope of fitted line.

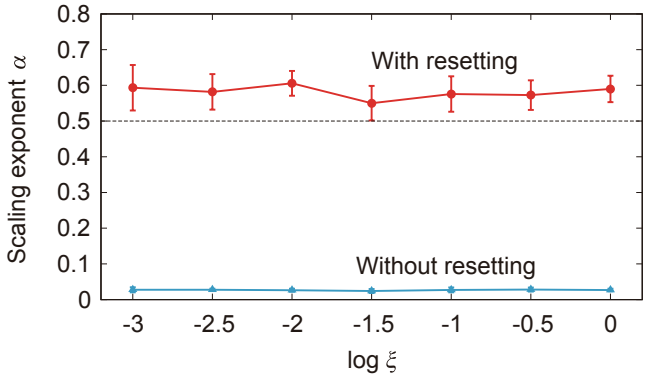

FIGURE 4.4: Comparison of scaling exponent α for noise amplitude ξ between models with and without phase resetting at gait speed $v = 0.4$ m/s. Data points and error bars correspond to the means and standard deviations, respectively, of the results of ten simulations.

4.4 Discussion

4.4.1 Mechanisms for statistical persistence and anti-persistence of stride intervals

In this study, the model with phase resetting exhibited statistical persistence in stride intervals ($0.5 < \alpha \leq 1.0$), whereas the model without phase resetting exhibited statistical anti-persistence ($\alpha < 0.5$) (Fig. 4.3), as observed in a previous modeling study [31]. Statistical anti-persistence is characterized by the alternation of large and small values. [31] performed a linearized stability analysis on a model without phase resetting and noise, and showed that the dominant mode (least stable mode) characterized by Floquet multipliers was a pair of complex conjugates whose amplitude was less than but close to unity and whose argument was greater than $\pi/2$. This suggests that the fluctuation ξ_n of the stride number n can be approximately written as $\xi_n = (-r)^n \xi_1$, where $r \sim 1$ $(r < 1)$ and ξ_1 is an initial deviation, corresponding to a slowly damped period-2 oscillation. They explained that this period-2 oscillation induced the alternation of long and short stride intervals and statistical anti-persistence. Although we performed the same stability analysis for our model, the dominant mode of our model without phase resetting and noise was positive real, whose amplitude is less than 1, indicating that the initial deviation monotonically decreases. In addition, our model with phase resetting had almost the same dominant mode as that for our model without phase resetting and it is difficult to conclude that these stability characteristics explain the difference in the statistical properties in stride intervals between the models with and without phase resetting. Furthermore, the amplitude of our dominant mode was 0.65 and the damping was relatively fast.

Next, we directly consider the difference in the response of the stride interval to disturbances. Specifically, we focus on the phase response curve in phase reduction theory [74, 128], which explains how the phase of a limit cycle oscillator shifts

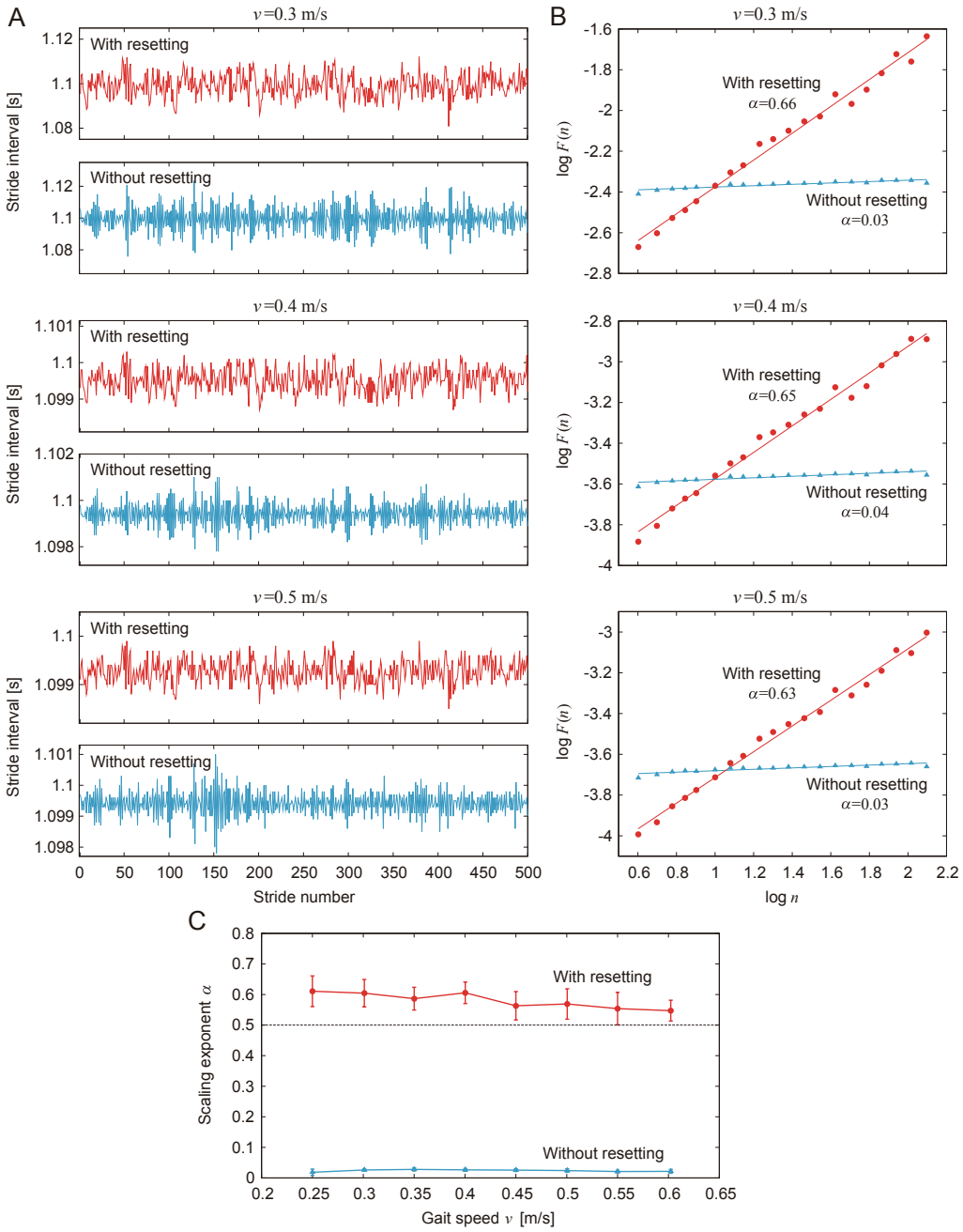

FIGURE 4.5: Comparison of stride interval fluctuations for various values of gait speed v between models with and without phase resetting using noise amplitude $\xi = 10^{-2}$. A. Stride intervals and B. plot of $\log F(n)$ for $\log n$ for gait speed $v = 0.3$, 0.4, and 0.5 m/s. C. Scaling exponent α versus gait speed v. Data points and error bars correspond to the means and standard deviations, respectively, of the results of ten simulations.

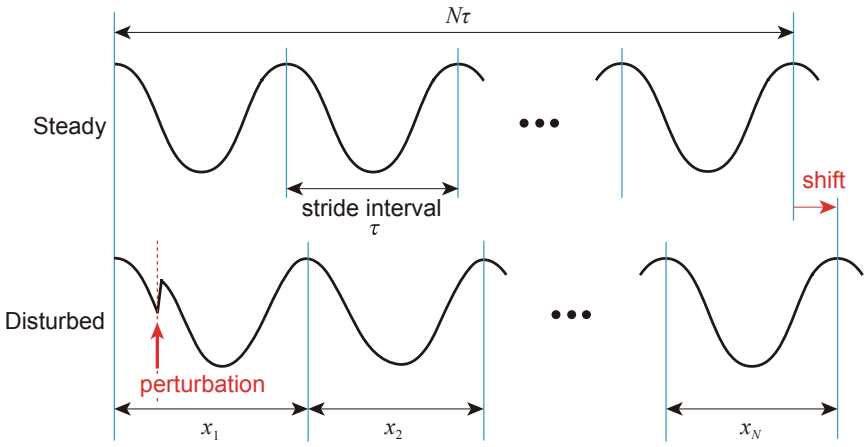

FIGURE 4.6: Phase shift caused by disturbance to limit cycle of walking. After recovery, locomotion phase is shifted ($x_1 + \cdots + x_N > N\tau$).

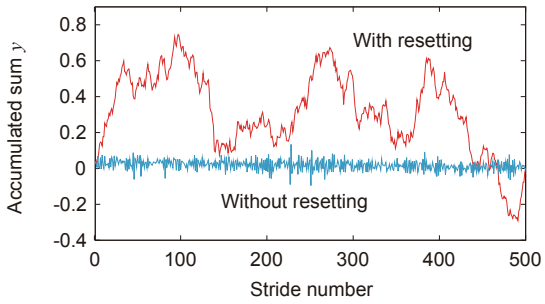

FIGURE 4.7: Comparison of accumulated sum y of stride intervals between models with and without phase resetting at gait speed $v = 0.4$ m/s and using noise amplitude $\xi = 1$ in Fig. 4.3.

by a perturbation at an arbitrary phase (Fig. 4.6). The model with phase resetting shows a shift of the locomotion phase after the recovery due to phase resetting in (4.11) at foot contact, whereas the model without phase resetting shows no phase shift [122]. Furthermore, the phase shift for the model with phase resetting varies depending on the timing of the disturbance. Therefore, the accumulated sum y of stride intervals in (4.14) tends to move to the cumulative sum of the amount of phase shifts induced by input noise in the model with phase resetting, which results in a relatively smooth signal with large low-frequency components, as shown in Fig. 4.7. In contrast, y tends to converge to 0 in the model without phase resetting, which results in a rough signal with large high-frequency components. Because the scaling exponent α increases with the degree of smoothness [27], this difference induces the difference in the scaling exponent α and statistical properties between the models with and without phase resetting.

4.4.2 Biological relevance of our findings

The scaling exponent α greatly decreases during walking to a metronome in humans [55], where the stride interval is constrained by an external cadence (i.e., metronome). This corresponds to the walking of the model without phase resetting,

where the stride interval is constrained by the frequency ω in (4.8) of the phase oscillator. Therefore, the locomotion phase remains almost unchanged during walking to a metronome, and α decreases as in the model without phase resetting (Fig. 4.3), as discussed in Section 4.4.1. It has been reported that α also greatly decreases for the stride interval fluctuations of elderly subjects [53] and patients with Huntington's disease [53] or Parkinson's disease [30]. Although the phase response characteristics have been clarified during walking for healthy adults [34, 92, 133], those during walking for elderly subjects and patients with neural disorders remain unclear. Investigating them would help clarify the mechanisms responsible for changes in the statistical persistence caused by aging and neural disorders.

Although stride interval fluctuations change depending on gait speed in humans, the statistical persistence remains unchanged [55]. Our model with phase resetting also exhibited statistical persistence regardless of the gait speed (Fig. 4.5). The constraint on gait rhythm seems more crucial for the statistical persistence than the constraint on gait speed, as observed for walking to a metronome [55].

The standard deviation of stride interval fluctuations is about 0.04 s in human walking, which is 3% of the mean stride interval [54]. It was difficult for previous studies [31, 38] using biomechanical models to reproduce a magnitude of stride interval fluctuations similar to that for humans. Although [38] reproduced statistical persistence in stride intervals ($0.5 < \alpha \leq 1.0$) using a simple biomechanical model as in this study, their model was not robust and the noise amplitude was limited. Therefore, their stride interval fluctuations were much smaller than those in humans. Furthermore, the scaling exponent α was sensitive to the noise amplitude, and the fluctuations exhibited brown noise at high noise levels ($\alpha > 1.0$). In contrast, phase resetting made our model robust, which allowed a magnitude of stride interval fluctuations similar to that for healthy adults (Fig. 4.3). Furthermore, α was 0.5 to 1.0, which is consistent with observations of healthy adults, and was not sensitive to the noise amplitude (Fig. 4.4), but sensitive to the controller (i.e., whether phase resetting was used).

Previous studies [3, 32, 122, 133] have shown that phase resetting contributes to adaptive walking. In this study, we found that it also contributes to the statistical persistence of gait. In addition to the fact that statistical persistence is impaired by aging [53], central nervous system diseases, such as Parkinson's disease [30] and Huntington's disease [53], and experimental intervention for walking [55], it has been suggested that statistical persistence is linked to important characteristics of gait. [11] suggested that fluctuation persistence leads to redundancies in gait and helps predict and prevent fall risk. [1] and [31] showed that fluctuation persistence appears in gait with low gait stability. [38] showed that a decrease in the ability to perform finely controlled movements leads to an increase in motor output noise and impairs the persistence of fluctuations.

Many studies have reported long-range correlations in stride intervals in human walking based on the results of DFA [10,53–55], which indicates that stride-to-stride correlations decay in a scale-free (fractal-like) power-law fashion and suggests that each stride depends explicitly on many previous strides. However, DFA is highly sensitive to yielding false positive results [59,80], and it is difficult to conclude the presence of long-range correlations from DFA alone. Instead, DFA provides a valid indicator of statistical persistence and anti-persistence in a time series [80]. In this study, we used statistical persistence instead of long-range correlations to interpret the results of DFA, as discussed in [22].

4.4.3 Limitations of our model and future work

Based on the hypothesis that the statistical persistence in stride intervals emerge through dynamic interactions between the neural and biomechanical systems, we integrated a simple neural model and a simple biomechanical model to reproduce statistical persistence in stride intervals and change in this statistical property. However, our model is very simple and has limitations with regard to replicating many aspects of human walking. In particular, because the feedforward torques (4.9) and (4.10) were simply composed of a sinusoidal wave, the gait speeds of our model were slower than those of healthy adults (Fig. 4.2). In addition, although statistical persistence could be associated with low gait stability (low convergence speed to the limit cycle) [1,31], our model had higher stability than that of complicated models due to its simplicity. The high stability of our model with phase resetting might have caused the scaling exponent α to be ~ 0.6, which is smaller than that (~ 1) in healthy adults [54]. Furthermore, stochastic noise is ubiquitous in the central nervous system and peripheral sensory-motor systems [14,67,124]. However, our model used only torque noise, which may result in the difference between the statistical anti-persistence in the model without phase resetting and the white noise in walking to a metronome in humans [11,55].

Based on the findings in this study, it is important to verify the essential mechanisms responsible for changes in the statistical persistence by using biologically detailed neuromusculoskeletal models. In a previous study [122], we integrated a musculoskeletal model composed of seven rigid links and 18 muscles with a CPG model with a muscle synergy-based controller to investigate the contribution of phase resetting to the phase response characteristics during walking. In another previous study [33], we used a half-center type CPG model composed of a rhythm generator network, which was modeled using neuron populations of flexor and extensor centers based on [19,20] and [108], to clarify the mechanisms responsible for the CPG responses to afferent stimulation using dynamic systems theory based on nullclines. We plan to incorporate these biologically detailed models to further investigate the mechanisms responsible for changes in the statistical persistence.

4.5 Conclusion

In this study, we clarified the contribution of phase resetting to the generation and change of statistical persistence using a simple neuromechanical model. Specifically, our model reproduced the statistical persistence in stride intervals. A lack of phase resetting induced a loss of statistical persistence. Furthermore, we clarified the mechanisms responsible for changes in statistical persistence caused by phase resetting based on the phase response characteristics. Our findings provide important insight into the mechanisms underlying the generation and change of the statistical persistence in the stride intervals in human walking.

Chapter 5

Conclusion

5.1 Summary

In this study, we focused on the importance of the generation and change of spatial and temporal fractals generated by bipedal walking, and reproduced these fractals using simple models to clarify these mechanisms. For spatial fractal, we investigated the fractality of the basin of attraction using the simplest walking model. For temporal fractal, we created a model that combines a simple neural system and a body mechanical system, and reproduced fractal fluctuations in humans. In particular, we discussed its mechanism by focusing on the fact that the sensory feedback changes fractality.

In Chapter 2, we calculated the basin of attraction of passive dynamic walking using the simplest walking model. We investigated the range of slope angle in which the basin of attraction becomes fractal and confirmed that the basin of attraction becomes fractal when a certain slope angle is exceeded. Furthermore, the mechanism of formation of the fractal basin of attraction was clarified by focusing on the formation process of the basin of attraction based on the stretching and bending properties of the inverse image of the Poincaré map, which has been clarified in previous research [94]. In particular, we newly focused on the range of the Poincaré map, which corresponds to the collection of states after the model walked one step starting from the domain, and specified the regions that are stretched and bent by the sequential inverse image of the Poincaré map. The results showed that when the slit formed in the process of forming the basin of attraction penetrated the range, the number of slits increased at an accelerated rate owing to the stretching and bending effects of the Poincaré map, and the basin of attraction became fractal. On the other hand, when the slit did not penetrate the range, the formation of the slit stopped, and the basin of attraction did not become fractal.

In Chapter 3, we used the model used in Chapter 2 to investigate the changes in the basin of attraction depending on the slope angle. The results showed that the size and fractality changed sharply at specific slope angles. The mechanism by which these sharp changes occurred was elucidated by improving the analytical method in Chapter 2. Specifically, when a new slit penetrates the range by increasing the slope angle, the rate of increase in the number of slits in the formation process of

the basin of attraction changes. As a result, it was shown that the fractality and size of the basin of attraction changed drastically after the penetration. We also clarified that the formation process for the basin of attraction can be assumed to be a one-dimensional Cantor set when a specific slit penetrates at a certain slope angle and the basin of attraction disappears.

In Chapter 4, we assumed that fractality appears through the interaction between the neural system and the body mechanical system and reproduced the fractality of fluctuation in walking by using a simple CPG model combined with a simple biomechanical model. We confirmed that the model with sensory feedback showed statistical persistence, whereas the model without sensory feedback showed anti-persistence, and showed that this difference in persistence would correspond to the different characteristics between healthy subjects and aging or neural disease patients. Furthermore, we suggested that this difference would be due to different phase response characteristics. Specifically, based on the previous study [122] showing that sensory feedback affects the phase response characteristics in gait, we clarified that the phase response characteristics determine the fluctuation trend in the gait cycle, and as a result, may influence fractality. This suggests that fractality in other bipedal models and in actual humans could be explained based on phase response characteristics.

5.2 Future work

As shown in Chapters 2 and 3, the spatial fractality of the basin of attraction in passive dynamic walking was analyzed based on the dynamical systems theory. Similarly, the fractality of the basin of attraction has been reported in the Hénon map [41], which is often studied in the field of nonlinear dynamics. The map generates many periodic saddle orbits, whose manifolds cross each other. These crossings explain the generation of and changes in fractality in the basin of attraction [42]. Because many periodic saddle orbits could appear in the simplest walking model [76,77], we would like to clarify if the crossing of these manifolds affects fractality in the basin of attraction in the future.

As shown in Chapter 4, temporal fractality in gait would be related to the phase response characteristics. However, it remains unclear how phase response characteristics affect fractality. We would like to investigate temporal fractals using a more detailed neuromusculoskeletal model [122], which investigated phase response characteristics during walking. Furthermore, we would also like to clarify how phase response characteristics affect temporal fractals based on stochastic process theory in the future.

Future work should also be conducted on how spatial and temporal fractals interact with each other in walking. Because temporal fractality is explained based

on stochastic process theory, it is difficult to discuss the relation with spatial fractality, which is generally discussed in deterministic dynamical systems. However, as shown in Chapter 4, it has been shown that temporal fractality is related to the phase response characteristics, and by extending this argument, temporal fractals could arise from deterministic arguments. We would like to extend this discussion in the future to clarify how spatial and temporal fractals are related to each other in walking.

Appendix A

Deformation of $T^{-1}(D_1 \cap R)$ by U^{-1}

Here, we approximately solve the deformation of $T^{-1}(D_1 \cap R)$ by U^{-1} based on the analysis in our previous study [94]. We first denote the solution of equations of motion (2.1) and (2.2) by $\Theta(t) = [\theta(t)\,\dot{\theta}(t)\,\varphi(t)\,\dot{\varphi}(t)]$. From the definition of U, for a point $\Theta(0) \in T^{-1}(D_1 \cap R) \subset H$, there exists $\Delta > 0$ such that

$$\Theta(-\Delta) = U^{-1}(\Theta(0)) \in T(H) \tag{A.1}$$

where $-\Delta$ is used as the negative time to analyze U^{-1} (Fig. 2.2A). $\Theta(0)$, $\Theta(-\Delta)$, and $-\Delta$ correspond to the state just before foot contact, the state just after foot contact, and the duration of a step, respectively. $\Theta(-\Delta)$ gives the deformation of $T^{-1}(D_1 \cap R)$ by U^{-1}.

Since $\Theta(-\Delta)$ is in $T(H)$, the following equations are satisfied from (2.7), (2.8), and (2.9):

$$2\theta(-\Delta) = \varphi(-\Delta) \tag{A.2}$$

$$\dot{\varphi}(-\Delta) = \dot{\theta}(-\Delta)(1 - \cos 2\theta(-\Delta)) \tag{A.3}$$

$$\theta(-\Delta) > 0 \tag{A.4}$$

In addition, since $\Theta(-\Delta)$ is in H, the following equation is satisfied from (2.3):

$$2\theta(0) = \varphi(0) \tag{A.5}$$

In order to approximately solve (A.1), we linearize the equations of motion (2.1) and (2.2) around $[\gamma\,0\,0\,0]$ by

$$\ddot{\theta} = \theta - \gamma \tag{A.6}$$

$$\ddot{\varphi} = -(\varphi - \theta + \gamma) \tag{A.7}$$

The solution is obtained by

$$\theta = \gamma + C_1 \exp(t) + C_2 \exp(-t) \tag{A.8}$$

$$\varphi - \frac{\theta - \gamma}{2} = K \cos(t + \phi) \tag{A.9}$$

where C_1, C_2, K, and ϕ are the integration constants $(0 \leq \phi < 2\pi)$. Here, $\dot{\varphi}$ on plane Z is obtained by

$$\dot{\varphi}(0) = \frac{C_1 - C_2}{2} - K \sin \phi \tag{A.10}$$

C_1 and C_2 are determined by the initial conditions of θ and $\dot{\theta}$, as follows:

$$\begin{aligned} C_1 &= \frac{\theta(0) - \gamma + \dot{\theta}(0)}{2} \\ C_2 &= \frac{\theta(0) - \gamma - \dot{\theta}(0)}{2} \end{aligned} \tag{A.11}$$

In contrast, K and ϕ are determined by the initial conditions of θ, φ, $\dot{\theta}$, and $\dot{\varphi}$.

From (A.2), (A.3), (A.5), (A.8), and (A.9), we have the following equations:

$$\theta(-\Delta) = C_1 \exp(-\Delta) + C_2 \exp \Delta + \gamma \tag{A.12}$$

$$\dot{\theta}(-\Delta) = C_1 \exp(-\Delta) - C_2 \exp \Delta \tag{A.13}$$

$$K \cos(-\Delta + \phi) = \frac{3\theta(-\Delta)}{2} + \frac{\gamma}{2} \tag{A.14}$$

$$K \sin(-\Delta + \phi) = -\dot{\theta}(-\Delta) \left\{ \frac{1}{2} - \cos 2\theta(-\Delta) \right\} \tag{A.15}$$

$$K \cos \phi = \frac{3}{2} \left(C_1 + C_2 + \frac{4\gamma}{3} \right) \tag{A.16}$$

where Δ, ϕ, K, $\theta(-\Delta)$, and $\dot{\theta}(-\Delta)$ are unknown variables (C_1 and C_2 are determined in (A.11) from $[\theta(0)\,\dot{\theta}(0)]$). We obtain $\Theta(-\Delta)$ from $[\theta(0)\,\dot{\theta}(0)]$ by solving (A.12)–(A.16).

In order to show how U^{-1} deforms $T^{-1}(D_1 \cap R)$, we used the approximated solution given above. In particular, we used the line segment $\hat{P}_1\hat{Q}_1$ within $T^{-1}(D_1 \cap R)$, as shown Fig. 2.5A ($\hat{P}_1$: $[\theta\,\dot{\theta}] = [-0.2311 \;\; -0.2536]$, $\hat{Q}_1$: $[\theta, \dot{\theta}] = [-0.3085 \;\; -0.3915]$). This segment was moved to two curves f_2e_2 and f_2g_2 by U^{-1}, which approximate $U^{-1}(T^{-1}(D_1 \cap R))$, as shown in Fig. 2.5E.

Bibliography

[1] J. Ahn and N. Hogan. Long-range correlations in stride intervals may emerge from non-chaotic walking dynamics. *PLoS One*, 8(9):e73239, 2013.

[2] N. Akashi, K. Nakajima, and Y. Kuniyoshi. Unpredictable as dice: analyzing riddled basin structures in a passive dynamic walker. In *Proc. IEEE Int. Symp. Micro-NanoMechatronics Hum. Sci.*, pages 1–6, 2019.

[3] S. Aoi, N. Ogihara, T. Funato, Y. Sugimoto, and K. Tsuchiya. Evaluating functional roles of phase resetting in generation of adaptive human bipedal walking with a physiologically based model of the spinal pattern generator. *Biol. Cybern.*, 102(5):373–387, 2010.

[4] S. Aoi, T. Ohashi, R. Bamba, S. Fujiki, D. Tamura, T. Funato, K. Senda, Y. Ivanenko, and K. Tsuchiya. Neuromusculoskeletal model that walks and runs across a speed range with a few motor control parameter changes based on the muscle synergy hypothesis. *Sci. Rep.*, 9(1):1–5, 2019.

[5] S. Aoi, T. Tanaka, S. Fujiki, T. Funato, K. Senda, and K. Tsuchiya. Advantage of straight walk instability in turning maneuver of multilegged locomotion: a robotics approach. *Sci. Rep.*, 6(1):30199, 2016.

[6] S. Aoi and K. Tsuchiya. Stability analysis of a simple walking model driven by a rhythmic signal. In *IEEE/RSJ Int. Conf. Intell. Robot. Syst.*, number 2, pages 1365–1370. IEEE, 2004.

[7] S. Aoi and K. Tsuchiya. Stability analysis of a simple walking model driven by an oscillator with a phase reset using sensory feedback. *IEEE Trans. Robot.*, 22(2):391–397, 2006.

[8] S. Aoi and K. Tsuchiya. Self-stability of a simple walking model driven by a rhythmic signal. *Nonlinear Dyn.*, 48:1–16, 2007.

[9] F. Asano, Z. W. Luo, and M. Yamakita. Biped gait generation and control based on a unified property of passive dynamic walking. *IEEE Trans. Robot.*, 21(4):754–762, 2005.

[10] Y. Ashkenazy, J. M. Hausdorff, P. C. Ivanov, and H. E. Stanley. A stochastic model of human gait dynamics. *Phys. A*, 316(1-4):662–670, 2002.

[11] N. K. Bohnsack-McLagan, J. P. Cusumano, and J. B. Dingwell. Adaptability of stride-to-stride control of stepping movements in human walking. *J. Biomech.*, 49(2):229–237, 2016.

[12] S. M. Bruijn, D. J. Bregman, O. G. Meijer, P. J. Beek, and J. H. van Dieën. The validity of stability measures: A modelling approach. *J. Biomech.*, 44(13):2401–2408, 2011.

[13] R. E. Burke, A. M. Degtyarenko, and E. S. Simon. Patterns of locomotor drive to motoneurons and last-order interneurons: Clues to the structure of the CPG. *J. Neurophysiol.*, 86(1):447–462, 2001.

[14] M. M. Churchland, A. Afshar, and K. V. Shenoy. A central source of movement variability. *Neuron*, 52(6):1085–1096, 2006.

[15] T. Chyou, G. Liddell, and M. Paulin. An upper-body can improve the stability and efficiency of passive dynamic walking. *J. Theor. Biol.*, 285(1):126–135, 2011.

[16] M. J. Coleman and A. Ruina. An uncontrolled walking toy that cannot stand still. *Phys. Rev. Lett.*, 80(16):3658–3661, 1998.

[17] S. Collins, A. Ruina, R. Tedrake, and M. Wisse. Efficient bipedal robots based on passive-dynamic walkers. *Science*, 307(5712):1082–1085, 2005.

[18] S. H. Collins, M. Wisse, and A. Ruina. A three-dimensional passive-dynamic walking robot with two legs and knees. *Int. J. Robot. Res.*, 20(7):607–615, 2001.

[19] S. M. Danner, N. A. Shevtsova, A. Frigon, and I. A. Rybak. Computational modeling of spinal circuits controlling limb coordination and gaits in quadrupeds. *Elife*, 6:1–25, 2017.

[20] S. M. Danner, S. D. Wilshin, N. A. Shevtsova, and I. A. Rybak. Central control of interlimb coordination and speed-dependent gait expression in quadrupeds. *J. Physiol.*, 594(23):6947–6967, 2016.

[21] K. Deng, M. Zhao, and W. Xu. Level-ground walking for a bipedal robot with a torso via hip series elastic actuators and its gait bifurcation control. *Robot. Auton. Syst.*, 79:58–71, 2016.

[22] J. B. Dingwell and J. P. Cusumano. Re-interpreting detrended fluctuation analyses of stride-to-stride variability in human walking. *Gait Posture*, 32(3):348–353, 2010.

[23] J. M. Donelan, R. Kram, and A. D. Kuo. Mechanical work for step-to-step transitions is a major determinant of the metabolic cost of human walking. *J. Exp. Biol.*, 205(23):3717–3727, 2002.

[24] M. S. Dutra, A. C. De Pina Filho, and V. F. Romano. Modeling of a bipedal locomotor using coupled nonlinear oscillators of van der pol. *Biol. Cybern.*, 88(4):286–292, 2003.

[25] J. Duysens. Fluctuations in sensitivity to rhythm resetting effects during the cat's step cycle. *Brain Res.*, 133(1):190–195, 1977.

[26] F. Dzeladini, J. van den Kieboom, and A. Ijspeert. The contribution of a central pattern generator in a reflex-based neuromuscular model. *Front. Hum. Neurosci.*, 8:1–18, 2014.

[27] A. Eke, P. Hermán, J. Bassingthwaighte, G. Raymond, D. Percival, M. Cannon, I. Balla, and C. Ikrényi. Physiological time series: distinguishing fractal noises from motions. *Pflügers Arch. Eur. J. Physiol.*, 439(4):403–415, 2000.

[28] K. Falconer. *Fractal Geometry: Mathematical Foundations and Applications Fractal*. Wiley, 2003.

[29] P. F. Fougere. On the accuracy of spectrum analysis of red noise processes using maximum entropy and periodogram methods: Simulation studies and application to geophysical data. *J. Geophys. Res.*, 90(A5):4355, 1985.

[30] S. Frenkel-Toledo, N. Giladi, C. Peretz, T. Herman, L. Gruendlinger, and J. M. Hausdorff. Treadmill walking as an external pacemaker to improve gait rhythm and stability in parkinson's disease. *Mov. Disord.*, 20(9):1109–1114, 2005.

[31] C. Fu, Y. Suzuki, P. Morasso, and T. Nomura. Phase resetting and intermittent control at the edge of stability in a simple biped model generates 1/f-like gait cycle variability. *Biol. Cybern.*, 114(1):95–111, 2020.

[32] S. Fujiki, S. Aoi, T. Funato, Y. Sato, K. Tsuchiya, and D. Yanagihara. Adaptive hindlimb split-belt treadmill walking in rats by controlling basic muscle activation patterns via phase resetting. *Sci. Rep.*, 8(1):1–5, 2018.

[33] S. Fujiki, S. Aoi, K. Tsuchiya, S. M. Danner, I. A. Rybak, and D. Yanagihara. Phase-dependent response to afferent stimulation during fictive locomotion: A computational modeling study. *Front. Neurosci.*, 13, 2019.

[34] T. Funato, Y. Yamamoto, S. Aoi, T. Imai, T. Aoyagi, N. Tomita, and K. Tsuchiya. Evaluation of the phase-dependent rhythm control of human walking using phase response curves. *PLoS Comput. Biol.*, 12(5):1–23, 2016.

[35] M. Garcia, A. Chatterjee, and A. Ruina. Efficiency, speed, and scaling of two-dimensional passive-dynamic walking. *Dyn. Stab. Syst.*, 15(2):75–99, 2000.

[36] M. Garcia, A. Chatterjee, A. Ruina, and M. J. Coleman. The simplest walking model: stability, complexity, and scaling. *J. Biomech. Eng.*, 120(2):281–288, 1998.

[37] D. H. Gates and J. B. Dingwell. Peripheral neuropathy does not alter the fractal dynamics of stride intervals of gait. *J. Appl. Physiol.*, 102(3):965–971, 2007.

[38] D. H. Gates, J. L. Su, and J. B. Dingwell. Possible biomechanical origins of the long-range correlations in stride intervals of walking. *Phys. A*, 380:259–270, 2007.

[39] A. L. Goldberger, L. A. N. Amaral, J. M. Hausdorff, P. C. Ivanov, C.-K. Peng, and H. E. Stanley. Fractal dynamics in physiology: Alterations with disease and aging. *Proc. Natl. Acad. Sci. U. S. A.*, 99:2466–2472, 2002.

[40] A. Goswami, B. Thuilot, and B. Espiau. A study of the passive gait of a compass-like biped robot: symmetry and chaos. *Int. J. Robot. Res.*, 17(12):1282–1301, 1998.

[41] C. Grebogi, S. W. McDonald, E. Ott, and J. A. Yorke. Final state sensitivity: an obstruction to predictability. *Phys. Lett. A*, 99(9):415–418, 1983.

[42] C. Grebogi, E. Ott, and J. A. Yorke. Basin boundary metamorphoses: changes in accessible boundary orbits. *Nucl. Phys. B Proc. Suppl.*, 2(C):281–300, 1987.

[43] S. Grillner. Locomotion in vertebrates: central mechanisms and reflex interaction. *Physiol. Rev.*, 55(2):247–304, 1975.

[44] S. Grillner. Control of Locomotion in Bipeds, Tetrapods, and Fish. In *Compr. Physiol.*, pages 1179–1236. Wiley, 1981.

[45] H. Gritli and S. Belghith. Walking dynamics of the passive compass-gait model under OGY-based control: emergence of bifurcations and chaos. *Commun. Nonlinear Sci. Numer. Simul.*, 47:308–327, 2017.

[46] H. Gritli and S. Belghith. Walking dynamics of the passive compass-gait model under OGY-based state-feedback control: analysis of local bifurcations via the hybrid Poincaré map. *Chaos Solitons Fractals*, 98:72–87, 2017.

[47] H. Gritli, S. Belghith, and N. Khraief. Cyclic-fold bifurcation and boundary crisis in dynamic walking of biped robots. *Int. J. Bifurc. Chaos*, 22(10):1250257, 2012.

[48] H. Gritli, S. Belghith, and N. Khraief. Intermittency and interior crisis as route to chaos in dynamic walking of two biped robots. *Int. J. Bifurc. Chaos*, 22(03):1250056, 2012.

[49] H. Gritli, N. Khraief, and S. Belghith. Period-three route to chaos induced by a cyclic-fold bifurcation in passive dynamic walking of a compass-gait biped robot. *Commun. Nonlinear Sci. Numer. Simul.*, 17(11):4356–4372, 2012.

[50] P. Guertin, M. J. Angel, M. C. Perreault, and D. A. McCrea. Ankle extensor group i afferents excite extensors throughout the hindlimb during fictive locomotion in the cat. *J. Physiol.*, 487(1):197–209, 1995.

[51] R. Hardstone, S.-S. Poil, G. Schiavone, R. Jansen, V. V. Nikulin, H. D. Mansvelder, and K. Linkenkaer-Hansen. Detrended fluctuation analysis: A scale-free view on neuronal oscillations. *Front. Physiol.*, 3:1–13, 2012.

[52] K. Hase, K. Miyashita, S. Ok, and Y. Arakawa. Human gait simulation with a neuromusculoskeletal model and evolutionary computation. *J. Vis. Comput. Animat.*, 14(2):73–92, 2003.

[53] J. M. Hausdorff, S. L. Mitchell, R. Firtion, C. K. Peng, M. E. Cudkowicz, J. Y. Wei, and A. L. Goldberger. Altered fractal dynamics of gait: reduced stride-interval correlations with aging and huntington's disease. *J. Appl. Physiol.*, 82(1):262–269, 1997.

[54] J. M. Hausdorff, C. K. Peng, Z. Ladin, J. Y. Wei, and A. L. Goldberger. Is walking a random walk? Evidence for long-range correlations in stride interval of human gait. *J. Appl. Physiol.*, 78(1):349–358, 1995.

[55] J. M. Hausdorff, P. L. Purdon, C. K. Peng, Z. Ladin, J. Y. Wei, and A. L. Goldberger. Fractal dynamics of human gait: stability of long-range correlations in stride interval fluctuations. *J. Appl. Physiol.*, 80(5):1448–1457, 1996.

[56] J. M. Hausdorff, L. Zemany, C.-K. Peng, and A. L. Goldberger. Maturation of gait dynamics: stride-to-stride variability and its temporal organization in children. *J. Appl. Physiol.*, 86(3):1040–1047, 1999.

[57] D. J. Higham. An algorithmic introduction to numerical simulation of stochastic differential equations. *SIAM Rev.*, 43(3):525–546, 2001.

[58] D. G. Hobbelen and M. Wisse. Swing-leg retraction for limit cycle walkers improves disturbance rejection. *IEEE Trans. Robot.*, 24(2):377–389, 2008.

[59] M. Höll and H. Kantz. The fluctuation function of the detrended fluctuation analysis — investigation on the AR(1) process. *Eur. Phys. J. B*, 88(5):126, 2015.

[60] K. Hosoda, T. Takuma, A. Nakamoto, and S. Hayashi. Biped robot design powered by antagonistic pneumatic actuators for multi-modal locomotion. *Robot. Auton. Syst.*, 56(1):46–53, 2008.

[61] H. Hultborn and J. B. Nielsen. Spinal control of locomotion - from cat to man. *Acta Physiol.*, 189(2):111–121, 2007.

[62] E. A. F. Ihlen. Introduction to multifractal detrended fluctuation analysis in matlab. *Front. Physiol.*, 3:1–18, 2012.

[63] Y. P. Ivanenko, R. E. Poppele, and F. Lacquaniti. Five basic muscle activation patterns account for muscle activity during human locomotion. *J. Physiol.*, 556(1):267–282, 2004.

[64] Y. P. Ivanenko, R. E. Poppele, and F. Lacquaniti. Motor control programs and walking. *Neurosci.*, 12(4):339–348, 2006.

[65] S. Jo. Hypothetical neural control of human bipedal walking with voluntary modulation. *Med. Biol. Eng. Comput.*, 46(2):179–193, 2008.

[66] S. Jo and S. G. Massaquoi. A model of cerebrocerebello-spinomuscular interaction in the sagittal control of human walking. *Biol. Cybern.*, 96(3):279–307, 2007.

[67] K. E. Jones, A. F. C. Hamilton, and D. M. Wolpert. Sources of signal-dependent noise during isometric force production. *J. Neurophysiol.*, 88(3):1533–1544, 2002.

[68] K. Jordan, J. H. Challis, and K. M. Newell. Long range correlations in the stride interval of running. *Gait Posture*, 24(1):120–125, 2006.

[69] Y. Kim, Y. Tagawa, G. Obinata, and K. Hase. Robust control of CPG-based 3D neuromusculoskeletal walking model. *Biol. Cybern.*, 105:269–282, 2011.

[70] T. Kinugasa, T. Ito, H. Kitamura, K. Ando, S. Fujimoto, K. Yoshida, and M. Iribe. 3D dynamic biped walker with flat feet and ankle springs: passive gait analysis and extension to active walking. *J. Robot. Mechatron.*, 27(4):444–452, 2015.

[71] A. D. Kuo. A simple model of bipedal walking predicts the preferred speed-step length relationship. *J. Biomech. Eng.*, 123(3):264–269, 2001.

[72] A. D. Kuo. Energetics of actively powered locomotion using the simplest walking model. *J. Biomech. Eng.*, 124(1):113–120, 2002.

[73] A. D. Kuo, J. M. Donelan, and A. Ruina. Energetic consequences of walking like an inverted pendulum: step-to-step transitions. *Exerc. Sport Sci. Rev.*, 33(2):88–97, 2005.

[74] Y. Kuramoto. *Chemical Oscillations, Waves, and Turbulence*. Springer, Berlin, 1984.

[75] M. Lafreniere-Roula and D. A. McCrea. Deletions of rhythmic motoneuron activity during fictive locomotion and scratch provide clues to the organization of the mammalian central pattern generator. *J. Neurophysiol.*, 94(2):1120–1132, 2005.

[76] Q. Li, S. Tang, and X. S. Yang. New bifurcations in the simplest passive walking model. *Chaos*, 23(4), 2013.

[77] Q. Li and X. S. Yang. New walking dynamics in the simplest passive bipedal walking model. *Appl. Math. Model.*, 36(11):5262–5271, 2012.

[78] B. Mandelbrot. How long is the coast of Britain? Statistical self-similarity and fractional dimension. *Science*, 156(3775):636–638, 1967.

[79] B. B. Mandelbrot. *The fractal geometry of nature*, volume 1. WH freeman New York, 1982.

[80] D. Maraun, H. W. Rust, and J. Timmer. Tempting long-memory - on the interpretation of dfa results. *Nonlinear Process. Geophys.*, 11(4):495–503, 2004.

[81] K. Matsuoka. Mechanisms of frequency and pattern control in the neural rhythm generators. *Biol. Cybern.*, 56(6):345–353, 1987.

[82] D. A. McCrea. Spinal circuitry of sensorimotor control of locomotion. *J. Physiol.*, 533(1):41–50, 2001.

[83] D. A. McCrea and I. A. Rybak. Modeling the mammalian locomotor CPG: insights from mistakes and perturbations. In *Prog. Brain Res.*, volume 165, pages 235–253. 2007.

[84] S. W. McDonald, C. Grebogi, E. Ott, and J. A. Yorke. Fractal basin boundaries. *Phys. D*, 17(2):125–153, 1985.

[85] T. McGeer. Passive dynamic walking. *Int. J. Robot. Res.*, 9(2):62–82, 1990.

[86] T. McGeer. Passive walking with knees. In *Proceedings., IEEE Int. Conf. Robot. Autom.*, pages 1640–1645. IEEE Comput. Soc. Press, 1990.

[87] T. McGeer. Principles of Walking and Running. pages 113–139. 1992.

[88] K. Minassian, I. Persy, F. Rattay, M. Pinter, H. Kern, and M. Dimitrijevic. Human lumbar cord circuitries can be activated by extrinsic tonic input to generate locomotor-like activity. *Hum. Mov. Sci.*, 26(2):275–295, 2007.

[89] S. Mochiyama and T. Hikihara. Impulsive torque control of biped gait with power packets. *Nonlinear Dyn.*, 102(2):951–963, 2020.

[90] S. Mochon and T. A. McMahon. Ballistic walking. *J. Biomech.*, 13(1):49–57, 1980.

[91] S. Montazeri Moghadam, M. Sadeghi Talarposhti, A. Niaty, F. Towhidkhah, and S. Jafari. The simple chaotic model of passive dynamic walking. *Nonlinear Dyn.*, 93(3):1183–1199, 2018.

[92] J. A. Nessler, T. Spargo, A. Craig-Jones, and J. G. Milton. Phase resetting behavior in human gait is influenced by treadmill walking speed. *Gait Posture*, 43:187–191, 2016.

[93] I. Obayashi, S. Aoi, K. Tsuchiya, and H. Kokubu. Common formation mechanism of basin of attraction for bipedal walking models by saddle hyperbolicity and hybrid dynamics. *Jpn. J. Ind. Appl. Math.*, 32(2):315–332, 2015.

[94] I. Obayashi, S. Aoi, K. Tsuchiya, and H. Kokubu. Formation mechanism of a basin of attraction for passive dynamic walking induced by intrinsic hyperbolicity. *Proc. R. Soc. A*, 472(2190):20160028, 2016.

[95] N. Ogihara and N. Yamazaki. Generation of human bipedal locomotion by a bio-mimetic neuro-musculo-skeletal model. *Biol. Cybern.*, 84(1):1–11, 2001.

[96] K. Okamoto, S. Aoi, I. Obayashi, H. Kokubu, K. Senda, and K. Tsuchiya. Investigating phase resetting effect on basin of attraction for walking using a simple model. In *Int. Symp. Adapt. Motion Anim. Mach.*, Lausanne, 2019.

[97] K. Okamoto, S. Aoi, I. Obayashi, H. Kokubu, K. Senda, and K. Tsuchiya. Fractal mechanism of basin of attraction in passive dynamic walking. *Bioinspir. Biomim.*, 15(5):055002, 2020.

[98] G. Orlovsky, T. G. Deliagina, and S. Grillner. *Neuronal Control of Locomotion-From Mollusc to Man*. Oxford University Press, 1999.

[99] D. Owaki, S. Y. Horikiri, J. Nishii, and A. Ishiguro. Tegotae-Based Control Produces Adaptive Inter- and Intra-limb Coordination in Bipedal Walking. *Front. Neurorobot.*, 15:1–16, 2021.

[100] K. G. Pearson. Generating the walking gait: role of sensory feedback. In *Prog. Brain Res.*, volume 143, pages 123–129. 2004.

[101] C.-K. Peng, S. V. Buldyrev, A. L. Goldberger, S. Havlin, M. Simons, and H. E. Stanley. Finite-size effects on long-range correlations: Implications for analyzing DNA sequences. *Phys. Rev. E*, 47(5):3730–3733, 1993.

[102] C.-K. Peng, S. V. Buldyrev, J. M. Hausdorff, S. Havlin, J. E. Mietus, M. Simons, H. E. Stanley, and A. L. Goldberger. Non-equilibrium dynamics as an indispensable characteristic of a healthy biological system. *Integr. Physiol. Behav. Sci.*, 29(3):283–293, 1994.

[103] C.-K. Peng, S. V. Buldyrev, S. Havlin, M. Simons, H. E. Stanley, and A. L. Goldberger. Mosaic organization of DNA nucleotides. *Phys. Rev. E*, 49(2):1685–1689, 1994.

[104] C.-K. Peng, J. M. Hausdorff, and A. L. Goldberger. *Fractal mechanisms in neuronal control: human heartbeat and gait dynamics in health and disease*, page 66–96. Cambridge University Press, 2000.

[105] M. C. Perreault, M. J. Angel, P. Guertin, and D. A. McCrea. Effects of stimulation of hindlimb flexor group II afferents during fictive locomotion in the cat. *J. Physiol.*, 487(1):211–220, 1995.

[106] S. Rossignol. Neural Control of Stereotypic Limb Movements. In *Compr. Physiol.*, pages 173–216. Wiley, 1996.

[107] S. Rossignol, R. Dubuc, and J. P. Gossard. Dynamic sensorimotor interactions in locomotion. *Physiol. Rev.*, 86(1):89–154, 2006.

[108] I. A. Rybak, N. A. Shevtsova, M. Lafreniere-Roula, and D. A. McCrea. Modelling spinal circuitry involved in locomotor pattern generation: insights from deletions during fictive locomotion. *J. Physiol.*, 577(2):617–639, 2006.

[109] I. A. Rybak, K. Stecina, N. A. Shevtsova, and D. A. McCrea. Modelling spinal circuitry involved in locomotor pattern generation: Insights from the effects of afferent stimulation. *J. Physiol.*, 577(2):641–658, 2006.

[110] M. Safartoobi, M. Dardel, and H. M. Daniali. Passive walking biped robot model with flexible viscoelastic legs. *Nonlinear Dyn.*, 109:2615–2636, 2022.

[111] E. D. Schomburg, N. Petersen, I. Barajon, and H. Hultborn. Flexor reflex afferents reset the step cycle during fictive locomotion in the cat. *Exp. Brain Res.*, 122(3):339–350, 1998.

[112] A. L. Schwab and M. Wisse. Basin of attraction of the simplest walking model. In *Proc. ASME Int. Des. Eng. Tech. Conf.*, pages 531–539, 2001.

[113] M. L. Shik and G. N. Orlovsky. Neurophysiology of locomotor automatism. *Physiol. Rev.*, 56(3):465–501, 1976.

[114] E. Sidorov and M. Zacksenhouse. Lyapunov based estimation of the basin of attraction of poincare maps with applications to limit cycle walking. *Nonlinear Anal. Hybrid Syst.*, 33:179–194, 2019.

[115] S. Smale. Differentiable dynamical systems. *Bull. Am. Math. Soc.*, 73(6):747–818, 1967.

[116] K. Stecina, J. Quevedo, and D. A. McCrea. Parallel reflex pathways from flexor muscle afferents evoking resetting and flexion enhancement during fictive locomotion and scratch in the cat. *J. Physiol.*, 569(1):275–290, 2005.

[117] S. H. Strogatz. *Nonlinear Dynamics and Chaos: With Applications to Physics, Biology, Chemistry, and Engineering*. CRC Press, New York, 1994.

[118] Y. Sugimoto and K. Osuka. Stability analysis of passive dynamic walking-an approach via interpretation of poincare map's structure. *Trans. Inst. Syst. Control Inf. Eng.*, 18(7):255–260, 2005.

[119] Y. Sugimoto and K. Osuka. Hierarchical implicit feedback structure in passive dynamic walking. *J. Robot. Mechatron.*, 20(4):559–566, 2008.

[120] G. Taga. A model of the neuro-musculo-skeletal system for human locomotion. *Biol. Cybern.*, 73(2):113–121, 1995.

[121] G. Taga, Y. Yamaguchi, and H. Shimizu. Self-organized control of bipedal locomotion by neural oscillators in unpredictable environment. *Biol. Cybern.*, 65(3):147–159, 1991.

[122] D. Tamura, S. Aoi, T. Funato, S. Fujiki, K. Senda, and K. Tsuchiya. Contribution of phase resetting to adaptive rhythm control in human walking based on the phase response curves of a neuromusculoskeletal model. *Front. Neurosci.*, 14:17, 2020.

[123] D. L. Turcotte. *Fractals and Chaos in Geology and Geophysics*. Cambridge University Press, 1997.

[124] R. J. Van Beers, P. Haggard, and D. M. Wolpert. The role of execution noise in movement variability. *J. Neurophysiol.*, 91(2):1050–1063, 2004.

[125] B. J. West and L. Griffin. Allometric control of human gait. *Fractals*, 6(2):101–108, 1998.

[126] B. J. West and L. Griffin. Allometric control, inverse power laws and human gait. *Chaos Soliton. Fract.*, 10(9):1519–1527, 1999.

[127] B. J. West and N. Scafetta. Nonlinear dynamical model of human gait. *Phys. Rev. E*, 67(5):051917, 2003.

[128] A. T. Winfree. *The Geometry of Biological Time*. Springer, New York, 1980.

[129] D. A. Winter. *Biomechanics and Motor Control of Human Movement*. John Wiley, New York, 2004.

[130] M. Wisse, D. G. E. Hobbelen, and A. L. Schwab. Adding an upper body to passive dynamic walking robots by means of a bisecting hip mechanism. *IEEE Trans. Robot.*, 23(1):112–123, 2007.

[131] M. Wisse, A. Schwab, R. van der Linde, and F. van der Helm. How to keep from falling forward: elementary swing leg action for passive dynamic walkers. *IEEE Trans. Robot.*, 21(3):393–401, 2005.

[132] Y. Yamamoto and R. L. Hughson. On the fractal nature of heart rate variability in humans: effects of data length and beta-adrenergic blockade. *American Journal of Physiology-Regulatory, Integrative and Comparative Physiology*, 266(1):R40–R49, 1994.

[133] T. Yamasaki, T. Nomura, and S. Sato. Possible functional roles of phase resetting during walking. *Biol. Cybern.*, 88(6):468–496, 2003.

[134] W. Znegui, H. Gritli, and S. Belghith. Design of an explicit expression of the poincaré map for the passive dynamic walking of the compass-gait biped model. *Chaos Soliton. Fractals*, 130:109436, 2020.

[135] W. Znegui, H. Gritli, and S. Belghith. Stabilization of the passive walking dynamics of the compass-gait biped robot by developing the analytical expression of the controlled poincaré map. *Nonlinear Dyn.*, 101(2):1061–1091, 2020.

[136] W. Znegui, H. Gritli, and S. Belghith. A new poincaré map for investigating the complex walking behavior of the compass-gait biped robot. *Appl. Math. Model.*, 94:534–557, 2021.

Publication List

Journal Articles

[1] K. Okamoto, S. Aoi, I. Obayashi, H. Kokubu, K. Senda, and K. Tsuchiya. Fractal mechanism of basin of attraction in passive dynamic walking. *Bioinspir. Biomim.*, 15(5):055002, 2020.

[2] K. Okamoto, I. Obayashi, H. Kokubu, K. Senda, K. Tsuchiya, and S. Aoi. Contribution of phase resetting to statistical persistence in stride intervals: A modeling study. *Front. Neural Circuits*, 16:836121, 2022.

[3] K. Okamoto, N. Akashi, I. Obayashi, K. Nakajima, H. Kokubu, K. Senda, K. Tsuchiya, and S. Aoi. Sharp changes in fractal basin of attraction in passive dynamic walking. *Nonlinear Dyn*, 111:21941–21955, 2023.

Conference Proceedings

[1] K. Okamoto, S. Aoi, I. Obayashi, H. Kokubu, K. Senda, and K. Tsuchiya. Investigating phase resetting effect on basin of attraction for walking using a simple model. In *Int. Symp. Adapt. Motion Anim. Mach.*, Lausanne, 2019.

[2] K. Okamoto, S. Aoi, I. Obayashi, H. Kokubu, K. Senda, and K. Tsuchiya. Disappearance of chaotic attractor of passive dynamic walking by stretch-bending deformation in basin of attraction. In *IEEE/RSJ Int. Conf. Intell. Robot. Syst.*, pages 3908–3913, Las Vegas, 2020.

[3] K. Okamoto, S. Aoi, I. Obayashi, H. Kokubu, K. Senda, and K. Tsuchiya. Boundary crisis by heteroclinic tangency in passive dynamic walking. In *Int. Symp. Swarm Behav. Bio-Inspired Robot.*, pages 90–93, Kyoto, Japan, 2021.

[4] K. Okamoto, S. Aoi, I. Obayashi, H. Kokubu, K. Senda, and K. Tsuchiya. Investigating contribution of phase resetting to long-range correlations in stride intervals using a simple model. In *Asian Control Conf.*, pages 1215–1216, Jeju Island, Korea, 2022.

[5] K. Okamoto, N. Akashi, I. Obayashi, H. Kokubu, K. Nakajima, K. Senda, K. Tsuchiya, and S. Aoi. Sudden change in fractality of basin boundary in passive dynamic walking. In *Int. Symp. Adapt. Motion Anim. Mach.*, Kobe, Japan, 2023.